SOLAR WIND AND NEUTRAL ATOMS IN THE HELIOSPHERE

Analysis of Current Data and Preparation for Future Missions

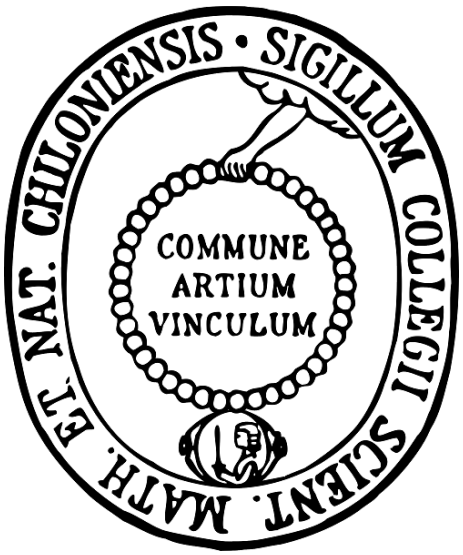

Dissertation
zur Erlangung des Doktorgrades
der Mathematisch-Naturwissenschaftlichen Fakultät
der Christian-Albrechts-Universität zu Kiel
vorgelegt von

THIES PELEIKIS

–Kiel, Mai 2017 –

Erster Gutachter (Supervisor):
Prof. Dr. Robert F. Wimmer-Schweingruber

Zweiter Gutachter (Advisor):
Prof. Dr. Wolfgang J. Duschl

Tag der mündlichen Prüfung:
22.6.2017

Zum Druck genehmigt:
22.6.2017

ABSTRACT

The Sun shapes our immediate surroundings in space and creates the heliosphere, which is filled with several particle populations. The most abundant one is the solar wind, which is a continuous stream of charged particles emitted by the Sun. Additionally, there are other particle species to be found in interplanetary space, like cosmic rays, energetic neutral atoms and so called pick up ions. Naturally, the heliosphere and the particles within have been subject of intensive research in the past decades. Nevertheless, many questions which arose during that time are still unanswered.
Here we will focus on two aspects of the heliosphere, namely the slow solar wind and energetic neutral atoms. While the slow solar wind is well characterized in its parameters, the mechanisms of its origin at the Sun are not well understood. Regarding the energetic neutral atoms neither their characteristics nor their origin is well understood, since there are few direct observations of these particles. In this work on the hand we look at observational data of the slow solar wind and combine this with a model of the coronal magnetic field in order to better understand its origin. On the other hand we prepare future missions for the measurement of the source regions of the slow solar wind and the observation of heliospheric neutral particles.
The observational data covered here was taken by the Ulysses and ACE spacecraft and it is combined with a Potential Field Source Surface (PFSS) model that gives us the magnetic field line configuration in the corona. From this we draw conclusions about the mechanism that might release the plasma which makes up the slow solar wind.
To support the upcoming Solar Orbiter mission we devised a measurement scheme for the Spectral Imaging of the Coronal Environment (SPICE) instrument which will enable the remote observation of solar wind plasma at its source location and the in-situ measurement of the very same plasma package with in-situ particle detectors. This kind of observation will hopefully greatly improve our understanding of the formation of slow solar wind.
And finally we help prepare the foundation of future missions that measure the neutral component in the heliosphere by establishing a calibration facility for heliospheric particle detectors. Part of this facility are Faraday cups which measure the particle beams. These Faraday cups have been calibrated for the detection of neutral particles and serve now as reference detectors for future neutral particle detectors.

ZUSAMMENFASSUNG

Unsere unmittelbare Umgebung im Weltraum, die Heliosphäre, wird von der Sonne geschaffen und ist angefüllt mit verschiedenen Teilchenpopulationen. Die größte davon, der Sonnenwind, ist ein kontinuierlicher Strom geladener Teilchen ausgehend von der Sonne. Zusätzlich existieren noch andere Teilchenarten im interplanetaren Raum, wie zum Beispiel die kosmische Strahlung, energiereiche neutrale

Atome und die so genannten Pick Up Ionen. Im Verlauf der letzten Jahrzehnte war die Heliosphäre und die darin enthaltenen Teilchenpopulationen Gegenstand intensiver Forschung. Dennoch sind viele Fragen diesbezüglich immer noch ungeklärt.
Wir werden uns hier auf zwei Aspekte der Heliosphäre fokussieren, nämlich auf den langsamen Sonnenwind und auf energiereiche neutrale Atome. Während der langsame Sonnenwind in seinen Eigenschaften gut charakterisiert ist, ist sein Ursprung auf der Sonne nicht gut verstanden. Im Falle der energiereichen neutralen Atome sind weder ihr genauen Eigenschaften noch ihr Ursprung gut verstanden, insbesondere da es nur wenige direkte Messungen dieser Teilchen gibt. In dieser Arbeit werden wir uns zum einen Beobachtungsdaten des langsamen Sonnenwindes anschauen und diese mit einem Modell des koronalen Magnetfelds kombinieren um seinen Ursprung besser zu verstehen. Zum anderen werden wir Vorbereitungen für zukünfitge Missionen treffen um diesen die Beobachtung der Quellregionen des langsamen Sonnenwindes und energiereicher neutraler Teilchen zu ermöglichen.
Die in dieser Arbeit benutzten Beobachtungen wurden von den Sonden Ulysses und ACE aufgenommen und mit einem so genannten Potential Field Source Surface (PFSS) Modell verknüpft. Dieses Modell simuliert das Magnetfeld in der Korona. Damit können wir Schlussfolgerungen über die möglichen Mechanismen ziehen, die für die Freisetzung des Plasmas verantwortlich sind, welches den langsamen Sonnenwind ausmacht.
Für die geplante Mission Solar Orbiter haben wir ein Messschema für das Spectral Imaging of the Coronal Environment (SPICE) Instrument entworfen. Dieses wird es SPICE ermöglichen das Sonnenwindplasma vom Orbit aus an seiner Quellregion auf der Sonne zu beobachten. Das selbe Plasmapacket wird dann später ein weiteres mal in-situ mit einem Partikeldetektor auf Solar Orbiter detektiert. Diese Art von Messung hat das Potential unsere Vorstellung von der Entstehung des Sonnenwindes entscheidend zu erweitern.
Im letzten Teil der Arbeit haben wir geholfen ein Fundament für zukünftige Missionen zu legen, die die neutrale Teilchenkomponente in der Heliosphäre messen werden, indem der Aufbau einer Kalibrationseinrichtung für heliosphärische Teilchendetektoren unterstüzt wurde. Teil dieser Einrichtung sind Faraday Cups, die dafür genutzt werden die erzeugten Teilchenstrahlen zu messen. Die Faraday Cups wurden in dieser Arbeit für die Detektion von neutralen Teilchen kalibriert und dienen nun als Referenzdetektoren für zukünftige Neutralteilchenzähler.

CONTENTS

LIST OF FIGURES

LIST OF TABLES

ACRONYMS

EUV Extreme Ultra Violet

SIR Stream Interaction Regions

ACE Advanced Composition Explorer

PFSS Potential Field Source Surface

GAS Ulysses interstellar neutral GAS experiment

IBEX Interstellar Boundary EXplorer

WSO Wilcox Solar Observatory

KPVT Kitt Peak Vacuum Telescope

MDI Michelson Doppler Imager

SOHO SOlar and Heliospheric Observatory

SPICE Spectral Imaging of the Coronal Environment

FC Faraday cup

SWICS Solar Wind Ion Composition Spectrometer

SWOOPS Solar Wind Observations Over the Poles of the Sun

SWEPAM Solar Wind Electron Proton Alpha Monitor

MAG Magnetometer Instrument

FIP First Ionization Potential

IR Interaction Region

CIR Co-rotating Interaction Region

SI Stream Interface

SDO Solar Dynamics Observatory

VHM Vector Helium Magnetometer

ToF Time of Flight

ESA European Space Agency

ECRIS Electron Cyclotron Resonance Ion Source

LET Low Energy Telescope

HET High Energy Telescope

STROFIO STart from a ROtating Field mass spectrOmeter

ELENA Emitted Low Energy Neutral Atoms

SERENA Search for Exospheric Refilling and Emitted Natural Abundances

MCP Multi Channel Plate

SSD Solid State Detector

SEE Secondary Electron Emission

SE Secondary Electron

SWA Solar Wind Analyzer

CAD Computer Assisted Drawing

1 INTRODUCTION

The interplanetary space around Earth is dominated by the Sun. In addition to being a source for electromagnetic radiation the Sun is also the source of a continuous particle stream. This particle stream is commonly referred to as the solar wind (Hundhausen, 1972) and it predominantly consists of ions and electrons forming a plasma with the embedded solar magnetic field (Borovsky, 2008). Although the solar wind is rather thin with a density of the order of 10 particles per cm^3 at 1 AU distance to the Sun, it nonetheless carves the entire heliosphere out of the interstellar medium. It is therefore the most dominant particle population in interplanetary space. However, there are also other types of particles inside the heliosphere and not all of them are of solar origin. The so called cosmic rays (Potgieter, 2012) consist of extremely high energetic charged particles that enter the heliosphere from the outside. Additionally, there are also neutral atoms of different origin that can be found inside the heliosphere. Some of them have an extrasolar origin and are thought to stem from the local interstellar medium while others are former solar wind that has been neutralized.
Since the first prediction of a solar wind by Parker (1958) and the first measurements in 1959, see for example Gringauz et al. (1960) and for subsequent observations Snyder and Neugebauer (1963), the solar wind has been a subject of intense research. From these and the following measurements we know that it consists mainly of protons ($\approx$ 95%), electrons, a smaller amount of alpha particles and a small amount of heavier ions with mass up to iron (Aschwanden, 2004). In addition there is a magnetic field embedded in the plasma which is transported outwards, see for example Balogh and Erdõs (2013). This magnetic field is directly connected to the solar magnetic field. By now multiple spacecraft have accumulated large amounts of plasma, magnetic and compositional data which revealed that the solar wind is highly dynamic and variable, with its parameters changing on timescales of the order of less than a day or even less than a hour (Gosling et al., 1995). Already early on it was attempted to discriminate the solar wind into different regimes due to the high variability and noticeable correlations between many plasma parameters. The earliest discrimination divided it into two regimes (Bame et al., 1977). It was noticed that there are fast and slow solar wind streams, where the fast streams consist of lowly charged ions and a low proton density but a high proton temperature while the slow streams consist of highly charged ions and a high proton density but a low proton temperature. These two types were accordingly labeled fast and slow solar wind. The differences in the solar wind properties point to different properties of their respective source regions. The general source for the solar wind is the Sun's corona, which in itself is highly structured and variable. Certain areas in the corona have been identified as the source regions for the fast solar wind, see Nolte et al. (1976). These regions are the so called coronal holes (Altschuler et al., 1972), i.e. areas that appear dark in Extreme Ultra Violet (EUV) images of the corona, where the local plasma parameters match the in-situ measured parameters of the solar wind. In contrast to other regions on the Sun the coronal holes are dominated by open magnetic field lines which extend into the heliosphere and enable the outflow of the solar wind plasma (Krieger et al., 1973).

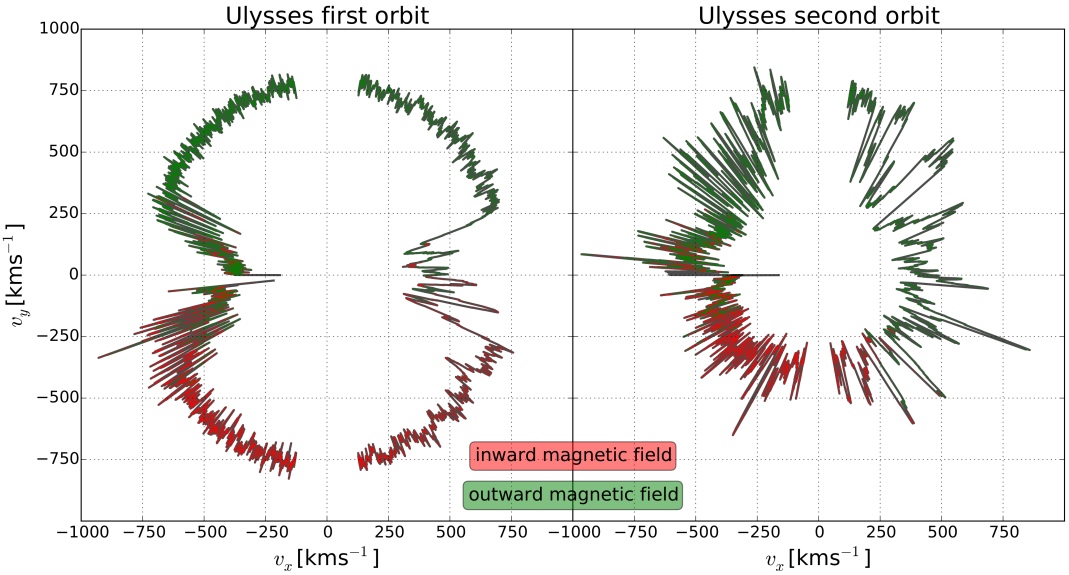

Figure 1: The x and y component of the solar wind speed, where x and y form a plane perpendicular to the ecliptic. The left panel shows the speeds measured during Ulysses first complete orbit, the right panel those measured during the second complete orbit. The colors discern between inward and outward directed magnetic field. Plot based on Figure 1 in McComas et al. (1998b)

The famous Ulysses mission (Wenzel et al., 1992) confirmed the coronal holes as sources for the fast solar wind when it flew over the large polar coronal holes of the Sun during its first orbit and exclusively observed fast solar wind (McComas et al., 2000). In figure 1 these measurements of the solar wind speed are shown. The left panel shows the measurements during Ulysses' first orbit. It can be seen that over the equatorial regions of the Sun a mixture of fast and slow solar wind is observed, while over the poles exclusively fast solar wind is measured. EUV images show that during that time the poles were completely covered by coronal holes (Nolte et al., 1978). The right panel, showing the measurements during the second orbit, displays a completely different behavior. The reason for this is the activity of the Sun. During the quiet phase of the Sun the coronal holes are situated mainly at the solar poles. During the active phase these polar coronal holes are heavily distorted and coronal holes can occur everywhere on the Sun. The second orbit of Ulysses happened during the active phase.

In contrast to the fast solar wind the exact source regions of the slow solar wind remain elusive, see Antiochos et al. (2011) and Fisk et al. (2003) for examples for different hypotheses of the origin of the slow solar wind. The parts of the corona where the local plasma parameters match the in-situ parameters are regions with closed magnetic field lines. Inside these regions, due to a hotter and denser electron population, the ions can reach the high charge states which are later measured inside the slow solar wind streams. But because the closed magnetic field lines do not extend into the heliosphere the plasma is essentially trapped close to the Sun and cannot escape. Additionally, unlike the coronal holes, these regions are highly structured and inhomogeneous. Hence it is neither known where the precise location of the slow solar wind's origin lies on the Sun nor what physical processes are responsible for the release of the hot plasma from the closed field line regions.

In order to lift the veil above the slow solar winds origin many approaches have been undertaken including in-situ and remote-sensing observations as well as simulations of the solar corona and the solar wind propagation, see for example Neugebauer et al. (1998). The in-situ observations include particle observations as well as magnetic field measurements. These measurements help us to understand the characteristics of different solar wind types. As mentioned above, velocity, density and charge state composition mainly define the different plasma streams, but they also help us to understand the dynamics of the solar wind. After emerging from the Sun the solar wind is far from being constant. Different plasma streams interact with each other and form the so called Stream Interaction Regions (SIR) where boundaries between fast and slow streams develop (Wimmer-Schweingruber et al., 1997). The magnetic field measurements give insight into another field of dynamics inside the solar wind. Parker (1958) predicted an interplanetary magnetic field in form of an Archimedean spiral. While on long term average this is true, the magnetic field is extremely variable on short terms. In any case, the field lines found in the solar wind plasma are still connected to their solar foot points. Alfvénic waves injected at the Sun propagate along the field lines out into the heliosphere, constantly shifting and distorting the field lines and potentially exchanging energy with the particles (Marsch, 2003). Due to all these interactions the solar wind is difficult to grasp and conclusions on its origin are challenging to make. To better understand the birthplace of the slow solar wind, i.e. the solar corona, several remote sensing instruments take spectral images of the Sun and the corona, see for example Giordano et al. (2000). These spectrograms contain information about the local plasma density and temperature and to a minor degree about the magnetic field strength and shape. As mentioned above the comparison between these local parameters and the in-situ parameters already contain some important correlations. The spectrograms are always based upon line-of-sight measurements and therefore are always subject to uncertainties. Unfortunately no local measurements of the corona and its magnetic field are available. Hence, the precise structure of the magnetic field lines is unknown to us. For the release of the slow solar wind plasma from the closed field line regions the field line structure is believed to play an important role, because the plasma inside the corona is bound to the magnetic field. In order to fill the lack of local magnetic measurements, simulations are made which model either the magnetic topology or the evolution of the solar wind plasma inside the corona.

Regarding the energetic neutral atoms inside the heliosphere there are much less direct observations available when compared to the solar wind. Examples for instruments that did measure the neutral component are the Ulysses interstellar neutral GAS experiment (GAS) (Witte et al., 1992) or the Interstellar Boundary EXplorer (IBEX) mission (McComas et al., 2004). Indirect observations of neutral atoms have mainly been made by pick-up ions measurements. Pick-up ions are former neutral atoms that have been ionized by solar ultra violet radiation or charge exchange processes with the solar wind (Möbius et al., 1985). They are often observed by solar wind particle detectors and are distinguished from the latter due to their charge state and velocity distribution. Usually pick-up ions are singly charged in contrast to the highly charged solar wind. Regarding their velocities, some pick-up ions have a velocity distribution that mimics that of the solar wind. These so called inner-source pick up ions are thought to be neutralized and subsequently recharged solar wind. Others have a velocity distribution that ranges from 0 to 2

times the solar wind speed. These are interstellar pick-up ions that originate from neutral atoms that have entered the heliosphere from outside.
In this work both the slow solar wind and neutral atoms in the heliosphere are covered, with an emphasis on the former. To really understand the origin of the solar wind streams a combination of in-situ and remote observations and simulations must be applied. For this purpose the in-situ measurements are mapped back to the outer border of the corona by a ballistic approach. Here, the solar wind is mapped further down to the photosphere along the magnetic field lines which have been modeled by a suitable model. Such a model usually uses the photospheric magnetic field as input parameter, which can be obtained by remote line-of-sight measurements. This is what the first part of this work attempts to do. For this purpose in-situ measurements from the Ulysses spacecraft and the Advanced Composition Explorer (ACE) (Stone et al., 1990) are used, together with a so called Potential Field Source Surface (PFSS) model (Altschuler and Newkirk, 1969). The PFSS model uses input magnetograms measured from either ground based observatories like the Wilcox Solar Observatory (WSO) (Bogart and Scherrer, 1986) or the Kitt Peak Vacuum Telescope (KPVT) (Livingston et al., 1974) or from the spacecraft based Michelson Doppler Imager (MDI) (Hoeksema et al., 1988) on the SOlar and Heliospheric Observatory (SOHO) (Domingo et al., 1995). As a novel attempt, not only the photospheric origin of the back mapped solar wind is investigated, but also the course of the field lines through the corona is studied. This includes the bending and twisting of the field lines to the analysis. Especially the spatial behavior of the open field lines with respect to the adjacent closed field lines is examined. These closed field lines mark the border of the open field line regions, i.e. the coronal holes. The coronal hole borders have long been suspected to be the source for at least some of the slow solar wind streams. This work was able to confirm this assumption. In addition we were able to add the shape of the solar winds source field lines as an additional parameter determining the solar wind type associated to the respective field lines. In the second and third part of this work the focus lies on supporting future missions that are going to explore the heliosphere. While the second part is about a very specific mission, namely Solar Orbiter (Müller et al., 2013), the third part will help several upcoming missions, because here a calibration facility for spacecraft based instrumentation is established. In this facility, many constituents of the heliospheric particle populations can be created, including energetic neutral atoms.
Specifically for the upcoming Solar Orbiter mission and the Spectral Imaging of the Coronal Environment (SPICE) instrument (Fludra et al., 2013) the tools at hand are used to devise a special measurement scheme. Solar Orbiter will orbit very close to the Sun, below 0.3 AU and it will combine remote-sensing and in-situ instrumentation on one spacecraft. One mission goal will be to find the source of the slow solar wind. For that purpose it is planned to remotely observe the sources on the solar surface and later observe the corresponding solar wind in-situ at the spacecraft. To do that correctly the devised measurement scheme has to be applied to ensure that time and location of the remote observation align with the in-situ observation.
Regarding the calibration facility a Faraday cup (FC) is calibrated to be used as a detector for neutral particles. Since a FC naturally measures impinging current and a beam of neutral atoms does not carry such it is not suited to be used as a neutral detector out of the box. Nevertheless, the secondary electron emission that is in-

duced by primary particles entering the FC can be used to detect neutral atoms. If the energy dependent secondary electron emission coefficient is determined, a FC can even be used to measure absolute fluxes of energetic neutral atoms. As such it can be used as a reference detector for future spacecraft based neutral particle detectors.

2 THE SOLAR WIND

The magnetized energetic plasma which fills the interplanetary space is called the solar wind. The source of this continuous supersonic plasma flow from where it streams radially outwards is the Sun's atmosphere. The extent of the solar wind determines the so called heliosphere, which forms a cavity inside the surrounding interstellar material. This interstellar medium is also a magnetized plasma of an extrasolar origin. Because of the different magnetic field in the interstellar medium and the heliosphere both plasmas cannot permeate each other, leading to a boundary called the heliopause.
All data shown in this chapter, if not taken from external publications, were measured by the Solar Wind Ion Composition Spectrometer (SWICS), see Gloeckler et al. (1998), the Solar Wind Electron Proton Alpha Monitor (SWEPAM), see McComas et al. (1998a) and the Magnetometer Instrument (MAG), see Smith et al. (1998), on ACE or by SWICS (Gloeckler et al., 1992) and the Solar Wind Observations Over the Poles of the Sun (SWOOPS) instrument on Ulysses, see Bame et al. (1992). The instrumentation will be described in more detail in chapter 4.

2.1 PHENOMENOLOGY OF THE SOLAR WIND

In this section the observable values of the solar wind are described. This includes the chemical and charge-state composition, the plasma parameters and the magnetic field. In addition to that the discrimination of the solar wind into different types is introduced. Historically, the solar wind has been divided into fast and slow solar wind, as measured by the proton velocity v_p, as in Parker (1965) or Bame et al. (1977). With more spacecraft data available it turned out that the discrimination into two types is not comprehensive enough and the solar wind is better described having three or more different types. Xu and Borovsky (2015) propose four kinds of solar wind, namely coronal hole, streamer belt, sector reversal wind and ejecta, which are defined by their plasma parameters. A different approach is done by von Steiger et al. (2010), who discriminate the solar wind by its charge state composition, mainly the count rate ratios of O^{7+} to O^{6+} and C^{6+} to C^{5+}.
In this work primarily the discrimination by Xu and Borovsky (2015) is used. If not stated otherwise, streamer belt and sector reversal wind are taken together in slow solar wind and fast solar wind is synonymous with coronal hole wind.

2.1.1 *Chemical Composition of the Solar Wind*

The solar wind consists mainly of protons, electrons and alpha particles. In addition to this, there are also heavier ions with masses up to iron and beyond as well as a component consisting of neutral atoms. The precise chemical composition of the solar wind is still researched and not fully understood yet. This is because in-situ data from spacecraft based mass spectrometers are difficult to analyze regarding absolute quantities. The main reasons for these difficulties are element depending

instrument efficiencies which are not well enough known and, for some spacecraft, complicated phase space coverage due to the spin of the spacecraft. For ions heavier than helium the count rates are often insufficient to reliably extract the elemental abundance. A more reliable source for the chemical composition of the solar wind are spectroscopic analyses of the corona or photosphere. In table 1 the abundance of some typical elements in the corona is shown. The existence of the

Element	Abundance	Abundance [ppm]
H	12	-
He	10.93	85113
O	8.8	630
C	8.5	316
N	7.9	79
Mg	7.6	40
Fe	7.6	40

Table 1: The relative abundance of the most abundant elements in the solar corona relative to Hydrogen. The second column gives the abundance on a logarithmic scale, $12 + log_{10}(A/A_H)$, with A/A_H being the abundance ratio of a specific element to Hydrogen. The third column gives the abundance in terms of parts per million with respect to Hydrogen as a more tangible number. Values taken from Grevesse and Sauval (2000)

so called First Ionization Potential (FIP) effect (Geiss et al., 1995) prevents one to simply transfer these numbers to the solar wind. The FIP effect is later described in section 2.2. It states that ions with a low FIP can be overabundant in the solar wind with respect to the corona and even more so to the photosphere.
The neutral atoms found in the heliosphere are particularly interesting. They are not associated directly with the solar wind and they have been seldom directly measured up to now. Alongside the few direct observations, their existence is confirmed by the observation of so called pick-up ions Möbius et al. (1985). Some neutral atoms inside the heliosphere have an extrasolar origin, namely the interstellar medium. Additionally, there is another population of neutral atoms that stem from neutralized solar wind. Pick-up ions that emerge from these neutrals are called inner-source pick up ions Geiss et al. (1996). The existence and observation of neutral atoms in the heliosphere will be discussed in more detail in chapter 7.

2.1.2 *Plasma Parameters of the Solar Wind*

The plasma properties of the solar wind have been measured for many years by multiple spacecraft, see for example Galvin et al. (1993). The main parameters are summarized in table 2. Here the parameters are already categorized into slow and fast solar wind. In reality the categorization of the solar wind is not that simple and the parameters are much more variable than table 2 might indicate, this will later be discussed in section 2.2. In figure 2 a time series of in-situ measured solar wind parameters is shown. The data were measured in the ecliptic plane by ACE, it can be seen that the solar wind is highly structured on time scales larger than $\sim$

	slow wind	fast wind
proton speed v_p [kms^{-1}]	∼350	∼700
proton density n_p [cm^{-3}]	∼10	∼4
proton temperature T_p [10^{5}K]	∼0.5	∼5.7
count ratio O^{7+}/O^{6+}	∼0.16	∼0.018
count ratio C^{6+}/C^{5+}	∼1.21	∼0.315

Table 2: Table listing some important solar wind parameters. The first row gives the proton speed. Density and temperature also refer to protons. The ratios O^{7+}/O^{6+} and C^{6+}/C^{5+} are count-rate ratios. These data samples are taken from Ulysses/SWOOPS and SWICS at ∼1.5 AU.

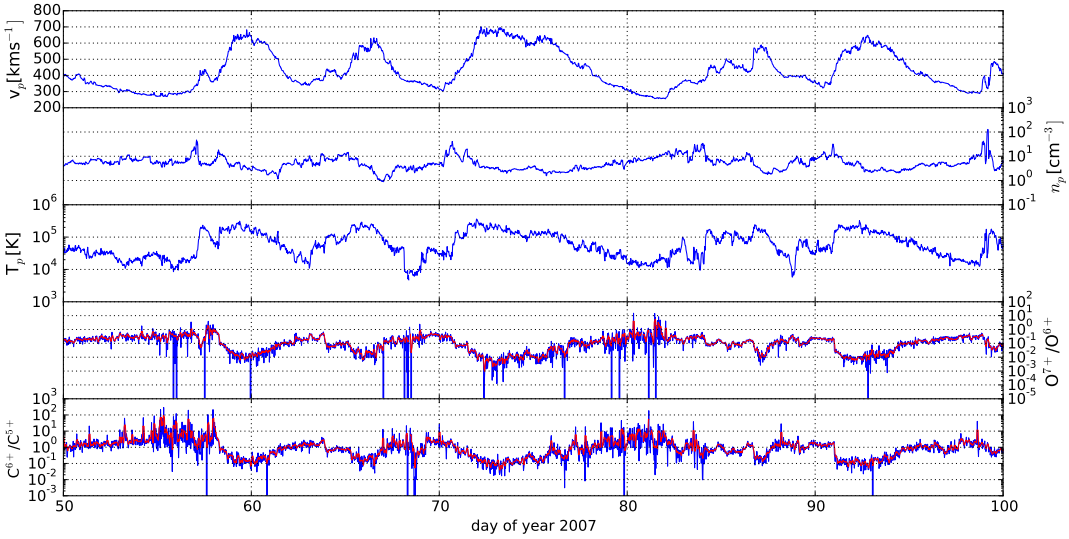

Figure 2: A time series of the same solar wind parameters as shown in table 2. The blue curves show 30 minute data and the red curves are averaged on 2 hour intervals. The high variability of the parameters as well as the correlation between them is noticeable. All data was measured by ACE/SWEPAM and SWICS.

1 day. It is also noticeable that there is a correlation between some and respectively an anti correlation between other parameters. The proton density and the charge state ratios are anti correlated with the solar wind speed while temperature and speed are correlated. As we will later see this is a direct result of the different origins of the solar wind inside the corona.
Another important parameter of the solar wind is the embedded magnetic field, which will be discussed in the next subsection.

2.1.3 *The Heliospheric Magnetic Field*

The plasma which makes up the solar wind is interspersed with a magnetic field at all times and everywhere inside the heliosphere. It is actually a remnant of the magnetic field inside the corona (Borovsky, 2008) which is frozen in inside the solar wind plasma and carried outwards into the heliosphere (Owens and Forsyth, 2013). Meanwhile, the foot points of these field lines are still connected to the

photosphere. Due to the rotation of the Sun the field lines are coiled up and form a spiral-like structure called the Parker Spiral, see Parker (1958). This spiral is shown in figure 3. It can be seen that there is a difference for fast and slow solar wind.

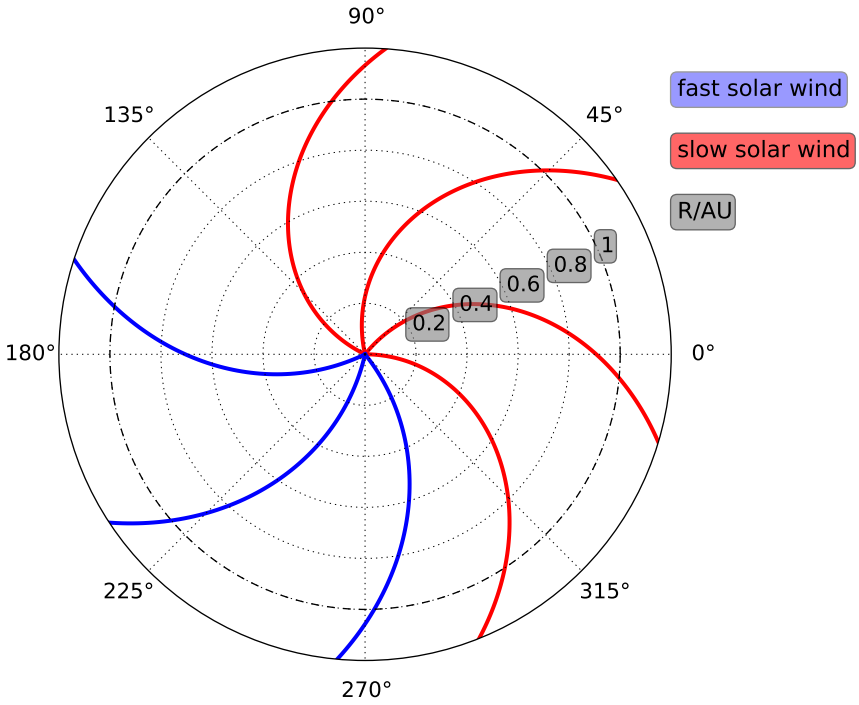

Figure 3: A schematic top down view on the ecliptic plane with the Sun in the center in polar coordinates. The radius gives the distance to the Sun in AU, the angle shows the heliospheric longitude. The blue and red lines represent the Parker Spiral for fast (blue) and slow solar wind (red). The dashed line marks the Earth's orbit at 1 AU.

The magnetic field lines in the fast solar wind are less coiled up when compared to the slow solar wind, resulting in a smaller angle between the magnetic field line and a radial line. The expected field line angle at 1 AU is often referred to as the Parker angle and is $\approx 45°$, depending of course on the solar wind speed. Measurements of the heliospheric magnetic field show that the Parker angle is only an approximation in reality. For additional information about the interplanetary magnetic field see for example Smith (1989) for measurements farther out in the heliosphere or Forsyth (1995) for high latitude measurements. In figure 4 magnetic field measurements made at 1 AU by ACE are shown. Two distinct features can be seen around 45° and accordingly around 225°. This illustrates that both inward and outward polarity of the magnetic field can be measured. It also shows that the Parker angle is only an average. The actual magnetic field angle depends primarily on the solar wind speed v_{sw} and the distance to the Sun R. It can be calculated according to

$$cos(\phi) = \frac{1}{1 - (\omega R / v_{sw])^2}} \ , \tag{1}$$

although this formula is only valid inside the ecliptic plane. Outside of the ecliptic plane the structure of the magnetic field becomes more complicated. In addition to equation 1 the actual field is disturbed by Alfvén waves which travel along the

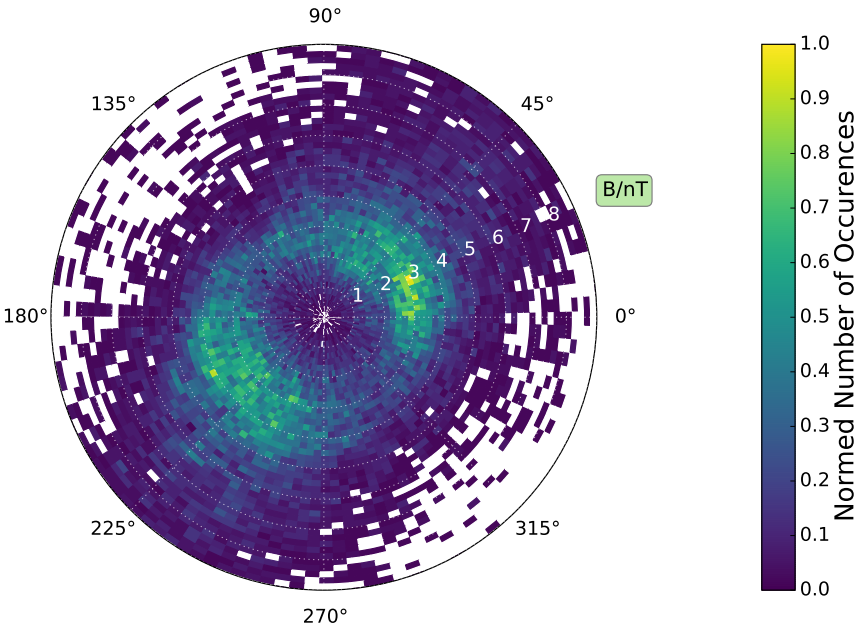

Figure 4: The heliospheric magnetic field measured by ACE/MAG over the year 2007. The radius give the field strength in nT and the angle is measured between field line and the radial direction with 0° pointing away from the Sun. The color coding represents the normed number of occurrences.

field lines. Those are either of solar origin or are induced locally by wave particle interaction. For more information about heliospheric plasma waves see Gary (1993).
Regarding the shift in polarity which can be seen in figure 4 this is due to the global shape of the interplanetary field. The Sun and consequently its magnetic field can be approximated as a dipole field. Respectively one hemisphere of the heliosphere is populated by inward directed magnetic flux while the other hemisphere contains outward directed flux. The border between the polarities is called the heliospheric current sheet. Interestingly, the magnetic polarity of the Sun reverses approximately every 11 years.

2.1.4 *Spatial Structure of the Solar Wind*

Due to the rotation of the Sun there are characteristic structures in the solar wind which form naturally. Unlike the magnetic field in figure 3 suggests, the solar wind streams radially away from the Sun as soon as it passes a certain point in the corona, the so called Alfvénic point (Hundhausen, 1972), where the kinetic pressure of the plasma surpasses the magnetic pressure. In case of a non rotating Sun the global picture of the solar wind would probably be a very simple one, since each source location on the Sun simply emits its specific solar wind type radially outward. But since the Sun is rotating with a sidereal period of 25.38 days the source regions continue to rotate with the Sun while the solar wind itself is decoupled from the Suns rotation. This leads to the case where the source of slower solar wind lies behind a stream of previously started fast solar wind and vice versa. The fast solar wind then runs either ahead of the slow solar wind or it runs into the slow solar wind, leading to so called compression and rarefaction regions

(Hundhausen, 1972). In figure 5 this effect is shown as observed at 1 AU distance

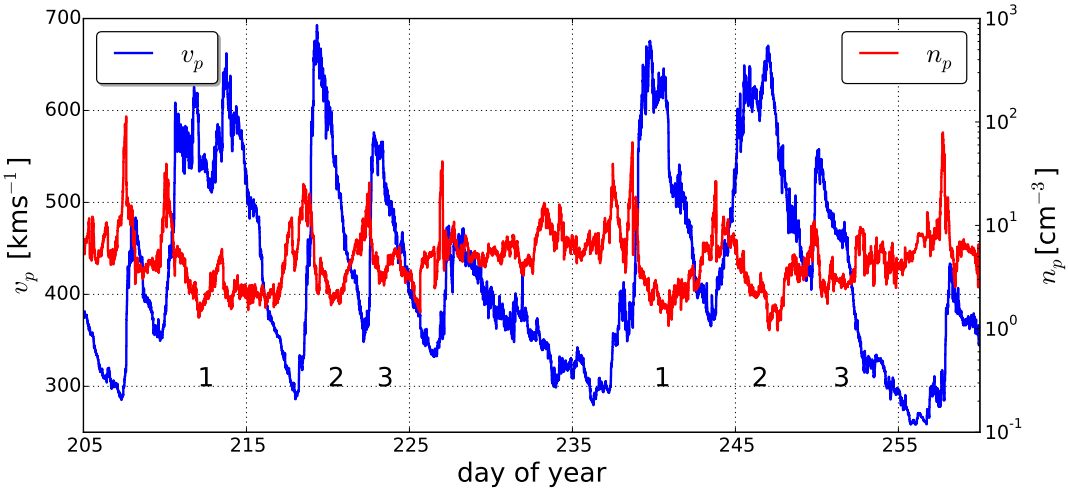

Figure 5: 50 days of solar wind data taken from ACE/SWEPAM. Shown are the solar wind speed in blue and the density on a logarithmic scale in red. The numbers and shaded areas mark a reoccurring pattern of fast solar wind streams.

to the Sun. The compression regions are identifiable by the peaks in the solar wind density. Here the fast solar wind runs into the slow solar wind. Due to the different magnetic fields both plasma streams cannot permeate each other, therefore both streams are compressed, leading to a higher density. The rarefaction regions are not as distinguishable as the compression regions, as they become more pronounced only farther out in the heliosphere. The regions where fast and slow solar wind meet are called Interaction Regions (IRs). The numbers 1, 2, and 3 in figure 5 mark three consecutive fast solar wind streams and the associated IRs. The marked patterns repeat themselves after a time of ∼27 days. This is commonly observed in the solar wind and is caused by the longevity of the respective source regions in the Sun, which can last for several solar rotations, see for example Whang and Burlaga (1989). Hence these IRs, which are repeatedly observed, are also called Corotating Interaction Regions (CIRs) and they form the most predominant structures in the heliosphere. The precise boundary layer between the two streams are embedded inside the CIRs. These are the so called Stream Interfaces (SIs), where the compositional changes between both streams occur, see Wimmer-Schweingruber et al. (1997) for more information.

2.2 THE SOLAR WIND TYPES

It has been hinted before in section 2.1.2 that the solar wind can be categorized into different types. The first discrimination that has been done was to divide the solar wind into fast and slow solar wind, see for example Bame et al. (1977) or Hundhausen (1973). Fast solar wind has velocities typically larger than 650 kms^{-1} while slow solar wind is in the range of 250 to 400 kms^{-1}.
In this section different categorization schemes and their respective underlying parameters are presented. The velocities given for the fast and the slow solar wind immediately show that this categorization scheme cannot be the end of the story, since all the intermediate velocities are measured as well in reality. Nevertheless

the denotation fast and slow solar wind is widely spread in the community. However, the categorization of the solar wind is probably more complex and is still an ongoing topic of research. At the moment the tendency points to four or more solar wind types.
As already hinted in section 2.1.2 there are certain measures in the solar wind which are used for its categorization, with the velocity being the most prominent one. In addition to that, the charge state composition is often used to discern between solar wind type, see for example Landi et al. (2012). Often there are particular ion pair ratios utilized, like the O^{7+}/O^{6+} or the C^{6+}/C^{5+} ratios. For example von Steiger et al. (2010) use the product of both ratios measured by ACE/SWICS as an especially robust criteria. The advantage of using oxygen and carbon charge

	slow wind	fast wind
$\frac{O^{7+}}{O^{6+}} \cdot \frac{C^{6+}}{C^{5+}}$	< 0.01	≥ 0.01

states as criterion lies in the fact that these elements are very prominent in the solar wind, apart from hydrogen and helium, as seen later in section 4.1.2.
Another measurable parameter in the solar wind which is used to discern between different types is the so called FIP effect. It has been observed that elements with a lower FIP are overly abundant in the solar wind when compared to their photospheric abundance, see Geiss et al. (1995). Figure 6 shows this effect. Here the FIP

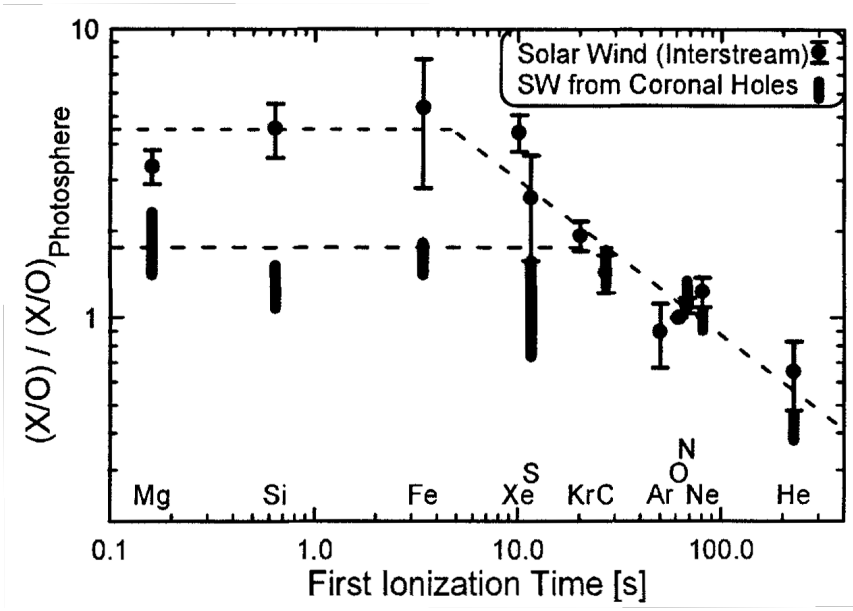

Figure 6: The abundance of certain elements relative to their photospheric abundance as a function of the first ionization time, which is equivalent to the FIP. The two curves represent interstream solar wind (slow) and coronal hole wind (fast). Plot taken from Geiss et al. (1995).

is substituted with the first ionization time which demonstrates the same behavior. Shown are the abundances relative to oxygen of different elements with respect to their photospheric abundance relative to oxygen. It can be seen that the FIP effect can be observed in coronal hole (fast) wind as well as in interstream (slow) solar

wind. But is is much more pronounced in the slow solar wind than in the fast solar wind. Typical elements with a low FIP are iron, magnesium or silicon. A common method to use the FIP effect as a tracer for the solar wind type is to look at certain element ratios, for example Fe/O. On the one hand, oxygen is an element with a high FIP and its abundance seems to be the same in fast and in slow solar wind. On the other hand, the iron abundance has been observed to change with the solar wind type, therefore a higher Fe/O ratio can be expected in slow solar wind. However, the FIP effect is not an easy tracer because the in-situ abundances of low FIP elements are not easy to measure with typical solar wind instruments. Especially magnesium and silicon are notoriously hard to identify. It has to be noted that the FIP effect as presented here is not generally accepted in the community (Nittler et al., 2010). It could very well be that oxygen is less abundant in figure 6, which would lead to the same result.
The so called collisional age A_{col} is another variable that divides the solar wind into different types. It is not a directly measured variable, but calculated from different observables:

$$A_{col} = \frac{r}{\tau v_{sw}} \ , \tag{2}$$

with r being the distance to the Sun and τ being a characteristic time scale on which collisions in a plasma happen. τ depends on the particle species involved in the collisions. For the solar wind most often the proton-proton collision time scale τ_p is used:

$$\tau_p \sim \frac{T_p^{3/2}}{n_p} \tag{3}$$

$$\Rightarrow A_{col} = \alpha \frac{r n_p}{v_{sw} T_p^{3/2}} \ . \tag{4}$$

The prefactor α norms A_c so that it becomes dimensionless, see for example Maruca et al. (2013). The collisional age can be interpreted as the ratio of the time between Coulomb collisions and the travel time to the observer (Kasper et al., 2008). If $A_c \ll 1$ the solar wind is collisionally young, otherwise it is collisionally old. Naturally, the fast wind has a lower collisional age when compared to the slow solar wind.
Another way to categorize the solar wind is employed by Xu and Borovsky (2015). They introduce a categorization scheme using three parameters:

$$S_p = T_p / n_p^{2/3}, \tag{5}$$

$$v_A = \frac{B}{\sqrt{4\pi m_p n_p}} \ , \tag{6}$$

$$\frac{T_p}{T_{exp}} = T_p \left(\frac{258}{v_{sw}} \right)^{3.113} \ . \tag{7}$$

S_p is the proton-specific entropy, v_A is the proton Alfvén velocity T_p/T_{exp} is the ratio of the proton temperature and the expected temperature, which depends on the solar wind speed, see Hundhausen et al. (1970) and Elliott et al. (2005). Obviously, four solar wind quantities must be measured to derive the above parame-

category	Q_1	Q_2	Q_3
ejecta	true	-	-
coronal hole plasma	False	True	-
sector reversal plasma	False	-	True
streamer belt plasma	False	False	False

Table 3: Categorization schemata after Xu and Borovsky (2015). *True* means that the respective condition must be fulfilled, *false* means the opposite. A minus (-) means that the respective condition does not matter for that category.

ters, namely the magnetic field B, the proton density n_p, v_p and T_p. With these four quantities they set up three conditions:

$$Q_1 \equiv 0.841 B n_p^{-0.315} T_p^{-0.222} v_{sw}^{-0.171} > 1 \tag{8}$$

$$Q_2 \equiv 8.77 \times 10^{-11} T_p B^{1.42} v_{sw}^{3.44} n_p^{-2.12} > 1 \tag{9}$$

$$Q_3 \equiv 0.0561 T_p B^{0.752} v_{sw}^{0.445} n_p^{-1.14} < 1 \ . \tag{10}$$

Depending on these three conditions the solar wind is then categorized into *ejecta*, *coronal hole plasma*, *sector reversal plasma* and *streamer belt plasma* as describe in table 3.

The four categories can be understood as the following:

1.) **Coronal hole plasma:** This is what is historically referred to as fast solar wind, which unambiguously originates from a coronal hole.

2.) **Sector reversal plasma:** This is a part of the slow solar wind. It is observed very close to the heliospheric current sheet where the solar magnetic field changes its polarity. In general this type of solar wind is especially slow.

3.) **Streamer belt plasma:** This is what normally falls into the category slow solar wind. It is not of coronal hole origin, highly charged and much denser than coronal hole wind. It can be observed in the equatorial regions above the so called streamer belt.

4.) **Ejecta:** This is anomalous plasma which is not a part of the quiescent solar wind. For example, interplanetary coronal mass ejections fall into this category.

In figure 7 a sketch is shown which illustrates how Xu and Borovsky (2015) roughly picture the source regions for their plasma types. The category ejecta is not shown here since it has no regular source regions. Instead, ejecta are most often produced by active regions or large scale impulsive events on the Sun. The origin of the coronal hole plasma is well determined and to be found at the coronal holes, see Tu et al. (2005). Streamer belt plasma is thought to originate at the boundaries of coronal holes where interactions between the open and closed magnetic field lines can release hot dense plasma, see section 2.3.3.1 for example. Sector reversal plasma is speculated to originate from the cusps of the streamer belt (Wang, 2012). Here the plasma is either released by interactions between open and closed field lines or the top of a loop can pinch of to form a detached plasmoid, see figure 8

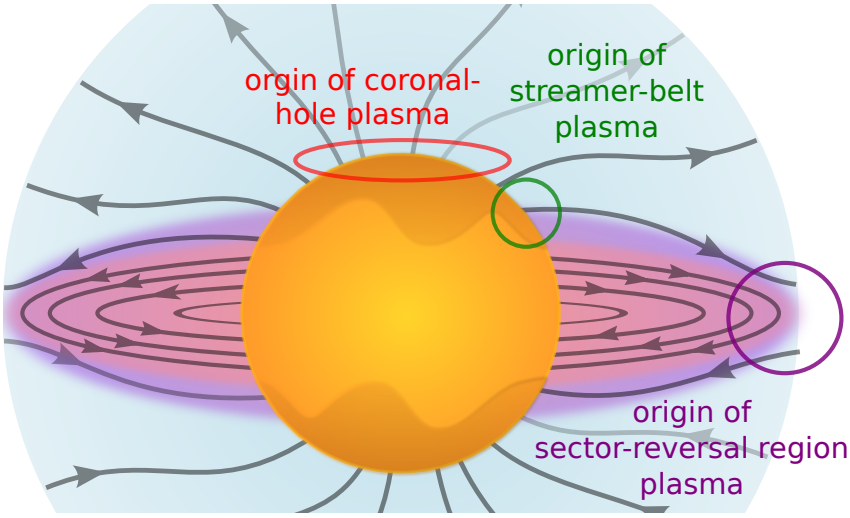

Figure 7: Sketch of the Sun and the surrounding corona. The black lines and arrows indicate the magnetic field lines and their polarity. The source regions for coronal hole plasma (red), streamer belt plasma (green) and sector reversal plasma (lilac) are marked. Plot based on figure 1 in Xu and Borovsky (2015)

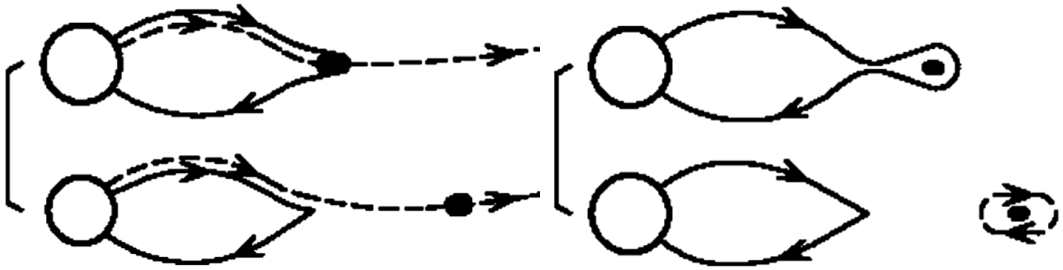

Figure 8: Sketch to illustrate how plasma might be released from closed loops. The Sun is shown as circle, the temporal evolution goes from top to bottom. On the left side a closed field line reconnects with an open field line and on the right side the top of the loop pinches of to form an isolated plasma bubble. Plot taken from Wang (2012).

for clarification. In any case, the mechanisms at work are not well understood and figure 7 is only a basic idea where the different plasma type might originate. The hypotheses around the origin of the solar wind in general and the slow solar wind in particular are discussed in the next section.

This categorization scheme applied to a time series of the solar wind yields a picture as shown in figure 9. It can be seen that ejecta are a relatively rare occurrence which is expected for transient phenomena. Coronal hole plasma can be found in the high speed streams with speeds of $v_{sw} \geq 550\,\mathrm{kms}^{-1}$. The solar wind with lower speeds is classified as streamer belt or sector reversal plasma, with the latter occurring when the magnetic field switches its polarity.

Of all solar wind categories only the origin of the fast solar wind has been definitively identified, hence the name coronal hole plasma is a more appropriate term. Streamer-belt and sector-reversal plasma make up the body of the slow solar wind.

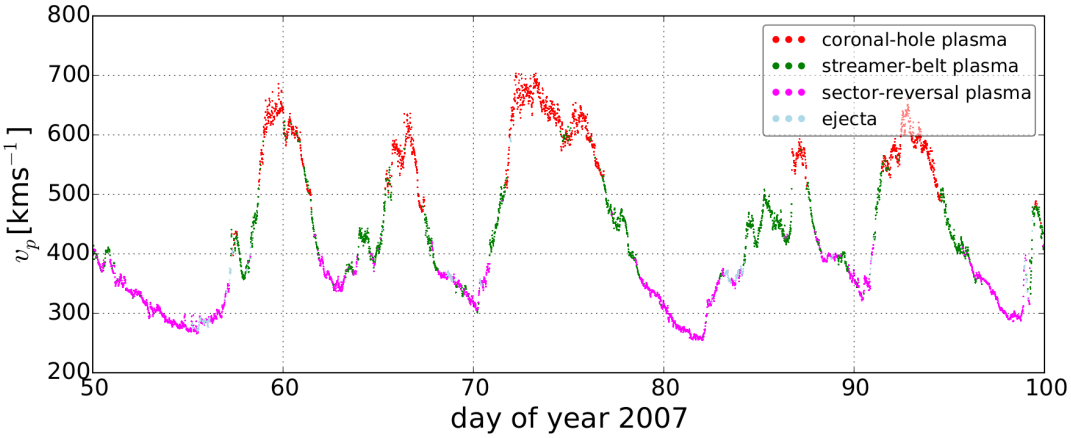

Figure 9: 50 days time series of the solar wind speed observed by ACE/SWEPAM in 2007. The colors correspond to the categorization schemes from Xu and Borovsky (2015)

If not stated differently, in this work slow solar wind means sector-reversal and streamer belt plasma combined.

2.3 SOLAR ORIGIN OF THE SOLAR WIND

The most basic way to understand the solar wind is as the expansion of the solar atmosphere. The first one to recognize the possibility of an expanding corona was Parker (1958). Prior to his considerations the gas in the corona was thought to be in an equilibrium state, leading to a momentum equation:

$$-\frac{dp}{dr} - \rho\frac{GM_\odot}{r^2} = 0 \ . \tag{11}$$

Here r is the distance to the Sun, p is the pressure, G is the gravitational constant, $M_\odot$ is the mass of the Sun and ρ is the mass density. The left term denotes the pressure driven expansion of the gas and the right term gives the gravitational force acting on the particles. Since both terms negate each other the corona is static with an outflow velocity $u(r) = 0$.
Consequently, Parker searched for non static solutions with $u(r) \neq 0$, i.e. allowing the gas to expand. This lead to a modified momentum equation:

$$\left(u^2 - \frac{2kT}{m}\right)\frac{1}{u}\frac{u}{r} = \frac{4kT}{mr} - \frac{GM_\odot}{r^2} \ . \tag{12}$$

T is the coronal temperature, k is the Bolztmann constant and m is the sum of proton and electron mass. In this equation the left side describes the change of $u(r)$ with respect to r. On the right side are two competing terms, $\frac{4kT}{mr}$ describes the temperature driven expansion of the corona and $\frac{GM_\odot}{r^2}$ describes the gravitational bonding of the gases. Considering reasonable temperatures for the corona in the order of 10^6 K, $\frac{4kT}{mr} < \frac{GM_\odot}{r^2}$ holds true for small r, meaning that the lower parts of the corona are bound by gravity. On the other hand, since $1/r^2$ decreases faster with increasing r than $1/r$, the upper parts of the corona are not bound anymore. Past a critical distance $r_c = \frac{GM_\odot m}{4kT}$ the constituents of the corona are free to expand into space. Thereby the equation 12 directly predicts the existence of a solar wind.

2.3.1 *Heating of the Corona*

In the previous subsection the existence of the solar wind was shown to be caused by the thermal expansion of the corona. In order for the first term on the right side of equation 12 to become larger than the second for reasonable distances r, the temperature T of the corona must be of the order of $T \approx 10^6\,\mathrm{K}$. While this is true in reality, the temperatures in the corona range from $\sim 1\,\mathrm{MK}$ to $\sim 3\mathrm{MK}$, see Aschwanden (2004), it is not immediately evident why these temperatures are reached. The energy source of the Sun is the nuclear fusion which takes place deep inside. The Suns core temperature is about 15 MK and decreases towards its surface. The temperature of the photosphere is only around 5800 K. From that it can be inferred that there must be a different process than thermal conduction responsible for the temperatures measured in the corona[1].
The heating of the corona is equatable with the heating of the solar wind and is therefore highly important for the understanding of it. Since the photosphere is so much cooler than the corona, thermal conduction between both regions cannot be the reason for the high temperatures found in the corona. Accordingly, there must be another mechanism of heat transfer at work. Actually coronal heating is not very well understood and is still an ongoing research topic, see for example De Moortel et al. (2008) and Hollweg (1990).
The heat source of the corona can most likely be found in the random motion of the photospheric foot points of the magnetic field lines. This random motion is powered by the convection of plasma packages beneath the photosphere which itself is ultimately driven by the solar dynamo. The foot point motion is transferred into the corona along the magnetic field lines in form of waves, more precisely Alfvén waves. For the corona to be heated by these waves a mechanism is needed to transfer the energy from the waves onto the particles. A possible mechanism for that is ion-cyclotron resonance. When the gyro frequency of the particles Ω and the frequency ω of the wave fulfill the resonance condition

$$\omega(k_\parallel) - k_\parallel v_\parallel = \Omega \ , \tag{13}$$

with $k_\parallel$ being the wave vector and $v_\parallel$ the velocity of the particle parallel to the magnetic field line, see for example Stix (1992) for more information.

2.3.2 *Charge State Composition in the Corona*

The ionic charge state distribution found in the solar wind is practically constant, in other words the solar wind ions do not alter their charge state in the interplanetary medium. The in-situ observed charge states must have been defined inside the corona below a certain distance to the Sun. Above this respective distance they become frozen in (Bochsler, 2000). Inside the corona electron-ion collisions are the main driver for the ionization, while photo ionization can be neglected. In figure 10 the temperature and density profile for coronal electrons as function of the distance to the Sun is shown. Looking at the radial dependence it is evident that the charge state composition of the solar wind must freeze in at certain point, since electron temperature and density decrease considerably with heliocentric distance. Ions traveling through the corona experience an ongoing mixture of ionization and

1 This problem is frequently referred to as: 'How can the pan be hotter than the stove plate?'

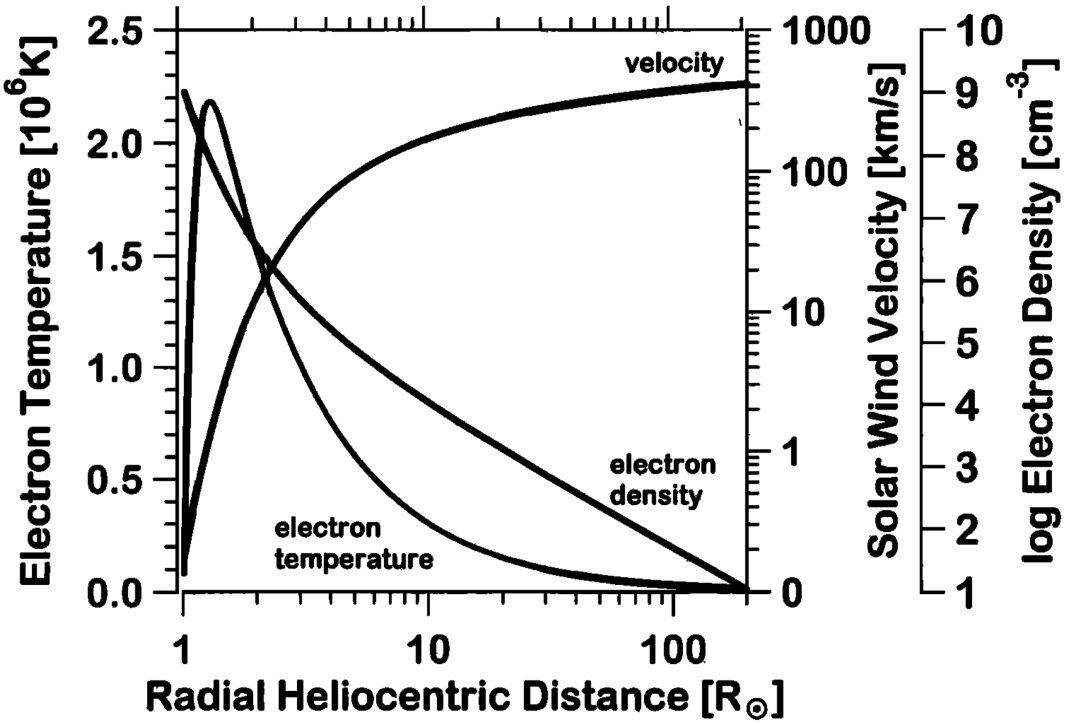

Figure 10: Here the electron density, temperature and the solar wind velocity are shown as a function of the radial distance to the Sun. Plot taken from Bochsler (2000)

recombination. Since the overall number of particles must be conserved, for each ionization state i of an element X

$$\nabla(n_i u_i) = n_e \left[n_{i-1} C_{i-1} + n_{i+1} R_{i+1} - n_i \left(C_i + R_i \right) \right] \quad , \tag{14}$$

where n and u are the density and bulk velocity and R and C are the recombination and ionization rates and n_e is the electron density. Two adjacent ion species X^i and X^{i+1} are coupled together via C_i and R_{i+1}. The timescale on which they interact with each other is given by

$$\tau_{i \leftrightarrow i+1} = \frac{1}{n_e (C_i + R_{i+1})} \quad . \tag{15}$$

It can be seen that the ionization-recombination time $\tau_{i \leftrightarrow i+1}$ increases with decreasing electron density until the ion pair effectively stops interacting (Bochsler, 2000). In order to provide an idea how this translates to the reality of the expanding corona figure 11 shows the evolution of oxygen charge states. The upper panel shows the temperature profile, while each of the other panels shows the fraction of one oxygen charge state with respect to the total quantity of oxygen. At the photosphere at $1\,R_\odot$ neutral oxygen is injected which then rapidly ionizes with increasing height and quickly reaches O^{6+} as dominant charge state. With further increasing height some of the O^{6+} ionizes to O^{7+} and even O^{8+}. Although the temperature here is high enough to allow fully ionized oxygen the electron density has decreased to the point that the ionization-recombination time surpasses the expansion time of the oxygen ions and the charge states freeze in at roughly $1.65\,R_\odot$. From what has been in shown in section 2.1.2 in-situ observations of fast and slow

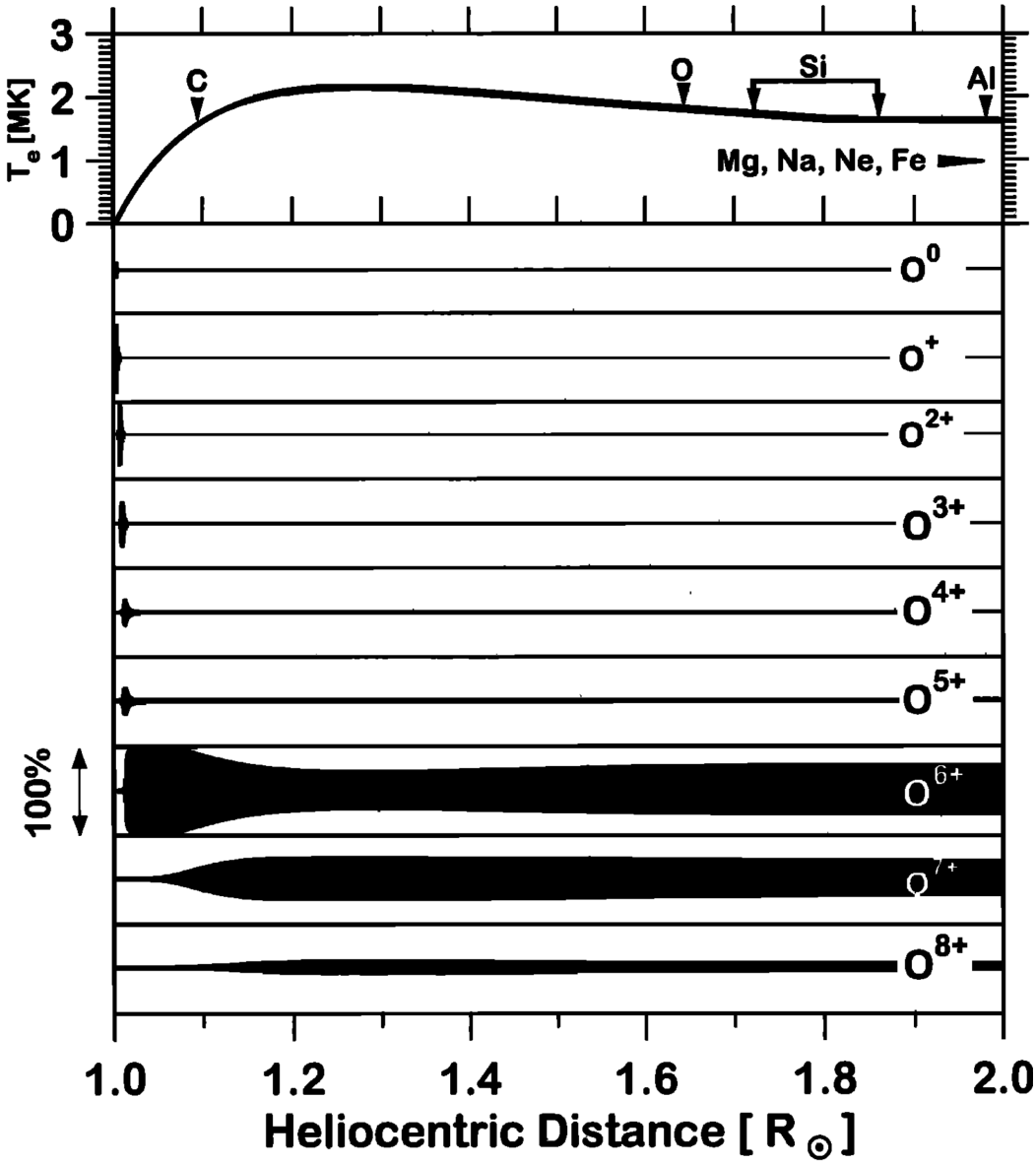

Figure 11: The evolution of oxygen charge states shown as a function of the heliocentric distance. The upper panel shows the expected electron temperature in MK. Here the freeze-in heights for different elements are marked. The lower panels show the fractions for different oxygen charge states with respect to the total amount of oxygen. Plot taken from Bochsler (2000)

solar wind show different charge state compositions. From that it can be inferred that both solar wind types must originate from different source regions on the Sun. The higher charged slow solar wind must come from regions where the electron temperature and density is considerably higher when compared to the sources of the fast solar wind.

2.3.3 *Source Regions for Fast and Slow Solar Wind*

The precise origin of the slow solar wind is still an ongoing topic of active research. Nevertheless there are various hypotheses regarding the source regions which are explored in this section. As already described in chapter 1, the source for the fast solar wind has been most certainly determined. Figure 1 reveals the coronal holes as the origin. Here the coronal conditions, especially the charge state composition, match the in-situ parameters. Inside coronal holes the temperature is $\sim 1\,\mathrm{MK}$. Looking at figure 11 this is consistent with O^{6+} being the dominant charge state of oxygen. This can be seen in figure 12, where the correlation between the O^{7+}/O^{6+}

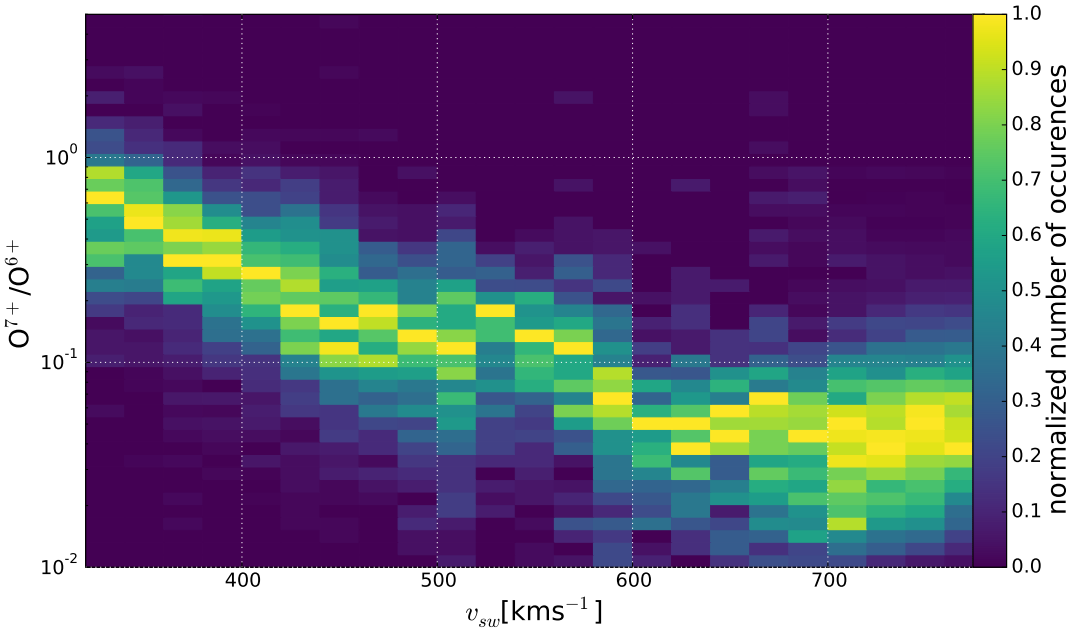

Figure 12: A 2d histogram showing the correlation between the O^{7+}/O^{6+} ratio in logarithmic scale and the solar wind speed. The color coding shows the counts normalized to the maximum of each column of bins. The underlying data were obtained by Ulysses over the year 1995.

ratio as a proxy for the charge state composition and the solar wind speed is shown in form of a 2d histogram. For solar wind speeds of $600\,\mathrm{kms}^{-1}$ and greater the majority of oxygen ions is sixfold charged, while for the slow solar wind the ratio between the charge states can reach 1 and greater. The same behavior can be seen for other ion pairs.

The origin of the slow solar wind is problematic because its charge-state composition matches regions of the corona which are dominated by strong magnetic fields that form large loop-like structures. Figure 13 shows a superimposition of three EUV wavelengths captured by the Solar Dynamics Observatory (SDO) (Pesnell et al., 2012). The displayed wavelengths belong to the emission lines of certain iron ions in the corona, namely Fe^{8+}, Fe^{11+} and Fe^{13+}. Because of that the brightness in the image is a measure for the particle density, or to be more precise the density of the respective iron ions. It is also a measure for the local electron density and temperature. In this representation the coronal holes are visible as dark regions, since here the density as well as the temperature is lowest. Since this is an image from the quiet Sun the coronal holes are situated predominantly at the poles of the

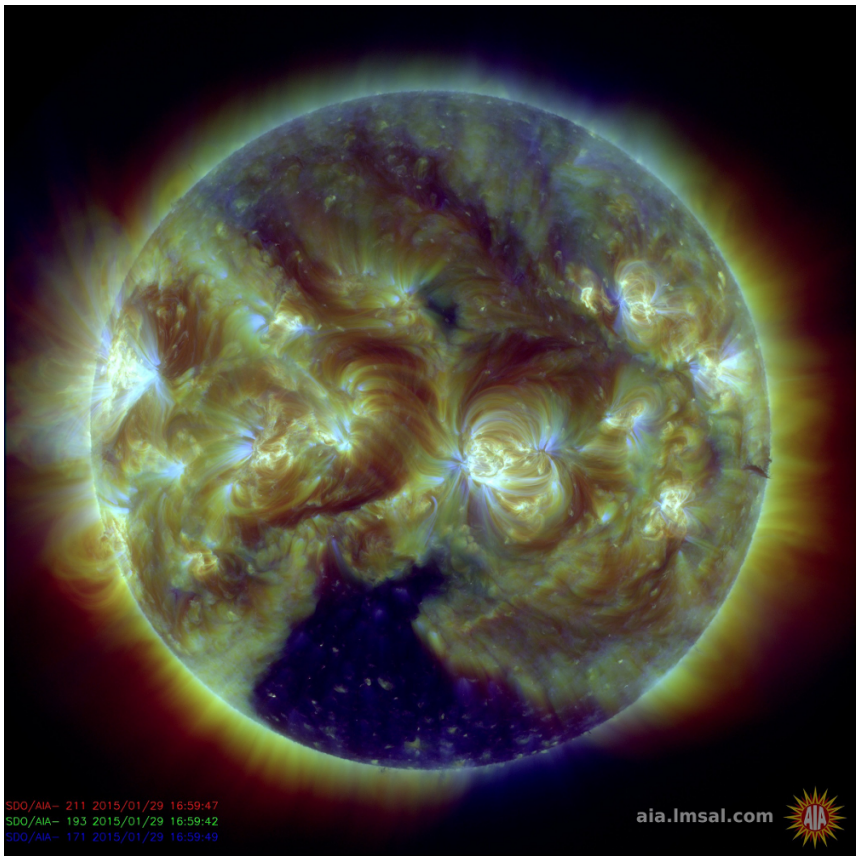

Figure 13: A false color image of the Sun showing three superimposed EUV wavelengths. The brightness is a measure for the local particle density. Source: Courtesy of NASA/SDO and the AIA, EVE, and HMI science teams.

Sun, which is in nice agreement with the solar wind speed observations made by Ulysses, as seen in the left panel of figure 1. Although the Ulysses measurements were made in 1995, in contrast to the image in figure 1 which is from 2015, in both cases the Sun was in its quiet phase. The bright regions on the contrary form a band around the solar equator. Inside these bright regions the magnetic loops are apparent. It is inside these loops were the birthplace of the slow solar wind is presumed (Zurbuchen et al., 2012). But in contrast to the coronal holes, where open magnetic field lines expand into space, here the loops are closed, meaning the plasma cannot freely expand into the heliosphere. This can be quantized by the plasma-β parameter, the ratio between kinetic and magnetic pressure:

$$\beta = \frac{p_{kin}}{p_{mag}} = \frac{nk_BT}{B^2/2\mu_0} \quad . \tag{16}$$

The plasma-beta is a crucial parameter that governs the behavior of a magnetized plasma. If $\beta < 1$, so called cross-field diffusion is prohibited, meaning particles are less likely to escape their magnetic confinement. Only if $\beta \geq 1$ particles can overcome magnetic confinement, see Aschwanden (2004). Inside the closed loops ions typically do not reach regions with $\beta \geq 1$, hence they are trapped. Because they are measured in the slow solar wind there must be some kind of mechanism which can distribute these ions onto the open field lines so that they can contribute

to the solar wind.

2.3.3.1 *Coronal Hole Boundary Wind*

The slow solar wind's properties suggest an origin in the closed field line regions, but here the particles cannot easily escape their magnetic confinement. The regions where ions can readily flow into the heliosphere are the open field line regions of the coronal holes. Naturally, there are regions on the Sun where open and closed magnetic field lines are adjacent to each other. From that it follows to investigate the border region between coronal holes and closed field lines regions. To get an idea how the solar wind in the heliosphere would be shaped Schwadron et al. (2005) developed a model that calculates the distribution of different solar wind speeds considering a consistent source region distribution on the Sun. Figure 14

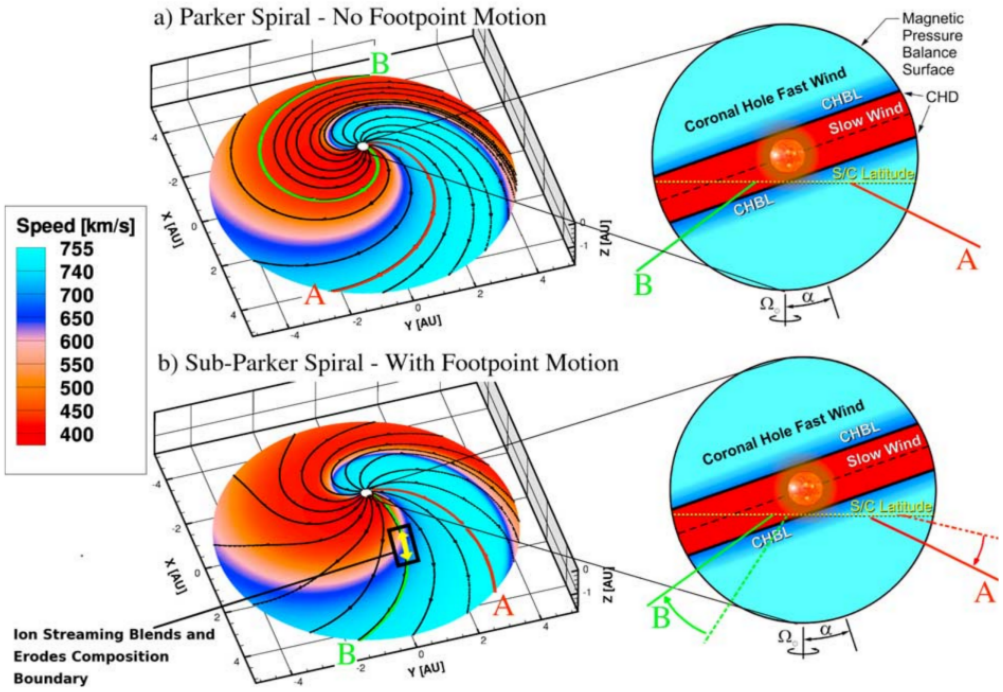

Figure 14: Solar wind speed distribution modeled by a magneto hydrodynamic model. The color coding gives the solar wind speed. On the left side the speed distribution in the heliosphere is shown, the black lines are the magnetic field lines. On the right side the sources for the different solar wind speeds are displayed on the surface of a sphere with a radius of 30 $R_\odot$ around the Sun with the same color coding. The plot was taken from Schwadron et al. (2005).

shows the result of their model. The black lines are the magnetic field lines, which form the Parker spiral. The distribution of the solar wind speeds correspond on a first approximation with the picture observed in reality, as seen in section 2.1.4. Fast and slow solar wind interact with each other forming CIRs. In the model the slow solar wind originates from a band around the solar equator, but the question how it breaks free from the closed loops is still unanswered. Regarding this point Schwadron et al. (2005) hypothesize about the random foot point motion of the

magnetic field lines which can transport open magnetic flux into the closed loop regions. Zhao et al. (2009) were dealing with the same problem in their study of the global distribution of the solar wind. They essentially divide it into coronal hole wind and non coronal hole wind and conclude that non coronal hole wind originates from a narrow band around the heliospheric current sheet. Similar to Schwadron et al. (2005) they propose foot point motion which drives the open flux from the coronal holes to the base of the heliospheric current sheet, which can be basically equated with the closed loop regions. Once the open flux has been carried there the plasma from the closed loops must be distributed onto the open field lines. For this Zhao et al. (2009) propose magnetic reconnection between open and closed field lines. By that the highly charged material can be released into the heliosphere.

2.3.3.2 *The S-Web*

A different approach has been made by Antiochos et al. (2011). They propose that the sources for the slow solar wind lie in a network of narrow channels which are filled with open magnetic flux. These channels are thought to connect seemingly separated coronal holes among each other. Indeed they speculate that all coronal holes are connected with each other, i.e. isolated coronal holes do not exist. This network of open-flux channels then maps to a web of separatrices in the heliosphere, consequently called s-web. Figure 15 helps to illustrate the idea. Here

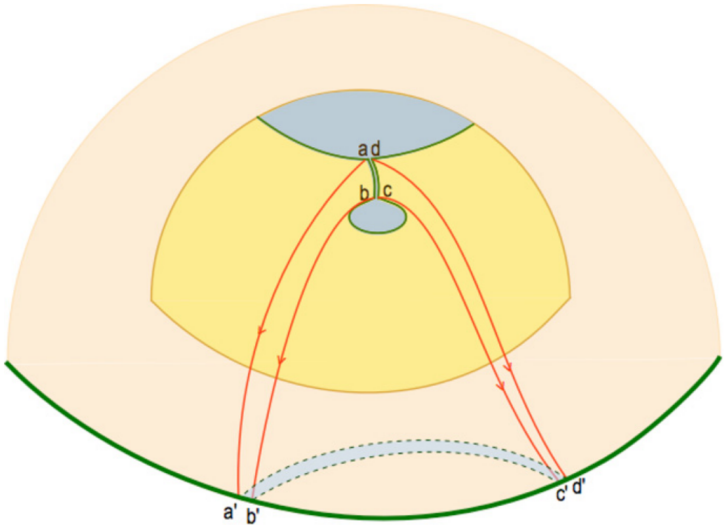

Figure 15: A sketch of the magnetic topology which underlies the s-web idea. The inner yellow area represents the photosphere while the outer area is supposed to be a radial sphere farther out in the heliosphere. Two coronal holes are shown on the photosphere as grey areas, one larger polar coronal hole and a smaller hole located towards the equator. Both are connected by a narrow channel of open flux. The plot was taken from Antiochos et al. (2011).

two coronal holes are shown, a large polar coronal hole and a smaller one which is located closer to the equator. Both holes are connected by a narrow channel filled with open flux. This narrow channel is speculated to be the source for the slow solar wind. The open magnetic field lines originating from this channel ex-

pand outwards into the heliosphere. The grey shaded area encased by dashed lines highlights the magnetic projection of the channel on a spherical surface farther out in the heliosphere, basically at a point where spacecraft based observations of the solar wind take place. This also demonstrates how relatively small regions on the Sun can project onto much larger areas in the heliosphere.
The pure existence of these open flux corridors alone still leaves the same question open as discussed in section 2.3.3.1. The plasma from the closed field line region must be distributed onto the open field lines. According to another study by Antiochos et al. (2007) the open flux corridors are robust features of the magnetic topology. Furthermore their existence is even mandatory as isolated coronal holes cannot exist in their model. Nevertheless the constant evolution of the photosphere, i.e. the random motion of the magnetic foot points, leads to an ongoing shifting and relocation of these corridors. These dynamics dictate permanent opening and closing of adjacent field lines and magnetic reconnection between the open field lines of the corridor and the closed field lines of the loop regions, whereby formerly trapped highly charged plasma can populate the open field lines and escape into the heliosphere.

2.4 IMPLICATIONS FOR THIS WORK

As seen in the previous sections in most scenarios or models the origin of the slow solar wind revolves around the reconnection of magnetic field lines and the subsequent release of formerly trapped highly charged plasma. Therefore, in order to look for the sources of the slow solar wind, one has to probe the borders of open field line regions, because only here the slow solar wind plasma can be distributed on open field lines. The main issue for such a study lies in the fact that there is currently no spacecraft closer than 1 AU to the Sun. Especially the magnetic structure in the corona cannot be directly measured, although it is certainly crucial for the formation of the slow solar wind. A solution would be to employ a model of the coronal magnetic field, which can then be combined with actual in-situ measurements of the solar wind. This is done in the first publication of this work and described in chapter 5. The magnetic field model is described in section 3.3. The instruments and spacecraft which measured the in-situ data are presented in chapter 4.
A spacecraft for a close up investigation of the Sun and the corona is already planned and scheduled to launch in 2019. This will be the Solar Orbiter mission which will closely approach the Sun and study the solar wind with in-situ particle detectors as well as the corona with remote-sensing instruments. Thereby Solar Orbiter will close the current observational gap between Earth's orbit and the Sun. To maximize the prospects of success a measurement scheme for its remote and in-situ instrumentation is devised in the second publication of this work in chapter 6.
Energetic neutral atoms, which have not been covered so far, are described in chapter 7, together with a facility for the calibration of, amongst others, neutral particle detectors.

3 BACK MAPPING

The term back mapping describes techniques used to determine the solar source positions of solar wind particles which have been measured in-situ somewhere in the heliosphere. To determine these source positions one has to trace the travel path of the particles back trough interplanetary space and the corona. Because of the different physical conditions in both mediums, the travel path of a particle cannot be treated in one step. Instead a case differentiation must be done. The path of the particle is therefore divided into two parts. The first part is the interplanetary medium, here the back mapping is done by the so called ballistic back mapping. The second part of the particles path is inside the corona. Here it has to follow the magnetic field lines. Hence, a model for the shape of the magnetic field lines must be applied in order to further trace the particle to its photospheric origin.
The techniques needed for back mapping of the solar wind and the associated principles are described in the following sections.

3.1 COORDINATE SYSTEMS IN THE HELIOSPHERE

In order to orientate oneself in the heliosphere different coordinate systems are applied.

3.1.1 *The Carrington Coordinate System*

One of the most commonly used coordinate systems when dealing with the back mapping of solar wind data is the Carrington coordinate system. It is named after Richard C. Carrington who invented it for its study of sunspots (Carrington, 1855). It is essentially a heliocentric spherical coordinate system co-rotating with the Sun, as such it is tilted with respect to the ecliptic plane by $\sim 7°$, as is the Suns axis of rotation. The coordinates are $(r|\lambda|\phi)$:

- r: the radial distance to the Sun
- λ: the Carrington or heliographic longitude
- ϕ: the Carrington or heliographic latitude

Note that the denotations Carrington and heliographic are synonymous in this work when used in the context of coordinates. λ runs from 0° to 360° while ϕ ranges from 90° to -90° with $\phi = 0$ being the equator, much like geographic latitude.
Next to being a spatial coordinate system, the name Carrington is also used for a temporal measure, the so called Carrington rotations. As mentioned, Carrington studied sunspots on the Sun. Due to the solar rotation the sunspots seemingly wander across the Suns surface until they disappear, only to reappear on the opposite side of the solar disc after roughly 13.5 days. Carrington began to count the rotations of the Sun, starting on the 9th of November, 1853. Since then solar rotations are counted as Carrington rotations, each rotation lasting $\sim$27.27 days, which is

the synodic rotational period of the Sun.
The point of reference for the Carrington system is always the sub Earth point on the Sun, meaning that the next rotation begins when the sub Earth point is at $\lambda = 360°$. In that context a decimal Carrington rotation is always synonymous with a Carrington longitude, e.g. rotation 2040.5 is equivalent to $\lambda = 180°$ and 2040.25 to $\lambda = 270°$, since the Carrington longitude runs backwards from 360° to 0°.

3.1.2 *RTN Coordinates*

A useful coordinate system when dealing with spacecraft data is the so called radial-tangential normal system, or rtn-system. Here the unit vectors are $(\vec{r}_e|\vec{t}_e|\vec{n}_e)$, with $\vec{r}_e$ pointing along the Sun-spacecraft line, $\vec{t}_e$ is the direction along the cross product of $\vec{r}_e$ and $\vec{\omega}$, with $\vec{\omega}$ being the Suns angular velocity. $\vec{n}_e$ is perpendicular to $\vec{r}_e$ and $\vec{t}_e$ and completes the right-hand system. Oddly, this coordinate system is not defined directly above the Suns axis of rotation, since $\vec{r}_e \times \vec{\omega} = 0$ for $\vec{r}_e \parallel \vec{\omega}$ and the three unit vectors do not form a perpendicular system.
Nevertheless the rtn-system is used to describe spacecraft data, as most spacecraft tend to stay in or near the ecliptic plane. In fact, no spacecraft has ever been directly over the Suns rotational pole. The rtn-systems becomes handy when describing the solar wind velocity or the magnetic field.

3.2 BALLISTIC BACK MAPPING

The travel path of a solar wind particle trough the heliosphere excluding the corona can be traced back by using ballistic mapping. It is assumed that the particles travel like a canon ball radially from the Sun to the observer, hence the name ballistic mapping. The concrete assumptions are the following: The solar wind ions travel with a constant velocity on a strictly radial path:

$$v_r = v_p = const \tag{17}$$
$$v_t = v_n = 0 \tag{18}$$

The validity of these assumptions will be discussed later on. The parameters needed are the measured proton velocity v_p, the spacecraft orbit data, meaning the radial distance to the sun d_{sc}, the heliographic longitude λ_{sc} and latitude ϕ_{sc} and the Suns angular velocity ω. As mentioned above, ballistic mapping cannot be used for the whole travel path of the particle, it can only be used for the part where the particles do not have to follow the magnetic field lines. As such it is not possible to obtain the photospheric source coordinates. What is instead determined is the so called ballistic foot point λ_{bfp} and ϕ_{bfp} of the spacecraft on the source surface:

$$\lambda_{bfp}(v_p, d_{sc}) = \lambda_{sc} + \omega \frac{(d_{sc} - 2.5R_\odot)}{v_p} \tag{19}$$
$$\phi_{bfp} = \phi_{sc}. \tag{20}$$

As can be seen in equation 19, the ions are traced back to a point $1.5\,\mathrm{R}_\odot$ above the photosphere. This point marks the so called source surface, which will be explained in section 3.3. For now it is just the boundary between the mentioned case differentiation. By trying to use ballistic back mapping further down into the

corona the necessary assumptions of equations 17 and 18 would be heavily violated.
One has to keep in mind that the assumptions made are not always fulfilled even in the interplanetary medium. Regarding the strictly radial propagation of the particles, equation 18 is not true in general. However, $\frac{v_r}{v_p} \approx 1$ holds for the majority of time. Nonetheless, studies by Marsch et al. (1982) have shown that the proton velocity distribution is not so trivial as equation 18 requires. Additionally, Berger et al. (2010) have shown that the velocity distributions of heavy ions do not follow that of the solar wind protons. Also care must be taken with equation 17. Dynamic regions in the solar wind as described in section 2.1.4 experience significant changes of v_p on their way to the spacecraft. Most prominent examples are compression regions, where the fast solar wind runs into the slow solar wind and is thereby decelerated.
Nonetheless, if dynamic regions are excluded from the analysis, equations 17 and 18 are reasonable assumptions in general and ballistic back mapping is a viable approach for estimating the source regions of the solar wind on the source surface.

3.3 MAGNETIC MAPPING AND THE PFSS MODEL

Inside the corona ballistic back mapping is no longer a valid approach. Below the Alfvénic point the solar wind plasma follows the curvature of the magnetic field lines and is therefore not strictly radially propagating. Also it is still being accelerated, hence equation 17 is not true. In order to trace the path of the solar wind ions through the corona, the coronal magnetic field has to be known. By now there are no direct measurements of the coronal magnetic field, therefore its precise structure is unknown. However, the field can be simulated with suitable models, like the so called Potential Field Source Surface (PFSS) model.
The PFSS model was developed parallel by Altschuler and Newkirk (1969) and Schatten et al. (1969). The model starts with the assumption of a current free corona, which is reasonable below a certain distance above the Sun typically below $2.6\,R_\odot$ (Altschuler and Newkirk, 1969). The absence of electric currents means

$$\vec{\nabla} \times \vec{B} = 0 \tag{21}$$

and thus

$$\vec{B} = -\vec{\nabla}\psi. \tag{22}$$

Following equation 22 the magnetic field can be described as the gradient of a scalar potential ψ. The divergence of $\vec{B}$ always vanishes, therefore:

$$\vec{\nabla}\vec{B} = -\vec{\nabla}\vec{\nabla}\psi \tag{23}$$

$$0 = \Delta\psi. \tag{24}$$

Equation 24 is Laplace's equation, its solution is given by

$$\psi(r,\theta,\phi) = R_\odot \sum_{n=1}^{\infty}\sum_{m=0}^{n}\left[\left(\frac{R_\odot}{r}\right)^{n+1}\left(g_n^m \cos(m\phi) + h_n^m \sin(m\phi) P_n^m(\theta)\right)\right], \tag{25}$$

with g_n^m and h_n^m being constants and $P_n^m(\theta)$ are the associated Legendre Polynomials. Please note that $(r|\theta|\phi)$ are classic spherical coordinates and not Carrington

coordinates. With equation 25 the components of the magnetic field can be written down as

$$B_r = R_\odot \sum_{n=1}^{\infty} \sum_{m=0}^{n} \left[(n+1) \left(\frac{R_\odot}{r} \right)^{n+2} (g_n^m \cos(m\phi) + h_n^m \sin(m\phi) P_n^m(\theta)) \right] \tag{26}$$

$$B_\theta = - \sum_{n=1}^{\infty} \sum_{m=0}^{n} \left[\left(\frac{R_\odot}{r} \right)^{n+2} (g_n^m \cos(m\phi) + h_n^m \sin(m\phi) \frac{dP_n^m(\theta)}{d\theta}) \right] \tag{27}$$

$$B_\phi = \frac{-1}{\sin\theta} \sum_{n=1}^{\infty} \sum_{m=0}^{n} \left[\left(m \frac{R_\odot}{r} \right)^{n+2} (g_n^m \sin(m\phi) - h_n^m \cos(m\phi) P_n^m(\theta)) \right], \tag{28}$$

with $r \geq R_\odot$. The problem now are the constants g_n^m and h_n^m, these must be somehow obtained before $\vec{B}$ can be calculated. One parameter that can be measured is the photospheric line of sight magnetic field B_l. The relation between B_l and the components B_r, B_θ and B_ϕ is

$$B_l = B_r \cos(\theta_0 - \theta) \cos(\phi - \phi_0) + B_\theta \sin(\theta_0 - \theta) \cos(\phi - \phi_0) - B_\phi \sin(\phi - \phi_0), \tag{29}$$

with θ_0 and ϕ_0 being the coordinates of the observers foot point. With the help of equations 27 and 28 this can be written as

$$B_l = \sum_{n=1}^{\infty} \sum_{m=0}^{\infty} (g_n^m \alpha_{nm}(\theta, \phi) + h_n^m \beta_{nm}(\theta, \phi)) \,. \tag{30}$$

Here $\alpha_{nm}(\theta, \phi)$ and $\beta_{nm}(\theta, \phi)$ are just variables to shorten the lengthy term. Equation 30 can now be used to find g_n^m and h_n^m by using them as fit parameters when fitting equation 30 to the measured line of sight magnetic field.
Hypothetically, solutions for the coronal magnetic field could now be calculated based on the measured photospheric field. Unfortunately, nature is again more complicated. The above discussed does not factor in the solar wind, which influences and distorts the magnetic field from a certain height above the photosphere on. More precisely, the assumption of equation 21 no longer holds above this point. This can be circumvented by introducing an outer boundary to the calculation, which forces the magnetic field into a purely radial configuration. Thus, the influence of the solar wind is taken into account, as this is what it effectively does when it reaches the point where the kinetic pressure of the plasma exceeds the magnetic pressure. For the computation this can be achieved by setting $\psi = 0$ at this outer boundary. This zero-potential surface is usually set to be at $r = 2.5\,R_\odot$, as this fits best with observations made by coronal imaging. Here closed field line loops could be observed for heights up to $\sim 2\,R_\odot$. The introduction of the zero-potential surface, which is also more commonly called source surface, means that no closed field lines can occur above it. Only beneath the source surface a mixture of open and closed field lines can be found.
The above described closely followed the work of Altschuler and Newkirk (1969), Schatten et al. (1969) utilized a different approach using Green's functions.
The PFSS data used in this work has been modeled by Kruse (2018). All plots and methods presented in the next section have been created as part of this work.

3.4 ANALYZING THE FIELD LINE GEOMETRY

The PFSS model as outlined above or in Kruse (2018) creates a map of the field lines geometry in the corona. Technically, the model provides the magnetic field strength

and direction at any point between photosphere and corona. Typically, the field looks like the example depicted in figure 16. It can be seen that the open field lines

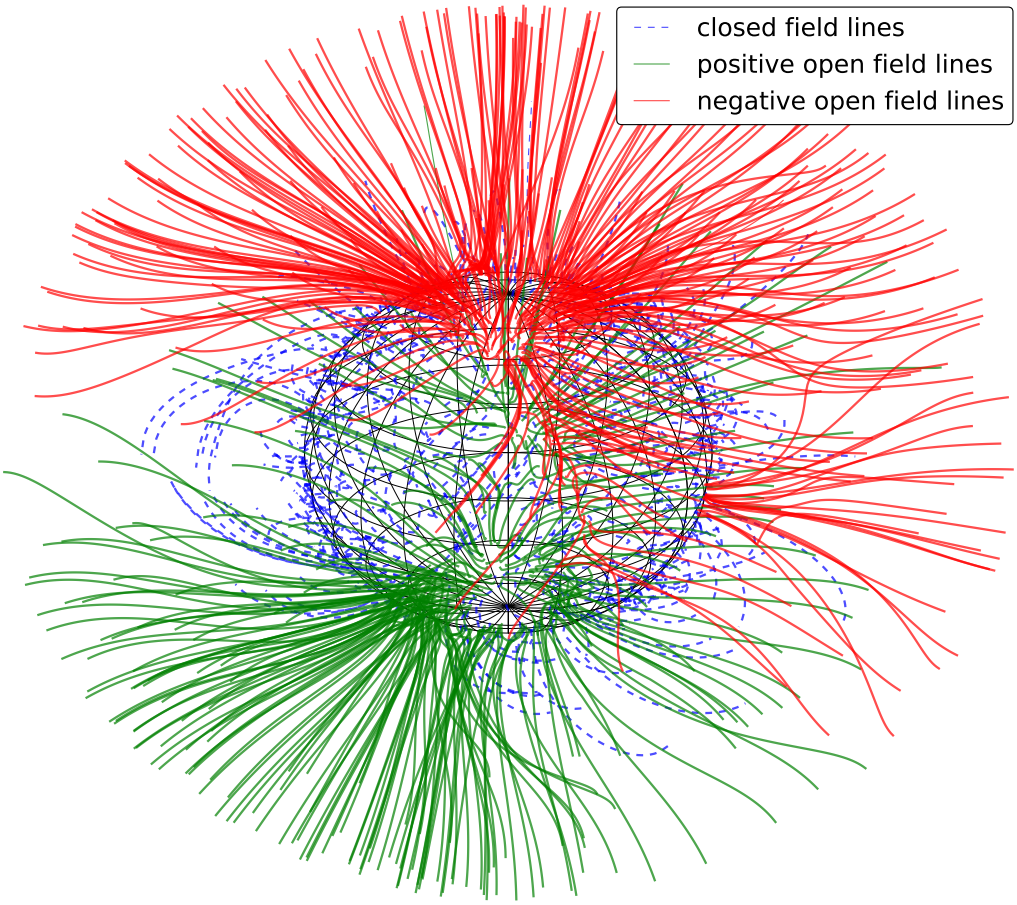

Figure 16: An Example of the output of the PFSS model. Shown is the computed magnetic configuration in the corona during Carrington rotation 2056. The red and green lines show open magnetic field lines of negative and positive polarity. The dashed blue lines show closed field lines. The black grid depicts the photosphere. For better visibility only 1/10th of the open field lines and only 1/100th of the closed field lines are drawn. In total the model produces 64800 field lines.

are divided into two polarities, roughly dividing the Sun into two hemispheres. This is of course expected, given the fact that the Sun resembles a magnetic dipole during its quiet times. Between both regimes of inward and outward pointing open field lines lies a region of closed field lines forming arch like structures. This overall shape of the magnetic field is consistent with solar observations like the one shown in figure 13. The way the field lines are shown in figure 16 mainly serves as a visualization of the magnetic field. A more practical way to work with these field lines maps is to project the field lines onto longitude-latitude projections for individual height levels. This is shown in figure 17. In this depiction it can be nicely seen how the open field line regions transform with increasing height. Starting from isolated isles surrounded by closed field lines on the photosphere they fan out while ascending towards the source surface. Once they reached $2.5\,R_\odot$ the whole space is filled with open field lines.

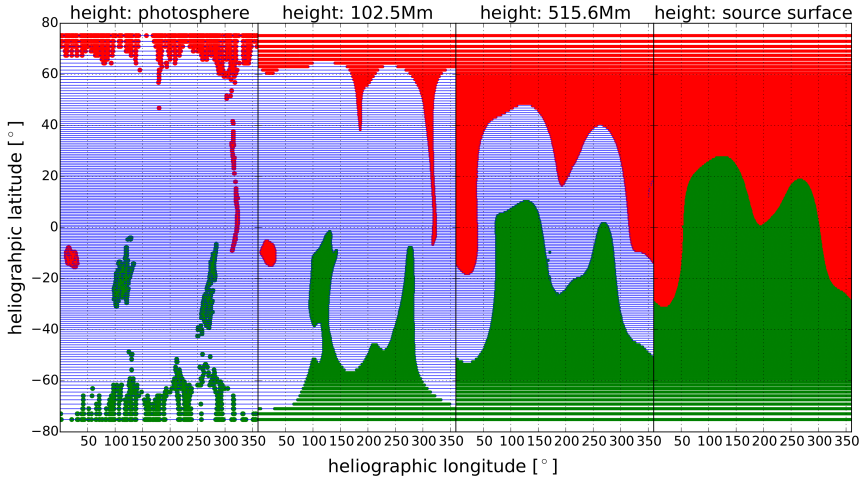

Figure 17: The magnetic field lines produced by the PFSS model for Carrington rotation 2056 shown in a longitude-latitude projection. This shows the same configuration as in figure 16. The four panels depict four different height levels, beginning on the photosphere in the left panel and ending at the source surface in the right panel. The stated height for the middle panels is relative to the photosphere.

With the PFSS maps being available in the format as shown in figure 16 and 17 they can now be combined with in-situ data which has been ballistically back mapped as described in section 3.2. Each of the ballistic foot points λ_{bfp} and ϕ_{bfp} of the in-situ data on the source surface is related to the nearest respective open field line by using a KD-Tree algorithm (Bentley, 1975). These open field lines are then referred to as source field lines, since it is then assumed that the solar wind had to travel along these lines while traversing the corona. In figure 18 the identified source field lines and their course through the corona is shown. Here the original ballistic

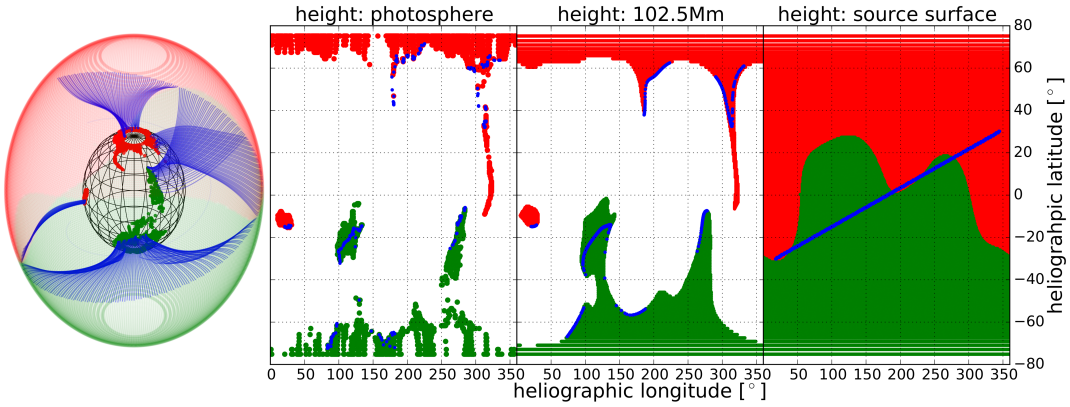

Figure 18: The same magnetic configuration as shown in figure 16 and 17, but with the closed field lines being omitted. Here the blue points depict identified source field lines, which are traced down from the source surface to the photosphere. The three panels to the right show the field lines in a longitude-latitude projection. The left panel shows the same configuration, but with the source field lines drawn over all height levels while the rest of the open field lines are only plotted for the source surface and the photosphere.

foot points range from -30° $\leq \phi_{bfp} \leq$30° and 10° $\leq \lambda_{bfp} \leq$350°. The blue lines

in the left panel in figure 18 show the identified source field lines and how these traverse the corona. Following this procedure one can identify the photospheric source regions of the solar wind. In addition to that, since the magnetic field lines are sampled over several different height levels between photosphere and source surface, even the position inside of the corona can be investigated. Thereby, the bending of the source field lines can be taken into account.
For the first publication of this work (see chapter 5) the distance of identified source field lines to the border of open field line regions has been calculated. In order to do so, the border had to be determined in the first place. Two methods were applied to achieve that. For the first method the outermost open field lines are defined as coronal hole border, as shown in figure 19. Here the open field lines

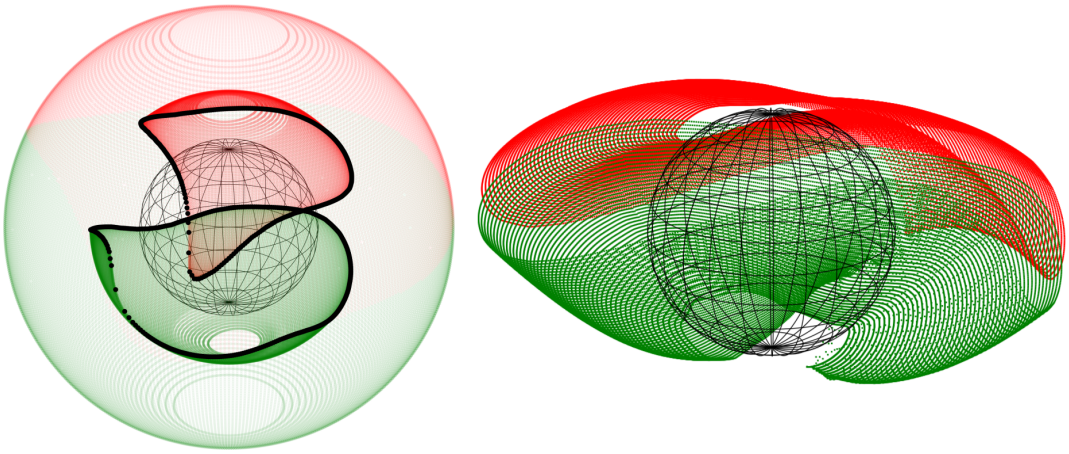

Figure 19: Plot that shows in the left panel the open field lines on the source surface and on an intermediate height level above the photosphere. The black points mark the open field lines that have been identified as coronal hole border. In the right panel the black points are interpolated over all height levels to form a surface that represents the border of the coronal holes.

that have been identified as coronal hole border are shown as black dots. This is done for every height level. The black dots are then interpolated between the different height levels to from a continuous point cloud, as shown in the right panel of figure 19. The distance to the coronal hole border is then for each source field line on each height level defined as the distance to the closest point of the point cloud which defines the coronal hole border. Therefore, if there are N height levels between source surface and photosphere there are N distances to the border determined for each source field line. That way it can be determined if a source field lines bends away from the border of the coronal hole or if it stays close to the border while ascending from the photosphere to the source surface.
The other way to calculate the distance to the border is to create a point cloud from the closed field lines which are also modeled by the PFSS model. Hereby no artificial coronal hole border needs to be defined. A sketch is drawn in figure 20 to visualize both determinations of the distance to the coronal hole border.

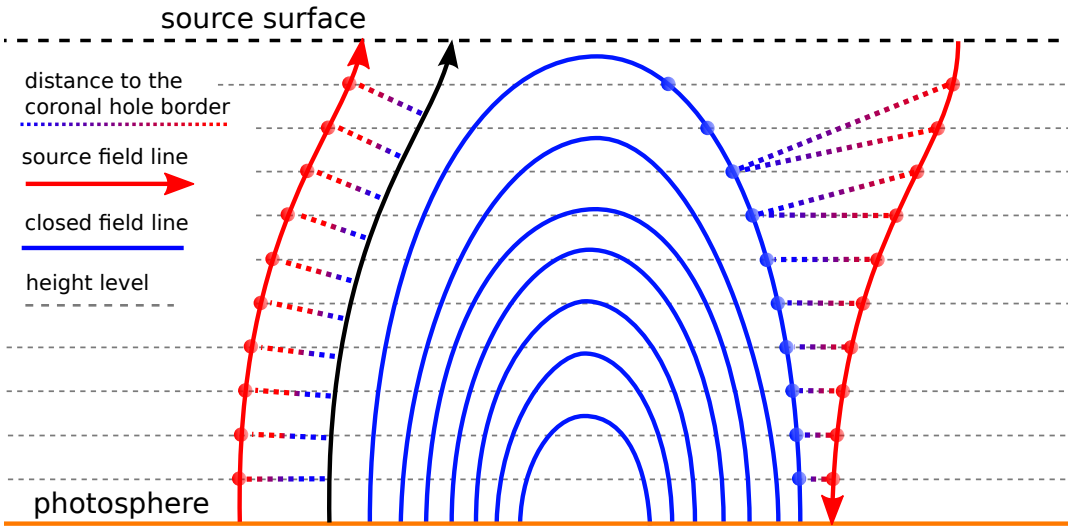

Figure 20: Sketch to illustrate the determination of the distance to the coronal hole border for individual source field lines. Shown is the region between photosphere and source surface. The blue lines represent the closed-loop regions which are surrounded by open field lines. The red lines are source field lines. The black lines is an open field line that has been identified as coronal hole border, compare with figure 19. The red points and blue points are the discrete data points produced by the PFSS model. The dotted lines depict the way the closest distance to the border has been calculated. For the left source field line the distance is determined to the outermost open field line, which then acts as coronal hole border. For the right source field lines the distance is determined directly to the nearest closed field line.

4 SPACECRAFT AND INSTRUMENTS

4.1 THE ULYSSES SPACECRAFT

The Ulysses spacecraft (Marsden and Smith, 1996) was launched in the year 1990 and operated for nearly 20 years until its radioisotope thermoelectric generator shut down in 2009. One of its most remarkable feature was its highly inclined orbit which let reach a heliographic latitude of 80.22°, see Marsden et al. (1996), thus enabling observations of the solar wind over the poles of the Sun. The only comparable mission in this regard was Helios (Leinert et al., 1974), but with a much smaller inclination. The orbit of Ulysses is shown in figure 21. Its closest distance

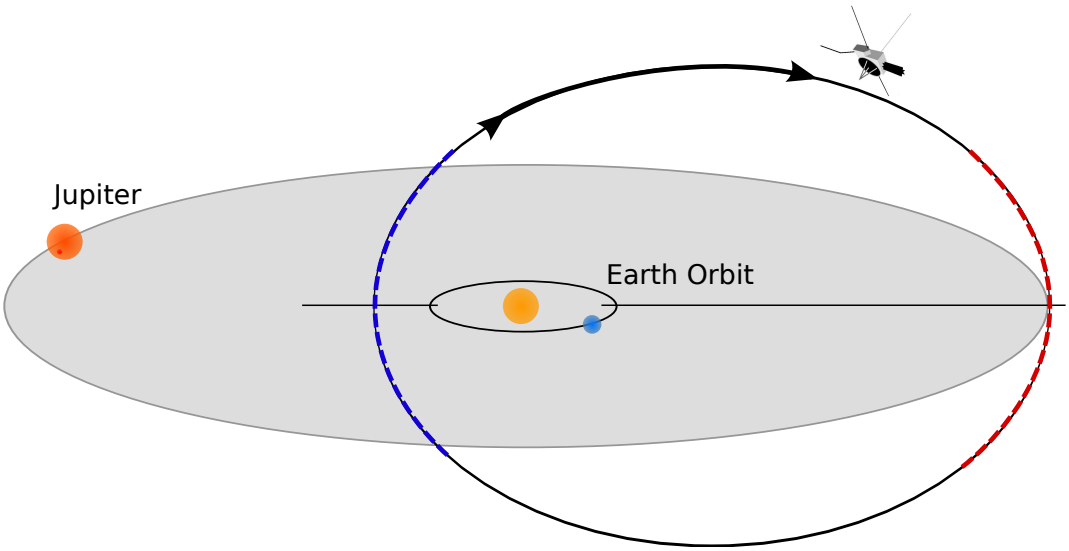

Figure 21: A schematic representation of Ulysses' orbit with respect to the ecliptic plane and the planets Earth and Jupiter. The blue part shows the fast latitude scan and the red part the slow latitude scan. Plot after European Space Agency (2008).

to the Sun is 1.33 AU on the so called fast latitude scan, shown in blue in figure 21, which refers to the fact that Ulysses is relatively fast on this part of its orbit. The furthermost distance is 5.4 AU on the slow latitude scan, shown in red in figure 21. Ulysses carried a wide range of scientific instruments from which three were used in this work:

- The Solar Wind Plasma Experiment, see Bame et al. (1992): The Solar Wind Plasma Experiment, also abbreviated SWOOPS (Solar Wind Observations Over the Poles of the Sun) is used to measure protons and electrons from which several plasma parameters are derived.
- The Solar Wind Ion Composition Spectrometer (SWICS), see Gloeckler et al. (1992): SWICS can measure the heavy ions in the solar wind up to and even beyond iron ions. It thereby complements the SWOOPS measurements and determines the ionic composition.

- The Vector Helium Magnetometer (VHM), see Balogh et al. (1992): VHM is used to measure the components of the magnetic field in three dimensions.

The data from SWOOPS and VHM are not evaluated from scratch in this work. Instead, already available data products were used, taken from the Ulysses Final Archive, (Ulysses Final Archive, 2008). In table 4 the used data products for all instruments are listed. In the case of SWICS, the data is extracted from the raw Pulse Height Analysis (PHA) data. Hence, SWICS will be described in more detail. Since SWOOPS shares some of the measurement principle with SWICS it will be briefly described in the next section. For more information about VHM see Balogh et al. (1992).
At the end of this chapter the SWICS-data analysis will be illustrated.

4.1.1 *Solar Wind Plasma Experiment*

SWOOPS consist of two particle detectors, one for the detection of electrons and the other for the detection of ions, see Bame et al. (1992) for the instrument paper. In this work primarily the ion measurements are used. Both detectors share the same measurement principle. A curved-plate electrostatic analyzer behind the entrance permits only particles with a certain kinetic-energy per charge ratio E/q into the instrument. The voltage applied to the analyzer is then varied in order to obtain measurements of different E/q ratios. The main information used from SWOOPS are basic solar wind plasma data, i.e. the solar wind velocity, density and temperature, which can all be inferred from the proton measurements. The fact that the instrument only measures the E/q ratio means that only protons and alpha particles can be reliably discriminated from the data set. Heavier ions cannot not be isolated from the observations. For that a more complex instrument is needed.

4.1.2 *The Solar Wind Ion Composition Spectrometer*

The Solar Wind Ion Composition Spectrometer (SWICS) is a Time of Flight (ToF) mass spectrometer, see Gloeckler et al. (1992). It has an entrance system comparable to SWOOPS which measures the E/q ratio of detected ions. But in contrast to that it additionally measures the ToF t_{ToF} of an ion as well as the residual kinetic energy E_{res}. With this additional information it is possible to determine mass m, charge state q and kinetic energy E of an incident ion.
Behind the electrostatic analyzer the ion is post accelerated by a known voltage U and passes through a thin carbon foil. The secondary electrons from the foil trigger the start signal for the ToF measurement. The accelerated ion then flies along a known distance d and hits a solid state detector, thereby again emitting secondary electrons which trigger the stop signal. The front of the solid state detector has a dead layer which the ion has to traverse before its residual energy E_{res} is measured. In such a way the ions attributes can be determined:

$$m = \frac{2E_{pa}}{v^2} = \frac{2E_{pa}t_{ToF}^2}{d^2} \tag{31}$$

$$q = \frac{E_{pa}}{U + E/q} \tag{32}$$

$$E = \frac{E}{q}q \tag{33}$$

Here E_{pa} is the kinetic energy of the ion after the post acceleration. Unfortunately due to unpreventable measurement uncertainties it is not possible to use the equations 31 to 33 to determine a measured ions characteristics in reality because $E_{pa} \neq E_{res}$. The ion looses an unknown amount of energy while passing through the foil and when traversing the dead layer of the solid state detector. Nevertheless for each fixed E/q step each ion of the solar wind occupies a specific coordinate in an E_{res}xt_{ToF} matrix, or et-matrix. Figure 22 gives an example for an et-matrix

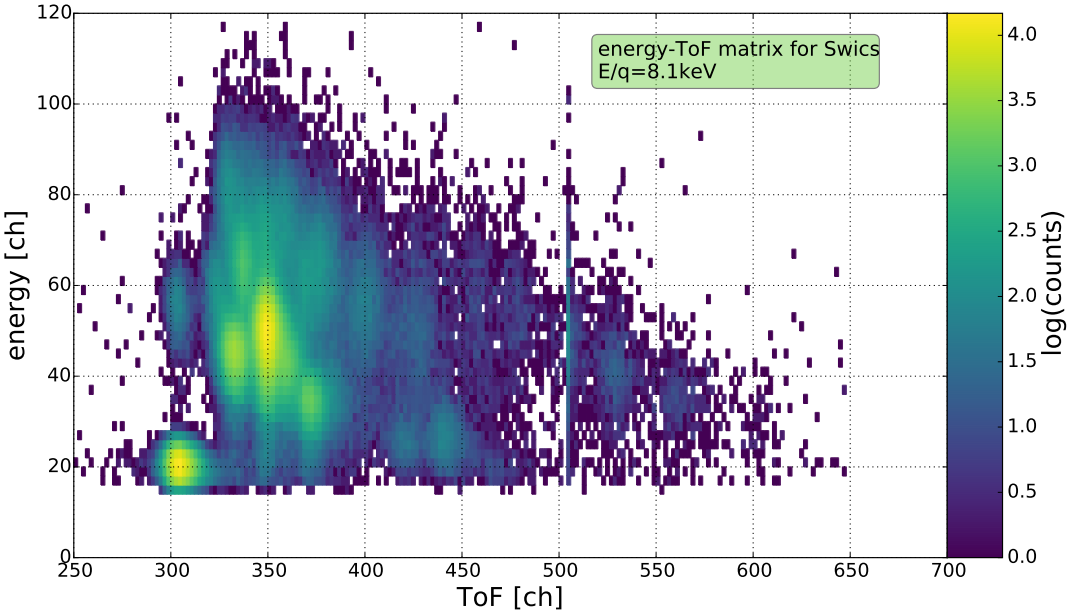

Figure 22: An example for a SWICS energy-ToF matrix. The x axis gives the time of flight in channel numbers, the y axis gives the residual energy in channel numbers. The counts are shown as color map in a logarithmic scaling. The energy per charge for that measurement is 8.1 keV. The total number of counts in this plot is $6 \cdot 10^5$ and have been accumulated over 365 days from the 1st of January to the 31st of December in 1995.

from SWICS for one particular E/q ratio in form of a 2D histogram where the ToF is given on the x axis and the energy measured in the solid-state detector on the y axis in units of channels. The number of counts is shown by the color map in a logarithmic scaling. It contains counts measured over the course of a whole year. Different ion species occupy specific positions in the 2D matrix which depend on the E/q ratio. As mentioned above, due to energy losses their position is displaced and the counts are distributed around their shifted position. The count distribution for each ion can be approximated by a 2D Gaussian distribution.

4.2 THE ADVANCED COMPOSITION EXPLORER

The Advanced Composition Explorer (ACE) was launched on 25th of August in 1997 and is still in service. It is located at the Lagrangian point 1 (L1). L1 lies on the radial between Earth and the Sun and is roughly $1.5 \cdot 10^6$ km away from Earth. Due to the superposition of the Sun's and Earth's gravitational field an object at L1 has the same orbital period as Earth, meaning that ACE and Earth are co-rotating

around the Sun. In comparison to Ulysses the orbit of ACE is much simpler. The radial distance to the Sun stays constant and the heliographic latitude only varies between -7° $\geq \phi_{sc} \leq$ 7°, which corresponds to the inclination of the Suns axis of rotation with regard to the ecliptic plane. This work utilizes three instruments out of ACEs instrumentation:

- The Solar Wind Ion Composition Spectrometer (SWICS), see Gloeckler et al. (1998): This instrument is identical in construction to SWICS on Ulysses, in fact it is the flight spare that was used for the ACE mission which started some years after Ulysses. The data analysis for ACE/SWICS has been done by Berger (2008).
- The Solar Wind Electron Proton Alpha Monitor (SWEPAM), see McComas et al. (1998a): SWEPAM on ACE basically serves the same purpose as SWOOPS on Ulysses. Again, SWEPAM is regarded as a black box.
- The Magnetometer Instrument (MAG), see Smith et al. (1998): The MAG instrument serves the same purpose as VHM on Ulysses. Like VHM, MAG is regarded as a black box.

So both Ulysses and ACE provide similar data sets for the analysis done in this work. The SWEPAM and MAG data were taken from The Ace Science Center (2008). For a summary of the used data products see table 4.

instrument	data product
SWICS	O^{7+}/O^{6+}, C^{6+}/C^{5+}
SWOOPS/SWEPAM	v_p, n_p, T_p
VHM/MAG	B_r, B_t, B_n

Table 4: The different instruments and the respective data products which were used in this work.

4.3 SWICS DATA EXTRACTION

As hinted in section 4.1.2 the data provided by Ulysses/SWICS cannot be directly used because measured ions are not automatically identified by the instrument. As shown in figure 22 the measured ions occupy distinct positions in an energy-ToF matrix. In principle they are determined by that, as each ion has an individual and unique (E, ToF) coordinate. The problem is that these coordinates are not known ab initio, they could be calculated by equations 31 and 32, but due to different energy losses during the measurement process their (E, ToF) positions are shifted. Even worse, because the energy losses are of a statistical nature, the ions positions are also smeared out. That leads to a distinct overlapping of different ion signals. Therefore, in order to extract the ion data from the energy-ToF matrix, first the ion positions must be determined and second the counts for each ion must be read out while considering the overlap of the different ion species.
Each measurement cycle consist of 64 nonlinear E/q steps. For each E/q step the ion positions are different since the ions energies differ. Fortunately, the determination of the ion positions has already been done for ACE/SWICS, see Koeten (2009)

for more information. In principle, since Ulysses/SWICS and ACE/SWICS are identical in construction, the ion positions can be used for Ulysses/SWICS. In reality there are two adjustments that must be made before the ion positions can be transferred.
The first adjustment must be made because ACE/SWICS and Ulysses/SWICS have different post acceleration voltages. As stated in section 4.1.2 the ions are accelerated after they passed trough the electrostatic analyzer in order to have enough energy to penetrate a thin carbon foil, which inevitably leads to an additional unknown energy loss. Unfortunately, regarding the post acceleration voltage U, it is $U_{ACE} \neq U_{Ulysses}$, which consequently leads to an offset between the ACE and the Ulysses data set in ToF and energy. The offsets Δt_{ToF} and ΔE_{tot} can be determined. For t_{ToF} it is:

$$t_{ToF} = \frac{d}{v_{ion}} = d\sqrt{\frac{m}{2q(E/q + U)}}, \tag{34}$$

with d being the distance over which ToF is measured and v_{ion} being the ion velocity after the post acceleration. The wanted Δt_{ToF} then is:

$$\Delta t_{ToF} = d\sqrt{\frac{m}{2q}}\left(\sqrt{\frac{1}{E/q + U_{Ulysses}}} - \sqrt{\frac{1}{E/q + U_{ACE}}}\right). \tag{35}$$

Using equation 35 the ToF position for each ion can be transferred from ACE/SWICS to Ulysses/SWICS. Technically it is not correct to use equation 35 because, like equations 31 and 32, it is only valid for a non error-prone instrument. However, under the assumption that both instruments are really identical in construction it can be assumed that the deviation Δ_{ToF} is most likely correct, as any altering effects affect both instruments equally. Δ_{ToF} is most likely energy dependent, but the post acceleration voltages in both instruments are rather similar:

- $U_{ACE} = 24.868\,\text{keV}$
- $U_{Ulysses} = 22.9\,\text{keV}$

Based on that it can be assumed that equation 35 is sufficiently valid. The same shift must be done for the energy position

$$E_{tot} = q\left(\frac{E}{q} + U\right) \tag{36}$$

$$\Rightarrow \Delta E_{tot} = q(U_{Ulysses} - U_{ACE}). \tag{37}$$

The second adjustment must be made because ACE/SWICS and Ulysses/SWICS do not have the same range of E/q steps. In figure 23 the E/q channels for both instruments are shown, it can be seen that the ranges slightly differ and the one for ACE has a discontinuity. This poses no problem since the range for Ulysses lies completely inside the range for ACE. In fact, the last 47 E/q channels (the points on the right in figure 23) are identical for both instruments. The energy and ToF positions of each ion for the cases were the E/q steps are not identical can be determined by interpolation. This is exemplarily shown in figure 24. Here the ToF and energy channel positions for O^{6+} are shown for ACE/SWICS (as determined in Koeten (2009)) as solid line and the interpolated points for Ulysses/SWICS. This is

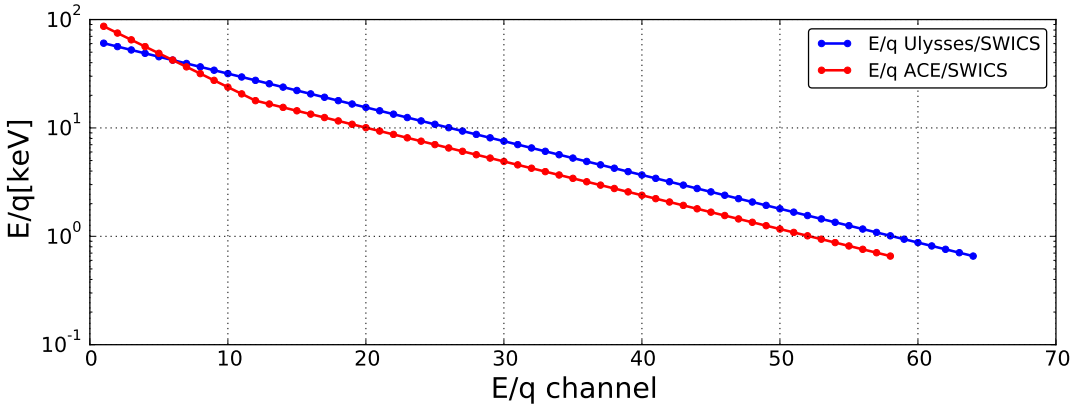

Figure 23: E/q values logarithmically plotted as function of the channel number for ACE (red) and Ulysses/SWICS (blue).

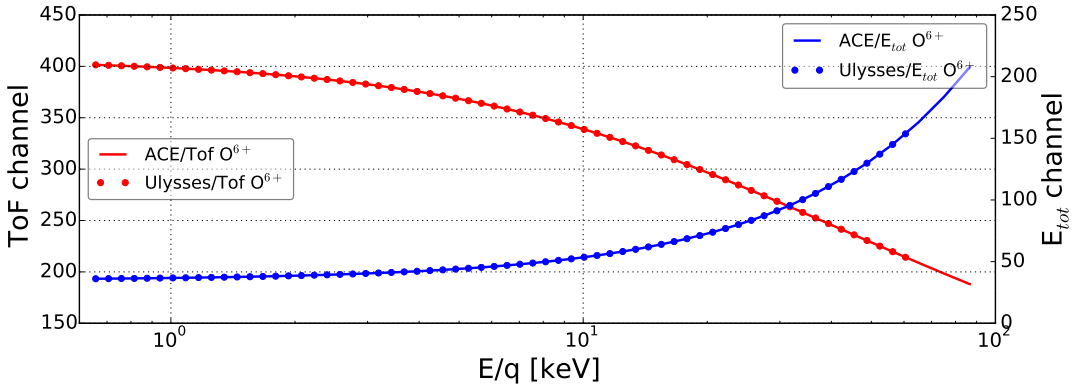

Figure 24: Energy and ToF channel for O^{6+} as function of E/q. The solid lines give the values for ACE/SWICS while the dot markers are the interpolated values for Ulysses/SWICS. Please note that the values for ACE/SWICS are also discrete, but for the sake of visibility solid lines were chosen.

done for all ion species which are expected to be measured. The interpolation is not done with a conventional fit, but with a numerical spline fit. The determined et-positions for the ions used in this work, O^{6+}, O^{7+}, C^{5+} and C^{6+} are listed in appendix 11.
With the above described adjustments done the ion positions in the $E_{res} \times t_{toF}$ matrix can be carried over to Ulysses/SWICS. If applied to the et-matrix shown in figure 22 the different peaks can now be identified and assigned to the respective ion species. This is shown in figure 25. It can be seen that the transfer of the ACE/SWICS ion positions works reasonably well. Now that the ions positions are identified the count rates must be extracted from the et-matrices. This can be done by the so called box rate method. Thereby, for each ion species rectangular boxes are centered around the respective position in the et-matrix and the counts inside the box are determined. The problem of the overlapping ion peaks remains. The size of the boxes must be chosen so that two factors are considered:

1 If the box is too small, the number of counts inside is at the risk of becoming too small.

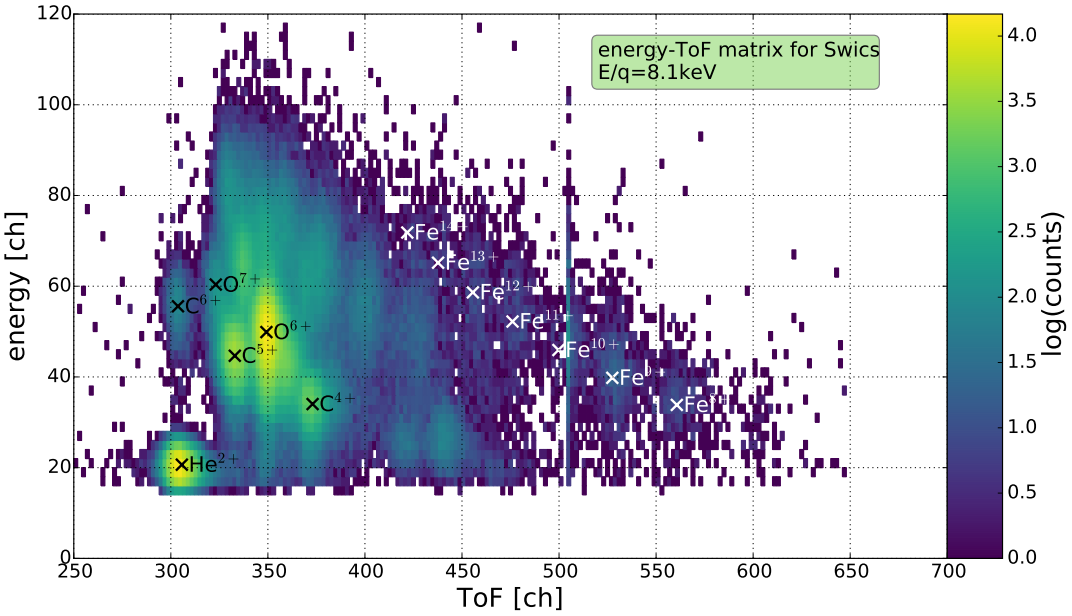

Figure 25: The same et-matrix as shown in figure 22. Here some of the ion positions are identified, namely He^{2+}, C^{4+}, C^{5+}, C^{6+}, O^{6+}, O^{7+} and Fe^{8+} to Fe^{14+}.

2 If the box is too large, the number of counts that are not related to the respective ion becomes to large, falsifying the count rate determination.

In this work primarily oxygen and carbon ions are used. Besides hydrogen and helium, oxygen and carbon belong to the most abundant elements inside the solar wind , as seen in table 1. Therefore point number one of the above numeration is not a great concern. Point number two is of greater importance for this analysis, since the so called spillover of adjacent ions can ruin the count rate determination. Hence, the boxes are chosen small. A good measure for box sizes are the respective sigmas. The ion peaks in the et-matrix can be approximated by 2d Gaussian distributions. Accordingly, each ion has a pair σ_{ToF} and σ_E. The values for σ_{ToF} and σ_E are taken from Koeten (2009) as well. Now the sizes for the boxes can be given in units of these sigmas. For this work one-sigma boxes were chosen. Their application can be seen in figure 26. Here the identified ions are boxed with one-σ boxes. It can be seen that there is an overlap between some of the iron boxes, meaning that some counts in this et-matrix are counted twice for two different ion species. Hence the resulting Fe^{14+} and Fe^{13+} count rates are erroneous by default. The last step to do is to correct the obtained count rates for their respective base rate weighting and their detection efficiency. The base rates adjust the count statistics for the fact that not all detected counts contribute to the PHA data, due to telemetry limitations. The base rates for Ulysses/SWICS are known and the detector efficiency is again inherited from ACE/SWICS.

It is important to note that the above described method cannot reproduce the absolute count rates for each ion species, because by using one-σ boxes around a 2D Gaussian distribution only approximately $68\% \times 68\% = 46\%$ of all counts are taken into consideration. But since one-σ boxes are used for every ion species it is possible to reliably derive relative values like count rate ratios, which are exclusively used in this work.

In order to verify this method the count rate ratios derived can now be compared

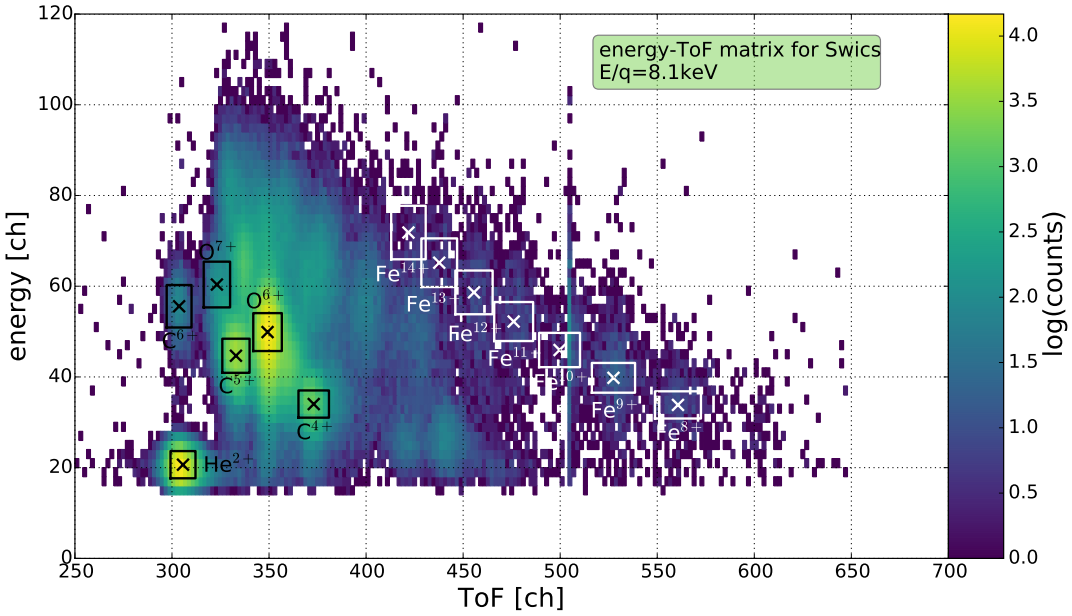

Figure 26: The same et-matrix as shown in figure 22. Here the formerly identified ion positions He^{2+}, C^{4+}, C^{5+}, C^{6+}, O^{6+}, O^{7+} and Fe^{8+} to Fe^{14+} are boxed with one-σ boxes.

to the ratios derived elsewhere by Zurbuchen and von Steiger (2000). The comparison is shown in figure 27 together with the data from this work. Here the red

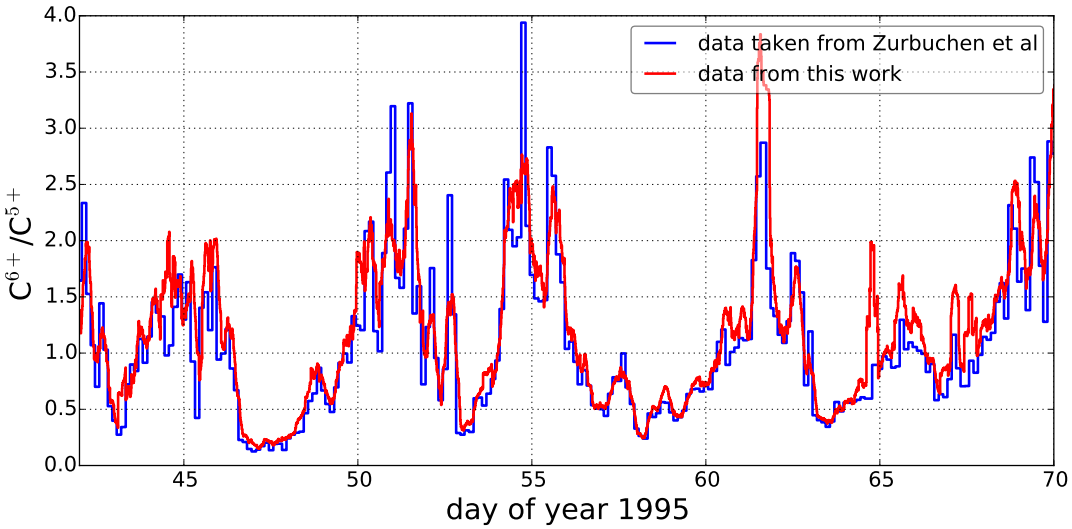

Figure 27: Comparison of publicly available Ulysses/SWICS data with the box rate derived data. Shown is the count rate ratio for C^{6+} to C^{5+}, the blue curve shows the data from Zurbuchen and von Steiger (2000) and the red curve data derived in this work. Note that both data sets have different time resolutions with a factor of 13 between both data sets.

curve is the data derived by the method described above while the blue curve represents the data taken from Zurbuchen and von Steiger (2000). It can be seen that both curves follow the same behavior with some minor discrepancies. It should be

noted that the time resolution for the red curve is higher than for the blue curve. For the box rate method the highest time resolution possible was used, meaning that each instrument cycle was analyzed. One instrument cycle lasts 13 minutes. The external data has a time resolution of 3.5 hours or 13 instrument cycles. A running average has been applied to the red curve to increase the comparability between both data sets. Nevertheless, brief mismatches between both curves, especially short lasting spikes in the C^{6+}/C^{5+} ratio can be attributed to the different time resolution.

It has to be noted that there are more sophisticated methods to extract the ion count rates from the SWICS et-matrices. The method conducted here is sufficient for ion species with high count rates such as oxygen and carbon. For other ions a more complex box-rate analysis is described in the appendix of von Steiger et al. (2000), which was used to derive the C^{6+}/C^{5+} ratio shown in figure 27. As stated above, for the abundant carbon and oxygen ions considered in this work the presented method proves to be equally applicable. Furthermore, the higher time resolution is advantageous since a smaller volume of the solar wind can be sampled. By using a lower time resolution the instrument is effectively averaging different structures in the solar wind like CIRs.

Probably the most sophisticated method to analyze SWICS data is a fit algorithm where the whole et-matrix is fitted with a sum of many 2D Gaussian, one for each ion species. This has been done by Berger (2008).

5 INVESTIGATION OF SOLAR WIND SOURCE REGIONS

In this chapter the first publication of this work is covered. Here the described back mapping techniques in combination with the PFSS model are used in order to relate in-situ measurements of the solar wind with magnetic structures in the corona.

5.1 MOTIVATION

The goal of this publication is to probe the border of coronal holes for the sources of the slow solar wind. As described in section 2.3 several of the ideas about the sources and release mechanisms of the slow solar wind revolve around magnetic reconnection between open and closed magnetic field lines. Naturally, this can only happen in the vicinity of the closed field line regions. Therefore one should expect a correlation between the solar wind parameters that define the solar wind type and the proximity to the closed field line regions.
The in-situ data used for this study are taken from Ulysses during its slow latitude scan in 1996/97. During that time, Ulysses was far out in the solar system, in the vicinity of Jupiter's orbit. Normally this is not an ideal case for a back mapping study, due to the errors that afflict the ballistic back mapping. This peculiar part of Ulysses orbit is initially chosen for two reasons. The first reason is that it took place during the quiet phase of the Sun. The second reason is partially based on the first one. During this slow latitude scan Ulysses was slowly descending from high latitudes to the ecliptic plane. Naturally it was also slowly probing the transition between the fast solar wind coming from the polar coronal hole because it was gradually traveling over the border of the coronal hole. This was especially possible during that time period because the shape of the polar coronal holes is much plainer during the Sun's quiet time. The probing of the coronal hole border can be seen in figure 2 of the publication. Here it is evident that Ulysses was crossing the same CIR over a time period of nearly 300 days.

5.2 BRIEF SUMMARY OF THE PUBLICATION

The results presented in this publication show that not only the distance of a source field line to the border of the coronal hole determines the solar wind type, but also that the shape of the field lines plays an important role. To produce slow solar wind, a source field line must follow the bending of the coronal hole border. Field lines which foot points are close to the coronal hole border on the photosphere but bent away from it while ascending towards the source surface typically produce fast solar wind.
Additionally, this is the fist publication that we know of that not only determines the photospheric sources of the solar wind, but also resolves the path of the solar wind through the corona for several height levels between photosphere and source surface, thereby creating height profiles of the solar wind's source field lines.

The following article is reproduced from Peleikis et al. (2016), with the permission of AIP Publishing.
The article is a peer reviewed proceedings to the Solar Wind 14 conference.

Own Contribution to Publication: 80%

This publication was supervised by Dr. Lars Berger and Prof. Robert F. Wimmer-Schweingruber, who together with Dr. Christian Drews contributed to the scientific discussion. Martin Kruse contributed the raw PFSS data. The SWICS data extraction and data analysis, all plots and the text were contributed by the first author Thies Peleikis.

Investigation of Solar Wind Source Regions Using Ulysses Composition Data and a PFSS Model

Thies Peleikis[1,a),b)], Martin Kruse[1], Lars Berger[1], Christian Drews[1] and Robert F. Wimmer-Schweingruber[1]

[1]*Institut of Experimental and Applied Physics, Christian Albrechts Universitaet Kiel, Germany.*

[a)]Corresponding author: peleikis@physik.uni-kiel.de

[b)]URL: http://www.ieap.uni-kiel.de/et/

Abstract. In this work we study the source regions for different solar wind types. While it is well known that the fast solar wind originates from inside Coronal Holes, the source regions for the slow solar wind are still under debate. For our study we use Ulysses compositional and plasma measurements and map them back to the solar corona. Here we use a potential field source surface model to model the coronal magnetic field. On the source surface we assign individual open field lines to the ballistic foot points of Ulysses. We do not only consider the photospheric origin of these field lines, but rather attempt to trace them across several height levels through the corona. We calculate the proximity of the field lines to the coronal hole border for every height level. The results are height profiles of these field lines. By applying velocity and charge state ratio filters to the height profiles, we can demonstrate that slow wind is produced close to the coronal hole border. In particular, we find that not only the proximity to the border matters, but also that the bending of the field lines with respect to the coronal hole border plays a crucial role in determining the solar wind type.

Introduction

The Solar Wind (SW) is most commonly divided into two types, namely the Fast Solar Wind (FSW) and the Slow Solar Wind (SSW), with the SSW typically being below $v_{sw} = 500\,\mathrm{km/s}$ and the FSW being above $v_{sw} = 500\,\mathrm{km/s}$. Despite this denotation, many SW parameters vary within the SW types [1]. Especially interesting are the ionic charge states, since these are direct coronal signatures which no longer vary when the wind propagates outwards [2]. The FSW is associated with Coronal Holes (CH) [3], regions where the plasma in the corona is less dense with a lower electron temperature and open magnetic field structures. During the solar minimum, the SSW is observed at low heliospheric latitudes, the so called streamer belt. Here the coronal plasma is denser and the electron temperature is higher compared to the CHs. Also these regions are filled with closed magnetic field structures were the plasma is trapped. The SW parameters we measure inside the SSW indicate that its origin lies within these closed field line regions. Nevertheless, the plasma has to be released from there before it can contribute to the SW. There are several candidates for the source regions of the SSW, like the S-web [4] or the general Coronal Hole Border (CHB) [5], most resolve around reconnection processes between open and closed magnetic field lines where the plasma inside these closed field line structures is released by the magnetic reconnection. If reconnection processes between open and closed magnetic field lines are responsible for the release of the SSW, its source location should be in close proximity to the CH border. To address this possible correlation of the geometry of the field lines and the solar wind type, we trace in-situ measured SW back to its coronal origin, using Ulysses measurements and a Potential Field Source Surface (PFSS) model [6]. Similar work has been done where the SW has been traced back to a photospheric origin [7]. In contrast to that, we trace the wind over several height levels between photosphere and corona and investigate the curvature and proximity of the field lines to the closed field line region.

Solar Wind 14
AIP Conf. Proc. 1720, 020003-1–020003-4; doi: 10.1063/1.4943804

Method and Analysis

For our study we use Ulysses' Solar Wind Ion Composition Spectrometer (SWICS) [8], Solar Wind Plasma Experiment (SWOOPS) [9] and Vector Helium Magnetometer (VHM) [10] measurements. From SWICS we derive the ratio of O^{7+} to O^{6+} via a box rate analysis similar to [11]. SWOOPS data is used to obtain plasma data like the solar wind velocity v_{sw} and from the VHM data we derive the in-situ magnetic field polarity. We use SWOOPS data with the highest possible time resolution of 8 minutes. The SWICS and VHM data are synchronized accordingly. In order to divide the SW into different types, we apply a v_{sw} and a O^{7+}/O^{6+} ratio filter [12]. The boundaries for the filters are given as text in the panels of Figure 3. The first step in our analysis is to map the in-situ data onto the source surface of the Sun via ballistic back mapping. From there on we use a PFFS model to trace the SW further down into the corona. The input for the model are synoptic photospheric magnetograms from the Michelson Doppler Imager (MDI) on the SOHO spacecraft. To run the PFSS model we use a numerical approach with a three dimensional grid. For each of Ulysses' ballistic foot points on the source surface we identify the closest open field line. We refer to these open field lines as Source Field Lines (SFLs) and assume that the SW we measured with Ulysses streamed along them. As a measure of validity we compare the in-situ measured magnetic field polarity with the one derived from the PFSS model. A mismatch in polarities is interpreted as erroneous back mapping and the data points are discarded. Also discarded are the points, where the in-situ polarity could not be unambiguously determined. Beneath the source surface we trace the SFLs over 10 equidistant height levels down onto the photosphere. The distance between the height levels is $\delta H = 94.84$ Mm. In addition to that, we determine the border of the northern and southern CH by identifying the outermost open field lines of every height level. By interpolating between the height levels we obtain a three dimensional representation of the border between open and closed magnetic field line region. Figure 1 shows the CHB and the reconstructed SFLs for Carrington Rotation (CR) 1914, from 18th September 1996 till 15th October 1996. Next we combine the determined CH boundary with the SFLs. For every SFL we calculate the closest distance

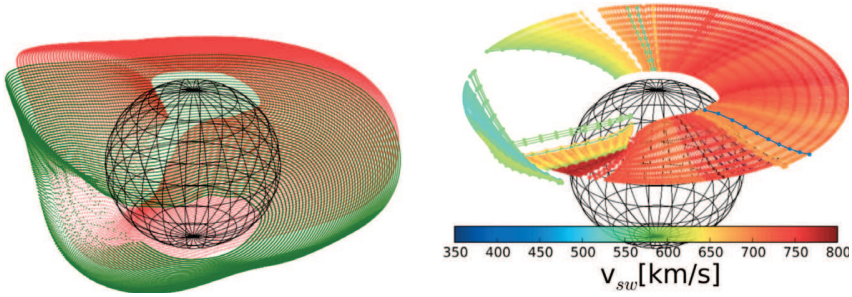

FIGURE 1. On the left side the three dimensional point clouds representing the border of the northern (red) and southern (green) coronal hole for CR 1914. On the right side the reconstructed SFLs for that CR are shown, color coded for the in-situ v_{sw}. The spherical grid in both pictures represents the photosphere

to the CHB of every height level. Thus, we create a height profile of the SFLs which shows the spatial evolution of the SFLs with respect to the CHB.

Observations and Discussion

We apply our method for the time period from CR 1913 until CR 1923, from 22nd August 1996 till 18th June 1997. Figure 2 shows v_{sw} for this period. Table 1 shows the percentages of data points with matching in-situ and PFSS magnetic polarity, subdivided into four different velocities as stated in table 1. The velocities are chosen so that they

TABLE 1. The percentage of correctly back mapped data point for the respective v_{sw} in units of km/s.

v_{sw}:	$v_{sw} < 450$	$450 < v_{sw} < 550$	$550 < v_{sw} < 700$	$700 < v_{sw}$
correct:	63.75 %	76.21 %	71.18 %	95.60 %

contain roughly the same number of data points to make them comparable, while dividing the SW into different types.

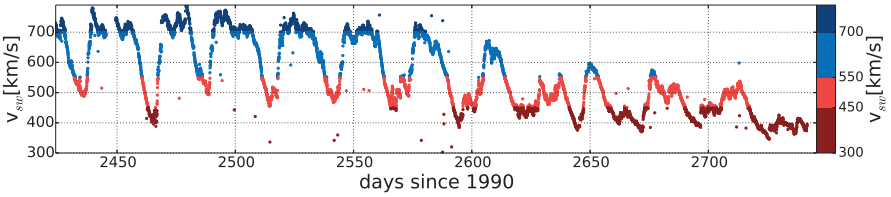

FIGURE 2. Time series of v_{sw} in the investigated time period. This period is part of Ulysses' slow latitude scan. The color coding corresponds to different velocities, the same as in table 1.

With the incorrectly mapped points discarded we can now look at the height profile of the SFLs. Figure 3 shows the height profile of the SFLs ordered by v_{sw} and the ratio O^{7+}/O^{6+}. Note that the photosphere and the lowest height level are not included in the analysis because it is difficult to determine the CHB for these heights. We show the spatial

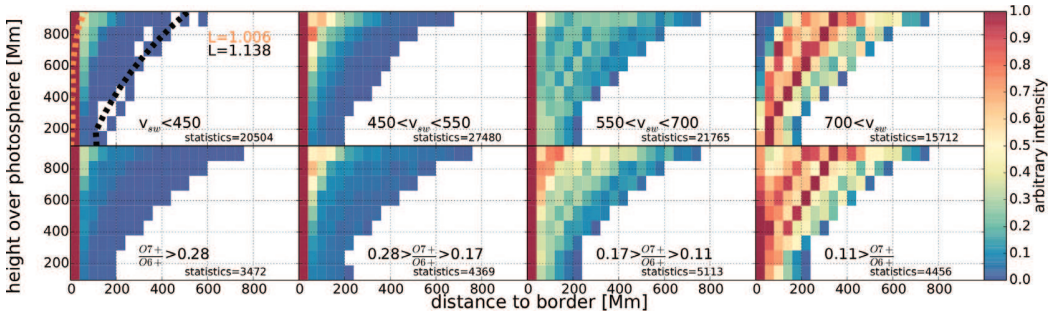

FIGURE 3. Height profile for the SFLs. The upper row of panels shows four different v_{sw} filter, v_{sw} in units of km/s. The lower row shows four different filter for the O^{7+}/O^{6+} ratio. The y-axis gives the height over the photosphere. The x-axis gives the calculated distance to the CHB at the respective height level. Each row of bins is normalized to the maximum of that row, therefore the highest bins are one. In panel one two SFLs are shown to illustrate the L parameter from equation 1 together with their respective L values.

distributions of the SFLs in form of 2d histograms. The y-axis gives the height above the photosphere, where each row of bins is equivalent to one PFSS height level. The x-axis gives the calculated distance to the CHB at that respective height level. Both axes are in units of Mm. Each row of bins is normalized to its respective maximum. The color coding shows the normalized number of occurrences. The left edge of each panel in Figure 3 can be understood as the CHB, while the right side of each panel can be conceived as the deeper parts of the CH. For example, the upper rightmost panel shows the majority of field lines being densely seated close to the CHB, but with increasing height over the photosphere they bend away from the border to form a broader distribution close to the source surface. It is obvious that the spatial distribution of the SFLs depends heavily on v_{sw} and accordingly on the O^{7+}/O^{6+} ratio. Compared to the FSW, the SFLs of highly charged SSW run closer to the CHB, implying that it is the border of the CH which produces the SSW. This is in agreement with prevalent ideas [5]. But if only the lower height levels are taken into account, the distinction between SW types is not very clear. Therefore we introduce the length of the SFL as an additional parameter which takes the bending of the SFLs into account in order to better discern between the SW types:

$$L = \frac{1}{(N-1)\delta H} \sum_{i}^{N-1} \sqrt{(\delta H^2 + (d_{i+1} - d_i)^2)} \tag{1}$$

N is the number of height levels and d_i is the distance to the CHB on height level i. It is important to note that L is not the absolute length of a field line, but the length in the coordinate system displayed in figure 3. In the first panel of figure 3, two field lines and their corresponding L are shown. Figure 4 shows L in form of 2d histograms, with the distance to the CHB on the lowest height level as x-axis. Hence the x-axis is basically the lowest bin in figure 3. The y-axis gives L. L is one for field lines which do not change their distance to the CHB with increasing height, while it increases for field lines which are bending away from the border. The left panels in figure 4 again show that SSW as well as FSW cover the same range on the x-axis, meaning that the distance to the border alone does not discriminate between the SW types. But the L parameter, which contains information from all the height levels shows that the SFL

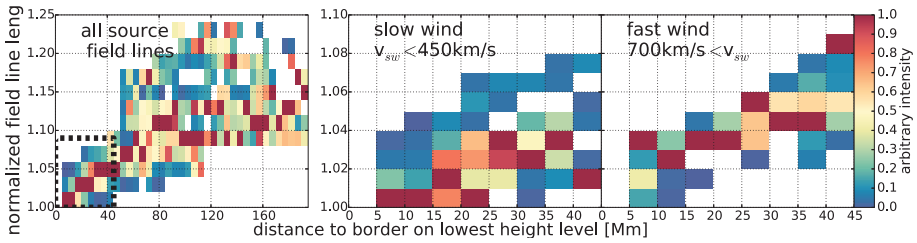

FIGURE 4. The normalized field line length plotted against the distance to the CHB shown as a 2d histogram. Each column of bins is normalized to its respective maximum. The left panel shows the whole data set, the middle panel the SSW and right panel the FSW filtered by v_{sw}. Both panels to the right show only a fraction of the left panel, indicated by the dashed box in the right panel.

for the FSW bend away from the border, indicated by a higher L at the same distance to the CHB. The SFL for the SSW retain their proximity to the border while ascending to the source surface.

Conclusion

Our analysis demonstrates that not only the proximity of a SFL but especially its curvature with respect to the CHB determines the SW type, as shown by the parameter L. L may bear some resemblance to the expansion factor f_s from the Wang-Sheeley model. But while Wang and Sheeley derive the ratio of the magnetic field at the source surface and at the photosphere for each field line, our parameter L results from a strictly geometrical analysis of the field lines. One has to be careful to draw quantitative statements from our analysis. Table 1 shows that especially for the SSW many data points have to be discarded because of the uncertainties in the back mapping, and the limitations of the PFSS model. Desite these limitations our findings are in good agreement with prevalent ideas. If magnetic reconnection is the driving force which releases the SSW, the curvature of the field lines with respect to the CHB plays an important role. The SFLs must stay in proximity to the CHB while ascending through the corona, so that the interactions between open and closed field lines can take place even at higher altitudes. As stated above, our analysis confirms the described behavior.

REFERENCES

[1] J. Geiss, G. Gloeckler, and R. von Steiger, Space Science Reviews **72**, 49–60 (1995).
[2] P. Bochsler, Reviews of Geophysics **38**, 247–266 (2000).
[3] A. S. Krieger, A. F. Timothy, and E. C. Roelof, Solar Physics **29**, 505–525 (1973).
[4] S. K. Antiochos, Z. Mikić, V. S. Titov, R. Lionello, and J. A. Linker, The Astrophysical Journal **731**, p. 112 (2011).
[5] N. A. Schwadron, D. J. McComas, H. A. Elliott, G. Gloeckler, J. Geiss, and R. von Steiger, Journal of Geophysical Research (Space Physics) **110**, p. 4104 (2005).
[6] M. D. Altschuler and G. Newkirk, Solar Physics **9**, 131–149 (1969).
[7] M. Neugebauer, R. J. Forsyth, A. B. Galvin, K. L. Harvey, J. T. Hoeksema, A. J. Lazarus, R. P. Lepping, J. A. Linker, Z. Mikic, J. T. Steinberg, R. von Steiger, Y.-M. Wang, and R. F. Wimmer-Schweingruber, Journal of Geophysical Research **103**, 14587–14600 (1998).
[8] G. Gloeckler, J. Geiss, H. Balsiger, P. Bedini, J. C. Cain, J. Fischer, L. A. Fisk, A. B. Galvin, F. Gliem, D. C. Hamilton, J. V. Hollweg, F. M. Ipavich, R. Joos, S. Livi, R. A. Lundgren, U. Mall, J. F. McKenzie, K. W. Ogilvie, F. Ottens, W. Rieck, E. O. Tums, R. von Steiger, W. Weiss, and B. Wilken, Astronomy and Astrophysics Supplement Series **92**, 267–289 (1992).
[9] S. J. Bame, D. J. McComas, B. L. Barraclough, J. L. Phillips, K. J. Sofaly, J. C. Chavez, B. E. Goldstein, and R. K. Sakurai, Astronomy and Astrophysics Supplement Series **92**, 237–265 (1992).
[10] A. Balogh, T. J. Beek, R. J. Forsyth, P. C. Hedgecock, R. J. Marquedant, E. J. Smith, D. J. Southwood, and B. T. Tsurutani, Astronomy and Astrophysics Supplement Series **92**, 221–236 (1992).
[11] R. von Steiger, N. A. Schwadron, L. A. Fisk, J. Geiss, G. Gloeckler, S. Hefti, B. Wilken, R. F. Wimmer-Schweingruber, and T. H. Zurbuchen, Journal of Geophysical Research **105**, 27217–27238 (2000).
[12] L. Zhao, T. H. Zurbuchen, and L. A. Fisk, Geophysical Research Letters **36**, p. 14104 (2009).

5.3 SUPPLEMENTAL CONSIDERATIONS

Based on this publication additional work is done to improve on the presented analysis. As mentioned, the great distance between Ulysses and the Sun during the slow latitude scan is not beneficial for the ballistic back mapping. Therefore, to remove this shortcoming, the study is done again with ACE data, because ACE is much closer to the Sun, with the distance between Sun and spacecraft being about 0.99 AU. This minimizes the uncertainties that are introduced to the ballistic back mapping.
The evaluation of the distance to the coronal hole border has also been improved upon. In the publication the outermost open field lines of the coronal hole are identified and treated as coronal hole border. This method has two distinctive disadvantages. Firstly, this does not produce the actual distance to closed field line region. Secondly, this method does not work very well for low height levels close to the photosphere due to the fractal nature of the open field line distribution on these low height levels, compare with the left panel in figure 17. Instead the closed field lines are now also extracted from the PFSS model and are taken together in form of a point cloud in cartesian space. For more information on the analysis of the field lines geometry see section 3.4
Another improvement is made for the field lines maps generated by the PFSS model. While in the publication there are ten height levels between photosphere and source surface available, that number is increased to 100. That means that the shape of the source field lines can be studied in greater detail. In Figure 28 the

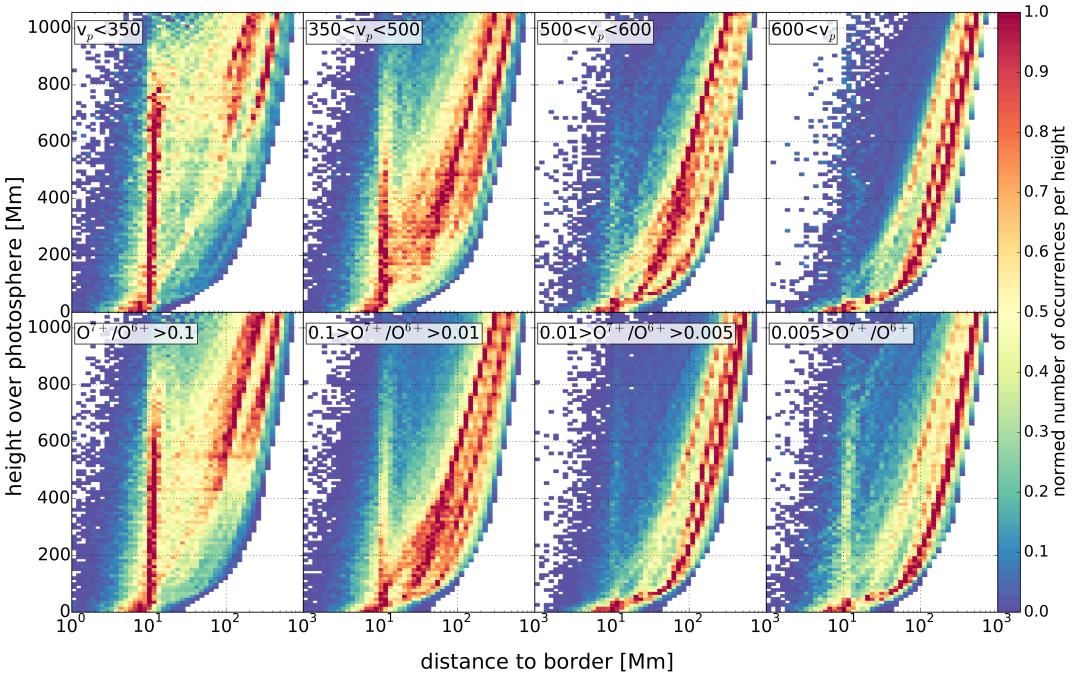

Figure 28: Recreation of figure 3 in the publication, but with ACE measurements. The y axis gives the height over the photosphere and the x axis the distance to the coronal hole border. The color coding represents the normed number of occurrences, each row of bins is normalized to its respective maximum.

source field line profiles of figure 3 of the publication has been replicated. In con-

trast to the figure from the publication here the x axis is shown in logarithmic scale. Again, for the upper row of panels different velocity filters have been applied and O^{7+}/O^{6+} filters are applied to the lower row. When figure 28 is compared to figure 3 from the publication the same general behavior can be seen.
Another point to consider is that in actuality, the velocity and charge state filters are to some degree arbitrary. A different division can be achieved by using the categorization scheme of Xu and Borovsky (2015), see section 2.2. In figure 29 the source field lines profiles are shown divided into three plasma categories after Xu and Borovsky (2015). Note that ejecta plasma has been left out, since it is not a part of the quiescent solar wind. The left panel in figure 29 shows the source field line

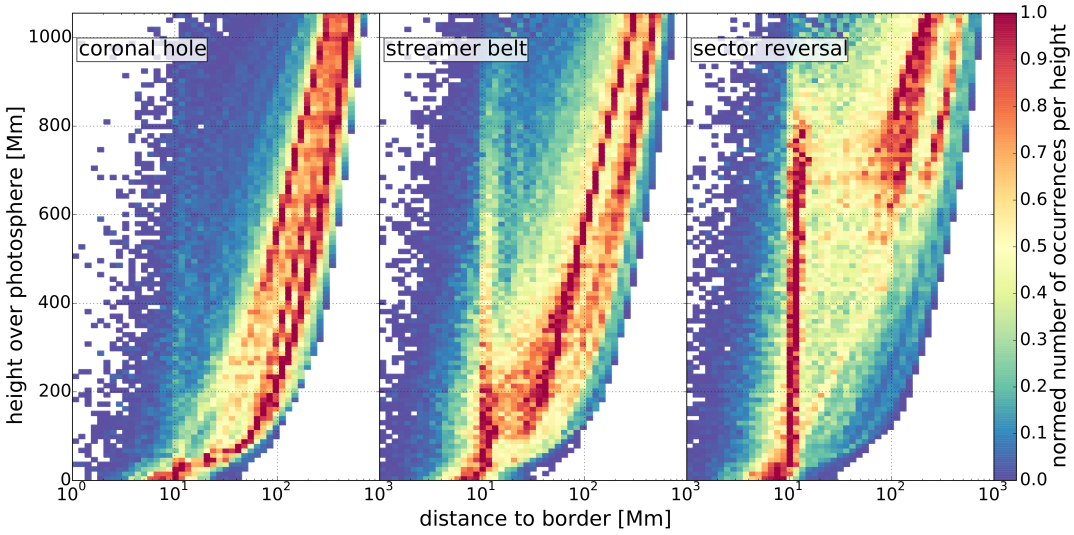

Figure 29: The source field lines height profile like in figure 28, but divided into coronal hole, streamer belt and sector reversal plasma, as defined by Xu and Borovsky (2015). Again, the y axis gives the height over the photosphere and the x axis the distance to the coronal hole border. The color coding represents the normed number of occurrences, each row of bins is normalized to its respective maximum.

profile for coronal hole plasma. It can be clearly seen that these field lines bend away from the coronal hole border as they rise from the photosphere towards the source surface. The opposite is true for the field lines which produced sector reversal plasma, which are shown in the right panel. Here it can be seen that the majority of source field lines do not change their distance to the closed field line region. In other words, these field lines cling to the coronal hole border. Only close to the source surface they break from this behavior and diverge from the border. The middle panel shows the source field lines profile of streamer belt plasma. It seems to occupy a middle ground between coronal hole and sector reversal plasma. The derived results are in agreement with the prevailing ideas regarding the sources and origin of streamer belt and sector reversal plasma. But ultimately it is not possible to identify the precise source regions of the slow solar wind. To achieve that the Solar Orbiter mission has been devised. Solar Orbiter is a spacecraft equipped with remote sensing instruments and in-situ particle detectors which will closely approach the Sun, thereby being well suited for the search for the slow solar wind's source regions. In the next chapter a measurement scheme for Solar Orbiter's remote sensing instrumentation is devised in order to enable it to do its task.

6 A MEASUREMENT SCHEME FOR SPICE ON SOLAR ORBITER

In this chapter the second publication of this work is covered. Here a measurement scheme is devised for the Spectral Imaging of the Coronal Environment (SPICE) on the upcoming Solar Orbiter mission (Müller et al., 2013). As the name already implies SPICE is a coronal spectrograph that images EUV wavelengths with a high resolution. From these measurements plasma temperature, composition, flow velocity and the presence of plasma turbulence can be inferred, see Fludra et al. (2013) for more information.
Solar Orbiter is a mission carried out by the European Space Agency (ESA), it is planned to launch in February 2019 and it is intended to investigate the origin of the solar wind, amongst other things. For that purpose its orbit will bring it particularly close to the Sun, well within the orbit of Mercury down to 0.288 AU. Besides SPICE, which is a remote sensing instrument, Solar Orbiter will carry several in-situ particle detectors combined in the Solar Wind Analyzer (SWA) suite (Livi et al., 2012) that measure the solar wind locally. The combination of in-situ and remote sensing instruments together with the close proximity to the Sun constitute the novelty of Solar Orbiter. The Helios mission for example reached a similar vicinity to the Sun but carried no remote sensing instruments, while SOHO carries both remote and in-situ instrument, but is located at 1 AU. The idea behind Solar Orbiter is to combine the in-situ and the remote measurements in a way that remotely observed features on the Suns surface or in the corona can be directly related to solar wind observations made at the spacecraft. Due to Solar Orbiters proximity to the Sun it can be assumed that the observed solar wind has not undergone many dynamical processes that would otherwise alter its pristine conditions.

6.1 MOTIVATION

The optimal modus operandi for Solar Orbiter would be to observe the same solar wind package twice. The first time remotely with SPICE on the solar surface at the moment of its formation and then later a second time in-situ with its on board particle detectors. That way it will be possible to directly link the properties of the in-situ measured plasma to its source location on the Sun.
Unfortunately, this is not an easy task. Compared to other remote sensing instruments like for example SDO or SOHO, the SPICE field of view does not cover a whole hemisphere of the Sun. Due to its finite coverage it is possible for SPICE to miss the source region of a later in-situ measured solar wind stream. In order to maximize the number of covered source regions a measurement scheme needs to be devised. Because Solar Orbiter will only have brief remote sensing windows during its orbit it is especially important to ensure an optimal utilization of these.

6.2 BRIEF SUMMARY OF THE PUBLICATION

Two approaches on a measurement scheme are attempted. For the first approach a direct prediction of the solar winds source regions is made. Here the idea is that SPICE is orientated at each source region individually. The problem with this method is that SPICE will probably not be able to be adjusted on the fly for each individual source region. Therefore, the second approach consists of a method were six images of SPICE are vertically stacked to form an elongated field of view that covers the whole Sun latitude wise. This enlarged field of view is then aimed at the Sun with a certain leading angle. For this purpose the optimal leading angle is determined that leads to a maximum number of source regions captured at the moment of the solar winds release.

The following article is reproduced from Peleikis et al. (2017), with permission ©ESO.

OWN CONTRIBUTION TO PUBLICATION: 80%

This publication was supervised by Dr. Lars Berger and Prof. Robert F. Wimmer-Schweingruber, who both contributed to the scientific discussion. Martin Kruse contributed the raw PFSS data. Dr. Bala Poduval supported this publication with coronal magnetic field data computed with the Current Sheet Source Surface (CSSS) model. The simulations, analysis, all plots and the text were made by the first author Thies Peleikis.

Astronomy & Astrophysics manuscript no. peleikis_pfss_spice
March 31, 2017

Origin of the solar wind: A novel approach to link in situ and remote observations

A study for SPICE and SWA on the upcoming Solar Orbiter Mission

Thies Peleikis[1], Martin Kruse[1], Lars Berger[1], and Robert Wimmer-Schweingruber[1]

Institut of Experimental and Applied Physics, Christian Albrechts Universitaet Kiel, Germany.

March 31, 2017

ABSTRACT

Context. During the last decades great progress has been achieved in understanding the properties and the origin of the solar wind. While the sources for the fast solar wind are well understood, the sources for the slow solar wind remain elusive.
Aims. The upcoming Solar Orbiter mission aims to improve our understanding of the sources of the solar wind by establishing the link between in situ and remote sensing observations. In this paper we aim to address the problem of linking in situ and remote observations in general and in particular with respect to ESA's Solar Orbiter mission.
Methods. We have used a combination of ballistic back mapping and a potential field source surface model to identify the solar wind source regions at the Sun. As an input we use in situ measurements from the Advanced Composition Explorer and magnetograms obtained from the Michelson Doppler Interferometer on board the Solar Heliospheric Observatory. For the first time we have accounted for the travel time of the solar wind above and also below the source surface.
Results. We find that a prediction scheme for the pointing of any remote sensing instrumentation is required to capture a source region not only in space but also in time. An ideal remote-sensing instrument would cover up to $\approx 50\,\%$ of all source regions at the right time. In the case of the Spectral Imaging of the Coronal Environment instrument on Solar Orbiter we find that $\approx 25\,\%$ of all source regions would be covered.
Conclusions. To successfully establish a link between in situ and remote observations the effects of the travel time of the solar wind as well as the magnetic displacement inside the corona cannot be neglected. The predictions needed cannot be based solely on a model, nor on observations alone, only the combination of both is sufficient.

Key words. solar wind - Sun: magnetic topology - Sun:corona - Space vehicles: instruments

1. Introduction

The solar wind which shapes the heliosphere has been intensively studied for many years. Measurements of the solar wind are made by in situ particle detectors on board various spacecraft distributed over different orbits around the Sun. Variations and patterns in the in situ parameters have been used to categorize the solar wind into different types (Geiss et al. 1995). The earliest categorization scheme discerns the solar wind by its velocity into two types, namely the fast and the slow solar wind (Schwenn et al. 1981). Similar discriminations can be made by other parameters such as the density, temperature, charge state and elemental composition. Although the solar wind's in situ parameters have been measured over a long time period, the precise origin of the solar wind is yet elusive, with the exception of lowly charged fast solar wind, which originates from structures in the corona called coronal holes (Krieger et al. 1973). Nevertheless the in situ parameters do contain information about the solar wind's origin. The measured elemental and ionic composition for example are photospheric and coronal signatures, which are assumed to stay unchanged beyond a certain distance above the Sun's surface. The ionic charge states are directly linked to the electron density and temperature in the corona (Bochsler 2000). The upcoming Solar Orbiter mission intends to determine the source regions of the slow solar wind in the corona. For that purpose it is planned to combine in situ particle measurements with a solar spectrograph (Hassler et al. 2011), the Spectral Imaging of the Coronal Environment (SPICE) instrument (Fludra et al. 2013). The in situ instruments are the Proton Alpha Sensor (PAS) and the Heavy Ion Sensor (HIS) of the Solar Wind Analyser (SWA) suite. The idea is to link the in situ observations to their coronal origin which are going to be remotely measured by SPICE. A comparable principle has been described by Landi et al. (2012). In the case of SPICE the remote observation is supposed to happen prior to the in situ observation, in order to observe the coronal structure ideally at the time of the solar wind's departure.

A common technique to locate the heliographic origins of in situ measurements is to map the solar wind back onto the solar surface, thereby obtaining heliospheric coordinates for the source region. The back mapping of the solar wind is done in two parts. The first part is a ballistic mapping of the wind back to the outer corona and the second part is a magnetic mapping trough the corona down to the photosphere. For the first part, the solar wind speed and for the second part, remote magnetograms and a model of the coronal magnetic field based upon the magnetograms are needed.

The basic concept of two-way back mapping has been used before for various spacecraft and instruments, see for example Neugebauer et al. (1998). But compared to former attempts, Solar Orbiter brings several remarkable advantages. Firstly, like SOHO before it, Solar Orbiter combines in situ and remote in-

Article published by EDP Sciences, to be cited as https://doi.org/10.1051/0004-6361/201629727

strumentation on one spacecraft. Usually observations from several different spacecraft and observatories were needed for any back mapping studies of the solar wind. Secondly Solar Orbiter will be very close to the Sun with radial distances down to 0.28 AU. On such close distances the ballistic back mapping will be especially effective since the solar wind has undergone less dynamic processing on its way to the spacecraft. Normally this is a major problem when back-mapping from 1 AU.
In this paper we explore different methods for determining the source regions of the solar wind. SPICE will image the source regions of a solar wind package prior to its in situ observation. To ensure that SPICE points at the correct region a predictive forward mapping of the solar wind is needed. This includes a prediction of the solar wind source regions, a prediction of the solar wind speeds prior to its measurement and consequently an estimation of its travel time. Only then can one predict where SPICE has to be pointed at and when it has to take a spectrogram of the Sun's surface. Our goal is to find promising measurement patterns and investigate their feasibility. In order to do so we have looked at the influence of the ballistic as well as the magnetic mapping by simulating the measurement sequence of SPICE. For these simulations we combined real solar wind in situ data measured by the Advanced Composition Explorer (ACE) and real magnetograms from the Michelson Doppler Interferometer (MDI). To validate the different methods, the ability of SPICE to observe the predicted source regions was calculated in each simulation.

2. Methods and Analysis

In this section, we describe the general procedure of our analysis. During the course of our analysis we applied modifications and improvements to the procedure, but the underlying method is based on the following descriptions.
In Fig. 1 the path of the solar wind from its origin to the spacecraft is sketched for two different solar wind speeds. When traveling from its origin to the spacecraft, the solar wind's path is divided into two distinct regions. First it has to traverse the corona which is dominated by strong magnetic fields. Here, the plasma has to stream along the magnetic field lines. Beyond the source surface in interplanetary space the situation is reversed and the magnetic field has to follow the plasma flow.
Both regions must be considered individually due to their different physics. The second part of the solar wind's path can be calculated via ballistic back mapping under the assumptions that the solar wind velocity does not change between corona and spacecraft and a strictly radial expansion of the solar wind plasma (Krieger et al. 1973). During the solar wind's travel time the Sun continues its rotation which leads to a displacement between spacecraft coordinates and source coordinates. We call this the ballistic displacement.
Unfortunately, the first part of the solar wind's path cannot be simply described by ballistic back mapping. The magnetic pressure inside the corona exceeds the kinetic pressure, therefore the plasma has to follow the magnetic field lines. In order to trace the solar wind further through the corona, the coronal magnetic field line configuration has to be known. Since it is not possible to measure the complete magnetic topology inside the corona directly, one has to introduce a model to simulate the course of the field lines. The Potential Field Source Surface (PFSS) model by Altschuler & Newkirk (1969) or Schatten et al. (1969) is commonly used for this task. It calculates the magnetic field strength and direction in a region between the photosphere and an artificial surface called the source surface. It needs photospheric magnetograms as input parameter. With the assumption that the solar wind plasma can only flow along the magnetic field lines it can now be traced through the corona to its photospheric origin (Neugebauer et al. 1998). The bending and twisting of the field lines causes an additional displacement between spacecraft and source coordinates. We call this magnetic displacement.
We note that there are other models beside the PFSS model in use. The Current Sheet Source Surface (CSSS) model has been shown to be better than the PFSS model when it comes to solar wind speed predictions (Poduval & Zhao 2014). At the end of this paper we compare the results obtained with the PFSS model with those obtained from a CSSS model

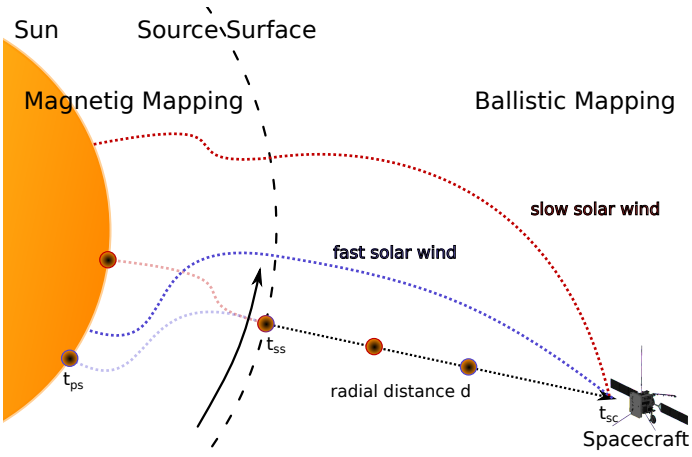

Fig. 1. Displacement between the spacecraft's coordinates and the source region's coordinates. The magnetic connection of a fast (blue) and slow (red) solar wind package are shown in the reference frame of the spacecraft. The bending of the field lines below the source surface causes the magnetic displacement, the rotation of the Sun during the travel time from the source surface to the spacecraft causes the ballistic displacement. A solar wind package starts at the time t_{ps} at the photosphere, reaches the source surface at t_{ss} and is measured at t_{sc} by the spacecraft. The colored dashed lines indicate the magnetic connection between spacecraft and the solar wind's sources.

2.1. Ballistic back mapping

For our consideration we assume a spacecraft orbiting the Sun. Its position is given in a heliospheric coordinate system corotating with the Sun, that is, the Carrington coordinate system, with λ_{sc} heliospheric or Carrington longitude, ϕ_{sc} heliospheric latitude and its distance to the source surface d. The source surface is a virtual sphere around the Sun with a radius of typical $2.5R_{\odot}$. It is the outer boundary for the PFSS model and it marks the point where the magnetic field lines are supposed to radially expand. In our consideration it also marks the point where the plasma no longer has to follow the magnetic field lines. A solar wind package measured by this spacecraft at the time t_{sc} can be mapped back onto the source surface via ballistic back mapping, hereby determining the ballistic footpoint λ_{bfp} and ϕ_{bfp} of the spacecraft. It can be calculated analytically:

$$\begin{aligned} \lambda_{\mathrm{bfp}}(d, v_{sw}) &= \lambda_{sc} + \frac{\omega d}{v_{sw}}, \\ \phi_{\mathrm{bfp}} &= \phi_{sc}, \end{aligned} \tag{1}$$

where v_{sw} is the speed of the measured solar wind package and ω is the angular velocity of the Sun. Consequently the time t_{ss}

when the solar wind starts at the source surface calculates to

$$t_{ss}(d, v_{sw}) = t_{sc} - \frac{d}{v_{sw}}. \quad (2)$$

Obviously, λ_{bfp} is a function depending on v_{sw} and d. The difference between the spacecraft coordinates and the ballistic footpoint is the afore mentioned ballistic displacement $\lambda_{\mathrm{dis}}^{\mathrm{bm}} = \frac{\omega d}{v_{sw}}$ and $\phi_{\mathrm{dis}}^{\mathrm{bm}} = 0$. For a spacecraft traveling between 1 AU and 0.2 AU and observing solar wind with speeds between 250 kms^{-1} and 900 kms^{-1}, $\lambda_{\mathrm{dis}}^{\mathrm{bm}}$ can reach rather high values of up to 100 °. Here the advantage of the Solar Orbiter mission becomes apparent since it will only do its remote observation in regions with $d \leq 0.4$ AU. Conveniently, $\lambda_{\mathrm{dis}}^{\mathrm{bm}}$ is always analytically determined. We note that the latitude ϕ_{bfp} is not affected by the ballistic mapping.

2.2. Magnetic mapping

To map from the source surface deeper into the corona to the photosphere the PFSS model has to be applied. It needs photospheric magnetograms as input parameters in order to model the coronal magnetic field. These magnetograms are typically taken over the course of one Carrington Rotation (CR). One of the major problems of the PFSS model lies in the assumption of a current free state in the corona. This is not essentially correct in reality, especially not for the active Sun. Therefore the correctness of the PFSS model strongly depends on the solar activity (Koskela et al. 2015). In general the best feasibility of the model is given for the quiet times of the solar cycle.
With the PFSS model applied each ballistic footpoint is related to the closest open field line on the source surface. We call these field lines source-field lines. They are then traced down to the photosphere. Under the assumption that the solar wind traveled along these source-field lines it has now been mapped magnetically to its photospheric origin. The bending of these field lines introduces an additional displacement λ_{dis}^{pfss} and ϕ_{dis}^{pfss} between the ballistic footpoint on the source surface and the photospheric footpoint of the source-field line. This is the aforementioned magnetic displacement. The coordinates for the photospheric source regions evaluate then to

$$\begin{aligned} \lambda_{sr}(d, v_{sw}, cr) &= \lambda_{sc} + \lambda_{\mathrm{dis}}^{\mathrm{bm}}(d, v_{sw}) + \lambda_{dis}^{pfss}(cr) \\ \phi_{sr}(cr) &= \phi_{sc} + \phi_{dis}^{pfss}(cr). \end{aligned} \quad (3)$$

Here, cr depicts the CR used to derive $\lambda_{diss}^{pfss}(cr)$ and $\phi_{diss}^{pfss}(cr)$, that is, magnetic field data from that CR were used as input for the PFSS model. Figure 2 shows an example of the magnetic mapping. Shown are the source surface, the photosphere, the ballistic footpoints and the respective source-field lines. The magnetic displacement induced by the bending of the field lines in heliographic longitude and latitude is apparent.
The time when the solar wind starts at the photosphere calculates to

$$t_{ps}(d, v_{sw}) = t_{sc} - \left(\frac{d}{v_{sw}} + t_{pet}\right). \quad (4)$$

The time t_{pet} is the plasma escape time, that is, the time the solar wind package needs to travel along the field lines to the source surface. The time t_{pet} cannot be measured by any means, but it can be estimated by simulating the passage of a solar wind plasma packet through the corona. In order to track a plasma packet through the magnetically dominated lower corona up to

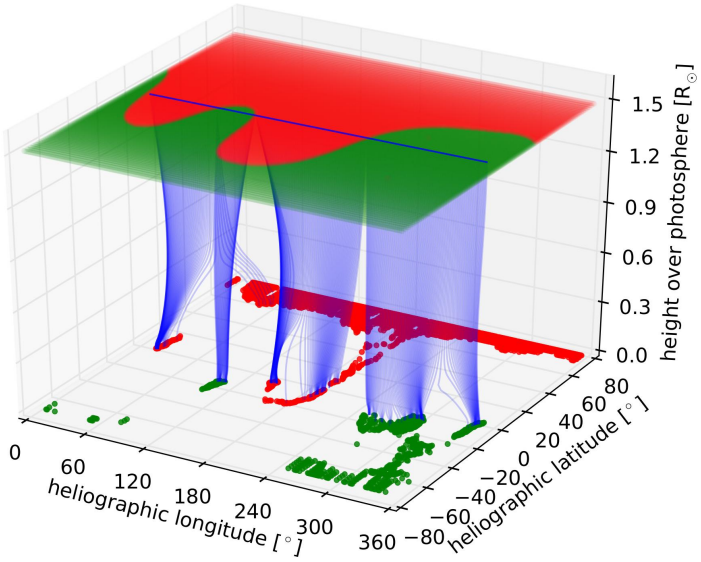

Fig. 2. Magnetic field map to illustrate the PFSS mapping. The intersection points with the source surface and foot points of the open magnetic field lines of the PFSS model are shown in red and green, where the colors depict the inward and outward polarities. The determined source-field lines and their course through the corona are shown in blue. The PFSS map corresponds to CR 2050, the underlying magnetogram is based on MDI observations.

the source surface, we analyzed several open flux tube geometries computed by Cranmer et al. (2007). Terminal velocities range from 344 km/s for the active region model to 753 km/s for the coronal hole model. We computed the package travel time from the transition region at about $r = 1.01\,\mathrm{R}_{\odot}$ to the source surface at $r = 2.5\,\mathrm{R}_{\odot}$ by reading in the velocity profiles to an equidistant grid and integrating via a Runge-Kutta (RK4) method. Results are shown in Table 1. Unfortunately, the magnetic mapping cannot be analytically calculated since it depends on the magnetic configuration at the Sun. The necessary input magnetograms are taken from the Michelson Doppler Interferometer (MDI) (Scherrer et al. 1995) on board of the Solar and Heliospheric Observatory (SOHO) spacecraft.

Table 1. Terminal velocities and travel times from transition region to source surface for different flux tube models. Based on Cranmer et al. (2007).

Model	Terminal velocity [kms^{-1}]	t_{pet} (h)
active	344	17.9
equator	498	14.8
pole	754	4.45
theta12	738	4.32
theta20	696	3.88
theta24	659	3.57
theta25	574	5.82
theta28	550	9.93

2.2.1. Spread and magnitude of the magnetic displacement

In this section we investigate the spread and magnitude of the magnetic displacement. To achieve this we calculated the magnetic displacements that a spacecraft would encounter on its orbit around the Sun if it were to attempt to back map observed solar wind. This was done with the PFSS model for 19 consecutive CRs from 2040 until 2058. These CRs are well

within one of the quiet times of the Sun's activity cycle. This

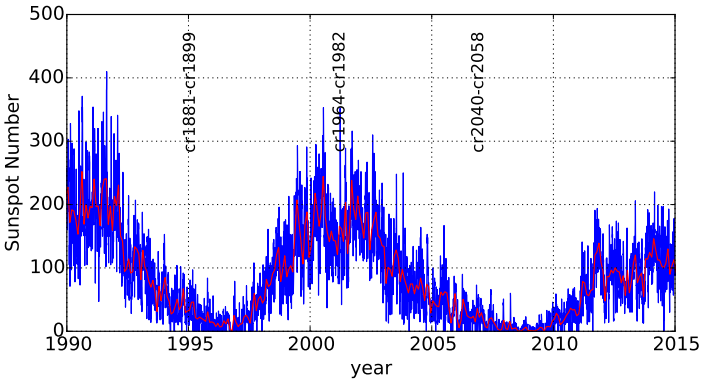

Fig. 3. Sunspot number as a function of time. The blue curve gives the actual sunspot number and the red curve the monthly average. The variation in the Sun's activity cycle is easily visible. The green shaded area marks the sequence of CRs we used for this study. The blue and red shaded areas mark sequences of CRs we investigated for comparison, the blue one also happens during the quiet time of the Sun while the red one happens during the active Sun. Data taken from Royal Observatory of Belgium (2016)

can be seen in Fig. 3. Here a time series of the sunspot number is shown. A high number of sunspots coincides with the active periods of the Sun and vice versa. The time period from CR 2040 until CR 2058 is marked in the figure, as is a comparable time period in the solar minimum while the red shaded area marks a period during solar maximum.

For each rotation we simulate a full orbit and disregard the ballistic displacement. Since the magnetic configuration is unique for each CR it is reasonable to use many rotations in order to cover the variability of the coronal magnetic field. Figure 4 shows the result of the calculations. All 19 CRs are

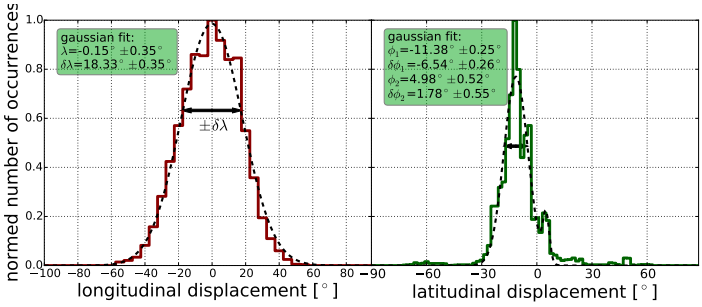

Fig. 4. Magnetic induced longitudinal (left) and latitudinal (right) displacement between source surface position and photospheric position. The y axis gives the number of occurrences for both plots normalized for the maximum. The calculation was made for an equatorial spacecraft path over the course of 19 consecutive CRs, each plot also shows a fit with a simple Gaussian (left) or a sum of two Gaussian (right). The fit parameters are given in the respective panels. The arrow marks $\delta\lambda$

combined in two histograms, one showing the longitudinal displacement between source surface and photospheric position, the other showing the latitudinal displacement. The longitudinal displacement shows a distribution which can be approximated by a Gaussian distribution with the most likely displacement of $\lambda = -0.15° \pm 0.35°$ and $\delta\lambda = 18.33° \pm 0.35°$. We note that there is no physical motivation for a Gaussian shape. Interestingly, the magnetic mapping as produced by the PFSS model does not seem to have a preferred direction in longitude. The right-hand histogram in Fig. 4 for the latitudinal displacement shows some interesting characteristics. First of all it shows a remarkable north-south asymmetry. Also the distribution itself is more complex compared to the longitudinal displacement. It cannot be described as single Gaussian, but as a sum of two or more Gaussian. In Fig. 4 we fit the histogram with a sum of two Gaussian with $\phi_1 = -11.38° \pm 0.25°$, $\delta\phi_1 = -6.54° \pm 0.26°$ $\phi_2 = 4.98° \pm 0.52°$ and $\delta\phi_2 = 1.78° \pm 0.55°$. This means that the majority of the ballistic foot points has been mapped into the southern hemisphere of the Sun and only few have been mapped into the northern hemisphere. Most of the lines originate from a $-30°$ to $10°$ band around the equator. This north-south asymmetry is not a numerical artefact but something which is indeed observed (Goel & Choudhuri 2009). In this context it is reassuring that the PFSS model is able to reproduce this asymmetry. There are two minor features around $\pm 60°$ latitude. These are the infrequent occasions where the equatorial ballistic foot points have been mapped into the polar coronal holes. We also note that the longitudinal distribution is rather broad, which emphasizes how important it is to have knowledge about the magnetic displacement when back mapping. Although the most likely displacement is ≈ 0, the majority of solar wind packages have been displaced by the magnetic field about a value $\neq 0$. Therefore it is highly improbable to estimate the photospheric origin of a measured solar wind package without using a PFSS model or a similar tool which can model the magnetic configuration inside the corona.

We repeated the method for two different time periods marked by blue and red shaded regions in Fig. 3 for comparison. The first one from CR 1881 until 1899 was also during solar minimum while the second one from 1964 until 1982 was during solar maximum. The results are shown in Fig. 5. It can be seen

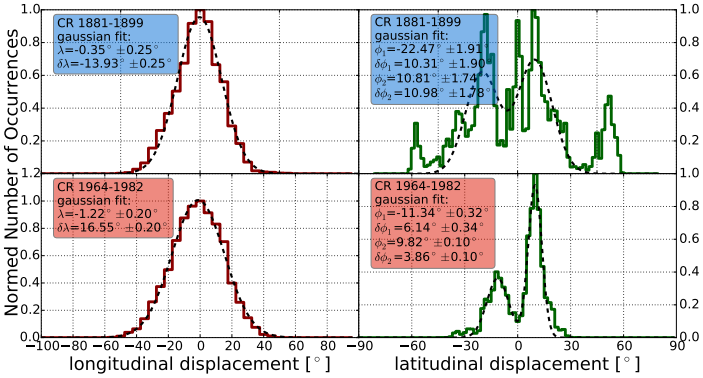

Fig. 5. Magnetic displacement for the other two time periods in Fig. 3 in the same manner as in Fig. 4. The period from 1881 until 1899 took place during the quiet phase of the Sun, but the magnetograms are from the Kitt Peak Observatory. The period from 1964 until 1982 took place during the active phase of the Sun where the PFSS model is not reliable.

that the longitudinal displacement looks similar to Fig. 4 for both time periods. In contrast the latitudinal displacement shows a different behaviour for both time periods. For the time period from CR 1881 until 1899 the distribution looks more disordered, with a broader spread and more source regions mapped into the polar coronal holes. This is most probably the case because for this time period we used input magnetograms from the Kitt Peak National Observatory (KPNT), because at that time, the SOHO mission was not yet launched. In comparison to the MDI magnetograms the magnetograms from KPNT have a lower resolution, 360x180 pixel in comparison to 3600x1080 pixel. Therefore many fine structures in the equatorial regions are not reproduced. Consequently many field lines are instead mapped

into the polar region of the Sun. The longitudinal displacement for CR 1964 until 1982 does show a stronger resemblance to the one shown in Fig. 4. Here the underlying magnetograms are also made by MDI, therefore a stronger similarity is to be expected. Since this period happened during the active Sun, the assumptions of the PFSS model may no longer be fulfilled. Especially the assumption of a current free corona can be violated. In the end these are the reasons why we chose the period from CR 2040 until 2058, here we have higher resolution magnetograms and a quiet Sun. Also, Solar Orbiter is expected to operate mainly over a similar time period during the quiet time of the Sun.

2.3. Dynamics in the coronal magnetic field

The coronal magnetic field can be a highly dynamic structure with magnetic reconnection occurring between the field lines. Moreover reconnection is a potential source of the slow solar wind, see for example Fisk (2003) and Rappazzo et al. (2012). Therefore to observe magnetic reconnection would be a relevant part of SPICE's investigations.
The reconnection of magnetic field lines alters the footpoint locations of source-field lines and hence affects the study in this paper. Unfortunately neither the PFSS model nor the CSSS model are able to predict or simulate dynamic processes in the magnetic field. Therefore we are not able to include this in the following analysis. In general the shift of a footpoint due to reconnection can be assumed to be confined to the area of one supergranule. Since the area of a supergranule accounts only for ∼4 % of SPICE's field of view, it is unlikely that the reconnection of two field lines will shift a source region so that is is no longer covered by the field of view.

2.4. Error estimation and uncertainties

Both the ballistic back mapping technique as well as the PFSS model are susceptible to errors. For the ballistic back mapping the errors derive from uncertainties in the solar wind speed measurements and dynamic processes the solar wind undergoes on its way from its source to the spacecraft. In case of the PFSS model the errors stem from uncertainties in the input magnetograms and from the general limitations of the model. For example the model is completely unable to reproduce any dynamic processes inside the corona.
To account for these uncertainties we repeated our analysis several times, at which for each run we introduce artificial statistical errors to the data. From the results for the different runs we then calculated the standard deviation.
For the ballistic back mapping we added noise with a uniform distribution with a magnitude of ±10° to the back mapped longitude λ^{bm}_{diss}. This leads to errors which are in agreement with Nolte & Roelof (1973), who proposed an error of $\Delta\lambda^{bm}_{diss} = \pm 10°$. The error for the PFSS model is more difficult to tackle. As a first attempt we added noise to the input magnetograms in order to derive different solutions for the model. To each pixel of the magnetogram the value $\pm 0.1 * I_p$ is added, where I_p is the intensity of each respective pixel. This is done according to Liu & Norton (2001) who suggest an error of up to 10% for the magnetic field measurement. In this way we took into account the error of the measurement but not the error of the PFSS model itself, which originates from the overly simplified assumptions. To estimate this intrinsic error of the PFSS model we compare each CR with its preceding and its succeeding rotation. For each source-field line we then calculated the difference $\Delta\lambda_{\pm} = \lambda^{PFSS}_{cr} - \lambda^{PFSS}_{cr\pm1}$ and the respective $\Delta\phi_{\pm}$. For both, the mean is calculated and then added as uniform noise to the respective maps. This does not reflect the actual intrinsic error of the PFSS model but it serves as maximum error estimation.

3. Solar orbiter forward mapping

Now we begin to focus on the upcoming Solar Orbiter mission. During the actual mission, remote observations are only planned during certain parts of Solar Orbiter's orbit. Those remote sensing windows occur when Solar Orbiter is particularly close to the Sun, that is, the distance between Sun and spacecraft ranges from 0.285 AU to 0.399 AU or at high heliographic latitudes. In Fig. 6 the planned orbit is shown in the x-y and

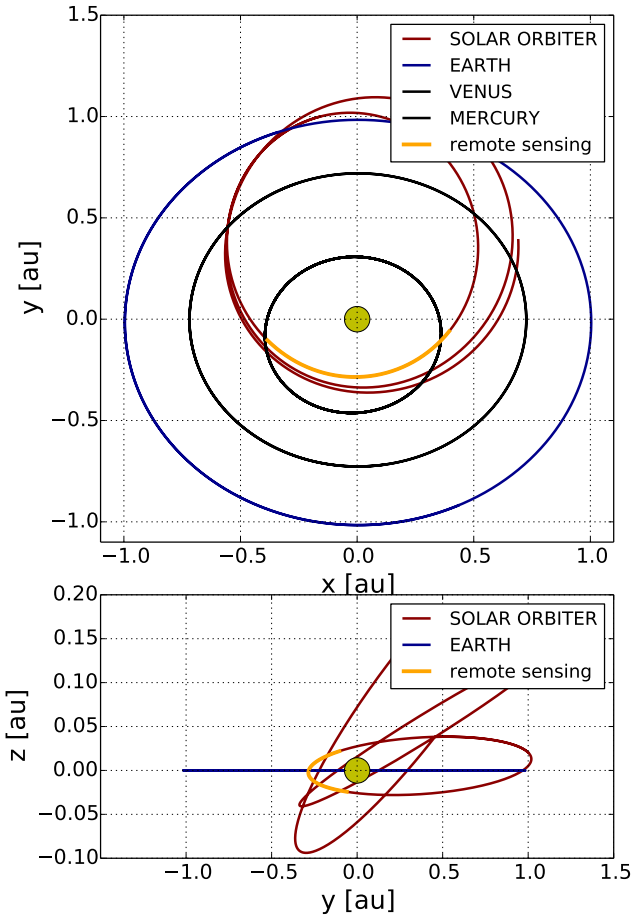

Fig. 6. Investigated orbit of Solar Orbiter shown in orange. The x and the y axes define the ecliptic plane, the z axis is perpendicular to the ecliptic. The units for the axes are AU. The full Solar Orbiter orbit is shown in red, the orbit of Earth is shown in blue, the Sun is shown as yellow circle. The upper panel also contains the orbits of Mercury and Venus as additional reference points. We note that the z axis in the lower panel has a different scale from the y axis. Hence the out-of-ecliptic extent of the orbit seems exaggerated.

in the y-z plane. It begins on the 11th of January, 2022 and ends on the 18th of July, 2023. The part of the orbit which is labeled "remote sensing" does not depict an actual remote sensing window, but marks a part of the orbit which satisfies the spacecraft-Sun distance condition for a remote sensing window.

In Fig. 1 the principle of forward mapping is illustrated. At the time t_{ps} SPICE has to image the source region of the solar wind package. The solar wind package travels through the corona and reaches the source surface at the time t_{ss}. From there it travels further through the heliosphere and is now decoupled from the Sun's rotation. At t_{sc} Solar Orbiter observes the solar wind package in situ. To successfully image each solar wind package with SPICE two parameters are needed, the release time of the solar wind at the photosphere t_{ps} and its source coordinates λ_{sr} and ϕ_{sr}. The release time t_{ps} is needed in order to determine the specific point in Solar Orbiter's orbit from where SPICE has to image the source coordinates λ_{sr} and ϕ_{sr} to capture the solar wind package at its origin. Both t_{ps} as well as the source coordinates can be determined by back mapping.
In the following simulations we construct 19 spacecraft orbits for each run. These orbits are intended to emulate the remote sensing windows of Solar Orbiter. The actual remote Sensing windows are planned to last for ten day but we do not have the precise orbit and time information. Therefore we construct them as as follows. Each orbit ranges from $\lambda = 360°$ to $\lambda = 0°$, thereby resembling one CR. The radial distance ranges from 0.285 AU to 0.399 AU, equivalent to the remote sensing window. For each of these constructed pseudo orbits we use one magnetogram from CR CR2040 to CR2058 as input parameter for the PFSS model. Hence we end up with 19 CRs each with a different magnetic configuration in the corona. For each orbit the simulation will run according to the following scheme:

1. Simulate the measurement of solar wind by using in situ solar wind data measured by the Solar Wind Electron Proton Alpha Monitor (SWEPAM) on ACE during the exact same CR. See Fig.7.

2. Determine the actual source regions of the observed solar wind by using Eq. 3. Also determine the release time with Eq. 4.

3. Predict the source regions and the release time using the preceding CR.

4. Simulate the orbit of the spacecraft again with SPICE trying to point at the predicted source regions. Thereby its field of view is projected onto the Sun's surface and it is tested if the actual source region is inside the projection. Figure 8 serves to clarify this concept.
   The field of view of the spectrograph is adjusted to represent SPICE's actual rectangular field of view of 11 arcmin width and 16 arcmin height (Caldwell 2014). The percentage of observed source regions is calculated, which in return is a measure for the quality of the prediction method.

In the following sections we try different prediction methods for Step 3 of the above numeration and compare the percentage of hit source regions.

3.1. Ballistic mapping only

For the first approach the source regions of the solar wind are predicted only by ballistic back mapping, therefore completely ignoring any magnetic displacement inside the corona. This method would be the easiest way to determine the source regions since it does not need any knowledge about the coronal magnetic structure. For the ballistic back mapping the solar wind speed is

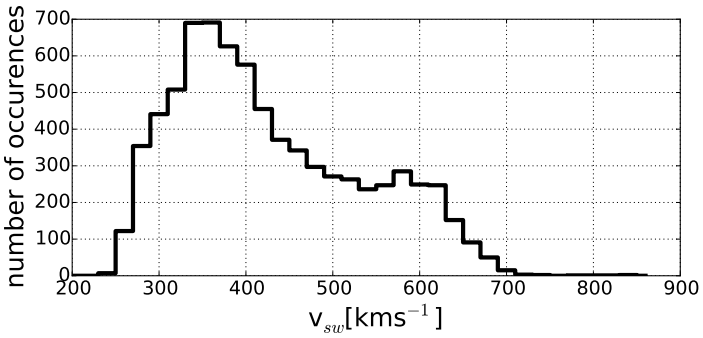

Fig. 7. Solar wind speeds used for this study. The solar wind speeds have been measured by ACE/SWEPAM during CRs 2040 to 2058.

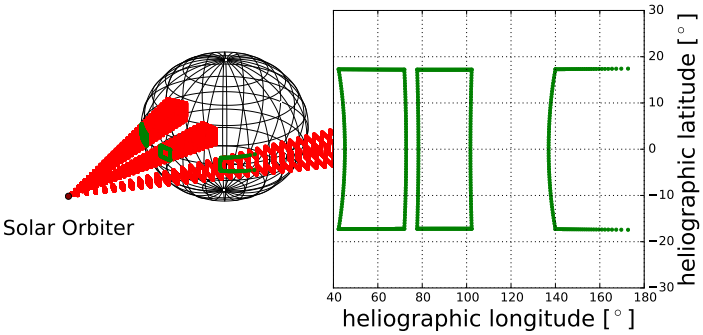

Fig. 8. Projection of a field of view on the Sun. The left panel shows Solar Orbiter (dark red point) in orbit around the Sun (black mesh) with SPICE's rectangular field of view (red) projected onto different regions of the Sun's surface (not to scale). The right panel shows the projection on the Sun's surface in heliographic coordinates. This is the actual projection of SPICE's field of view from 0.3 AU, hence the right panel is to scale.

needed in order to derive $\lambda_{\mathrm{dis}}^{\mathrm{bm}}(d, v_{sw})$ and $t_{ss}(d, v_{sw})$ according to Eqs. 1 and 2. Unfortunately, at the time the spectrograph has to be pointed at the Sun the in situ solar wind speed has not yet been measured. A solution would be to use the solar wind velocities measured during the preceding CR. At solar minimum the solar wind speeds measured during one CR do not differ too much in comparison to the speeds measured in the preceding CR (see Fig. 11).
Using the solar wind speeds from the preceding CR $cr - 1$, λ_{sr} and ϕ_{sr} for CR cr can be calculated. The above described is now applied for each CR with the exception of 2040, because here no preceding rotation is available. With the source regions predicted we check if the spectrograph was actually able to hit them. The percentage of successful hits calculates to:

$$H = \frac{N}{5490} \cdot 100\%. \tag{5}$$

Here N is the number of observed source regions and 5490 is the total number of observations simulated over 18 CRs. Considering only the ballistic mapping we end up with:

$$H = 16.08\% \pm 9.42\%. \tag{6}$$

The error of H is the standard deviation calculated from the individual $H(cr)$ for each CR. Additionally the values for individual CRs $H(cr)$ are displayed in Fig. 9 as blue x. The errorbars shown here stem from the procedure described in Sect. 2.4. This result shows that ballistic back mapping alone is not sufficient for the prediction of the source regions, since more than 80% are missed. Obviously the magnetic displacement can be expected

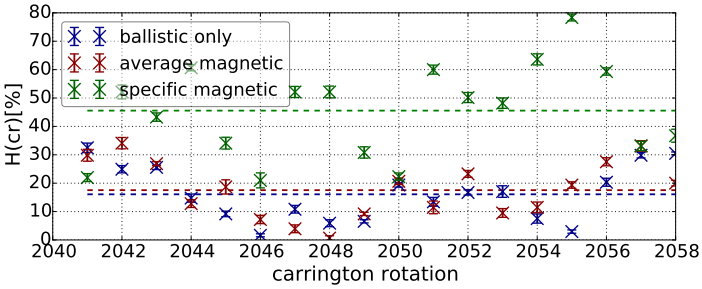

Fig. 9. Percentage of hits $H(cr)$ plotted against the CR. The different colors depict the different methods used. The dashed lines represent the average of $H(cr)$ for each method. The individual error bars stem from the error estimation described in Sect. 2.4.

to have a large influence on the results. There are different ways to include the magnetic displacement which we explore in the next subsections.

3.2. Average magnetic mapping

The simplest way to include the magnetic mapping into the simulation and therefore the prediction of the source regions of the solar wind is to assume an overall average magnetic displacement which substitutes the actual magnetic displacement. This can be done under the assumption that displacement distributions like those shown in Fig. 4 are of a general validity.
For that approach we calculated displacement distributions in a similar way as in Sec. 2.2.1. The results are shown in Fig. 10 We now estimate the percentage of captured source regions, cal-

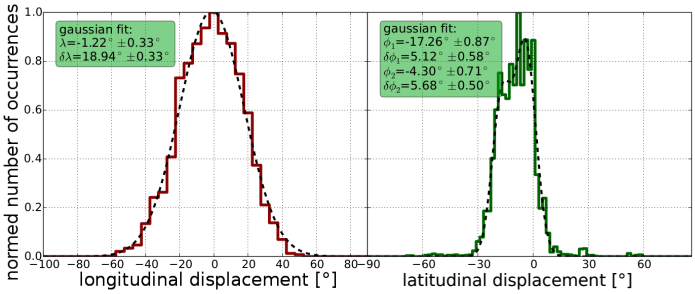

Fig. 10. PFSS induced longitudinal (left) and latitudinal (right) displacement between source surface position and photospheric position similar to Fig. 4. The y axis gives the normed number of occurrences for both plots. The calculation was made for Solar Orbiter's orbit over the course of 19 consecutive CRs, each plot also shows a fit with a simple Gaussian (left) or rather a sum of two Gaussian (right). We note the stronger shift to lower latitudes compared to Fig. 4 due to Solar Orbiter's tilted orbit.

culating the expected source locations for the solar wind using Eq. 3 with $\lambda_{dis}^{pfss} = -1.22°$ and $\phi_{dis}^{pfss} = -4.3°$ taken from Fig. 10 in addition to the ballistic mapping according to Eq. 3. This approach yields the following result:

$$H = 17.76\% \pm 9.76\% \tag{7}$$

The result is only slightly better than the previous one where only the ballistic back mapping has been considered. The results for the individual CRs are shown as red x in Fig. 9. The overall average displacement calculated over many CRs does not sufficiently reflect the actual displacement for an individual rotation. Hence, a more sophisticated approach is required.

3.3. Specific magnetic mapping

In this approach we calculate the exact photospheric sources including ballistic mapping and magnetic mapping for the orbit of CR $cr-1$ and use them for rotation cr. Of course, they are not exactly the same but similar enough for SPICE's field of view to capture a significant portion of them. The expected source locations for rotation cr calculate to:

$$\begin{aligned} \lambda_{esr}(d, v_{sw}, cr) &= \lambda_{sc} + \frac{\omega d}{v_{sw}(cr-1)} + \lambda_{dis}^{pfss}(cr-1) \\ \phi_{esr}(cr) &= \phi_{sc} + \phi_{dis}^{pfss}(cr-1) \end{aligned} \quad . \tag{8}$$

The overall result for this method calculates to:

$$H = 45.56\% \pm 15.77\%. \tag{9}$$

The results for the individual CRs are shown in Fig. 9 as green x. This is a more satisfying result than the two derived before. But if we look at the individual CRs in Fig. 9 there is a notable degree of variation, ranging from 75% of the source regions captured, for example, CR2055, down to only around 30%, for example, CR2050. To understand this variation we compared the mentioned examples with their respective preceding CR which was used to determine $\lambda_{esr}(d, v_{sw}, cr)$ and $\phi_{esr}(cr)$. This is done in Fig. 11. It is evident that the differences between CR

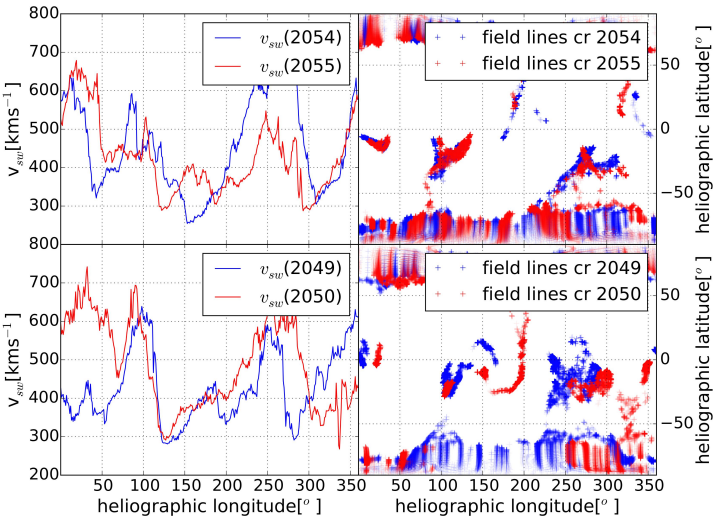

Fig. 11. Comparison between consecutive CRs. The left panels show the solar wind velocity taken from ACE for the respective CRs while the right panels show the PFSS model data of the photospheric foot points of the open magnetic field line. The latter rotations 2055 and 2050 are shown in red, the former rotations 2054 and 2049 are shown in blue. The upper panels show the case for CR 2055, where the predictions produced very good results while the lower panel show the case for rotation 2050, where only very poor results were produced.

2054 and 2055 are rather small, hence the specific deviation method was able to produce such good results. The opposite is true for the rotations 2050 and 2049. Here the differences are considerable. Therefore it is only reasonable that the hit percentage is very low for CR 2050 and high for rotation 2047. From Fig. 11 and Fig. 9 it can be inferred that the correct prediction of the source regions depends critically one the similarity between consecutive CRs. If the similarities are not sufficient, the predictions made become unreliable.
In the case of SPICE constantly imagining the source regions for every step in Solar Orbiter's orbit the method to specifically predict the source regions could be considered a satisfactory method since it leads to many cases where the source regions

are successfully captured. SPICE will also be used for different purposes, therefore it will only image the solar wind's source regions for certain selected points during its orbit. With only a small number of images the risk of not capturing even one source region becomes considerable. This renders the procedure discussed in this chapter rather unfavorable in the end. A different and more reliable method is discussed in the next Sect..

3.4. Leading stripe mapping

Instead of predicting each solar wind source region individually one could point the spectrograph at the sun with or without a certain leading angle while also trying to maximise the covered area on the Sun's surface. Six observations per day can be vertically stacked in order to increase the instruments field of view. This increased field of view has a height of 96 arcmin and completely covers the Sun in terms of latitude. In this section we analyze the feasibility of such an approach. Solar Orbiter's orbit and the observation of solar wind is simulated in the same manner as before. For each point in its orbit SPICE takes an image of the Sun's surface with a fixed leading angle λ_{la}, pointing at

$$\lambda = \lambda_{sc} + \lambda_{la}. \quad (10)$$

With this configuration SPICE is able to capture virtually any source region on the Sun's surface, but not necessarily at the actual solar wind release time. For each CR we calculate the coordinates of the solar wind's source position and for every source coordinate we also determine the solar wind release time t_{ps}. The orbit is then simulated as described above ten times for different leading angles λ_{la} ranging from $-50°$ to $40°$. Due to the rotation of the Sun, source regions enter the projection of the field of view coming from lower longitudes. As soon as a source region is located in the center of SPICE's field of view it counts as observed. For each observed source region the remote observation time t_{obs} is listed. Due to the rotation of the Sun the source region enters the field of view on the left side, that is, at lower longitudes. The field of view then sweeps over the source region until it is no longer covered. A source region stays roughly between 40 and 90 hours inside the field of view, depending on the leading angle. In order to analyze this simulation we calculate the time difference between the release time of the solar wind package t_{ps} and the observation time t_{obs} for every source region:

$$\Delta t = t_{ps} - t_{obs}. \quad (11)$$

The results are shown in Fig. 12. Each panel shows the results for a different leading angle, starting with the upper left panel at $\lambda_{la} = -50°$ and ending with the lower right panel at $\lambda_{la} = 40°$. The histograms are normalized to their respective sum. The y axis therefore gives the probability per bin. The differently colored histograms show source regions with measured solar wind speeds below 350 kms^{-1} , only source regions with speeds above 600 kms^{-1}, and intermediate speeds with 350 kms^{-1} $< v_{sw} <$ 600 kms $^{-1}$. On the x axis Δt is shown. A negative value for Δt means that a particular source region has been observed by SPICE after the solar wind package was released, a positive value means the source region has been observed before the solar wind package departed. The area taking the extent of the field of view into account is marked. As stated above, a source region needs 40 to 90 hours to traverse the field of view. With SPICE's intention to observe a source region during the release of the solar wind, the area between the dashed lines marks the optimal observation time. We call the portion of source regions which are optimally covered Γ_{oc}.

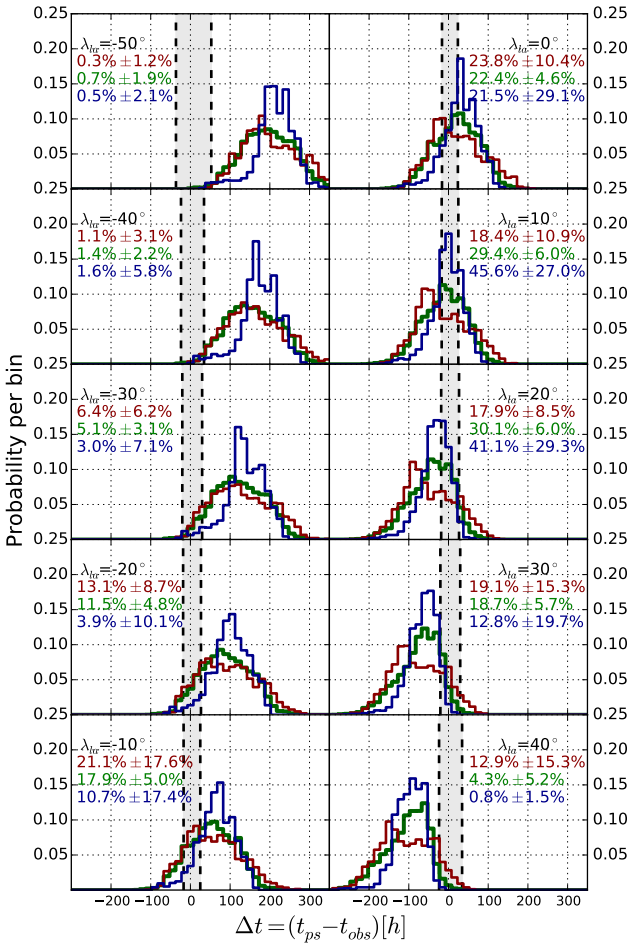

Fig. 12. Results for the leading stripe mapping. The x axis shows the time difference $\Delta t = t_{ps} - t_{obs}$ between the time when a source region is observed by the spectrograph and when it releases its solar wind package. The y axis shows the probability per bin. The red curves show only source regions with a measured solar wind speed below 350 kms^{-1}, the green curves represent intermediate speeds from 350 kms^{-1} to 600 kms^{-1} and the blue curves with speeds above 600 kms^{-1}. Each panel shows the result for a different leading angle. The dashed vertical lines mark the area where a source regions would be observed at the moment of the solar wind's release. The colored numbers show Γ_{oc} in percent with the corresponding errors. The errors are the statistical errors originating from the variation between individual CRs.

If we now analyze the shown distributions of Δt it is evident that it shifts from right to left with increasing leading angle. With a leading angle of $\lambda_{la} = -50°$ the majority of solar wind packages are observed before the release of the solar wind package. Then again, a leading angle of $\lambda_{la} = 30°$ and greater means the observation of nearly all source regions happens after the solar wind is released. We note that the difference between fast and slow solar wind is small. On the one hand the ballistic displacement leads to a systematic separation between the distributions of the fast and slow solar wind, since it depends on the solar wind speed. The magnetic displacement on the other hand does not depend on v_{sw} and therefore leads to a broadening of both distributions and therefore to a distinctive overlap.

Since SPICE's goal is to find the source regions of the slow solar wind we will focus on the red histograms in Fig. 12. The optimal solution would be a leading angle which enables SPICE to observe the solar wind's source region at the moment when the

solar wind is released, that is, when Γ_{oc} becomes maximal. This is the case for a leading angle $\lambda_{la} \approx 0°$, as can be seen in the respective panel in Fig. 12. To examine this in more detail we repeat the simulation for leading angles ranging from -8° to 2°. The results are shown in Table 2. It can be seen that the best results are achieved for leading angles λ_{la} between -6° and -4°. For the study of fast and intermediate solar wind a leading angle of $\lambda_{la} = 10°$ would be optimal.

Table 2. Γ_{oc} for solar wind with speeds < 350 kms^{-1}, as function of the leading angle.

Leading angle[°]	Γ_{oc}[%]
-8	23.6±18.1
-7	24.3±17.4
-6	24.8±16.2
-5	24.7±14.8
-4	24.8±12.4
-3	24.4±11.4
-2	24.4±10.8
-1	24.0±10.0
0	23.8±10.4
1	23.1±12.6

The errors shown in Fig. 12 derive from the variation between the individual CRs. These statistical errors are considerably larger than the ones derived from the method described in Sect. 2.4, which are of the order of 0.5 % and smaller. From that we conclude that the uncertainties from the ballistic and magnetic mapping play only a secondary role in comparison to the statistical error.

4. Comparison with the CSSS model

As stated in Section 2, the CSSS model has been shown to predict solar wind speed nearly twice better than the PFSS model. The details of the CSSS model and the method adopted for the prediction technique can be found in Poduval & Zhao (2014) and Poduval (2016). In order to test if a different input model alters the results of our analysis we repeated the analysis of the former section but using the CSSS model for the calculation of the magnetic mapping. Additionally we adjust the radius of the source surface to 15 $R_\odot$, as this is the case for the CSSS model. Since we have only a smaller subset of CRs computed with the CSSS model we also used the same smaller subset of rotations computed with the PFSS model for the comparison. The results are shown in Fig. 13. The histograms shown here cover the same solar wind speed window as the red histogram in Fig. 12. The differences from Fig. 12 are because of the smaller subset of CRs used. In Fig. 13 we can see that both results show the same behaviour. Although the absolute numbers differ slightly both histograms show that the optimal value for Γ_{oc} is obtained for $\lambda_{\mathbf{la}} = -10°$. This analysis shows that the CSSS results are comparable to those of the well-established PFSS model. Therefore, for the present analysis both the CSSS and PFSS models seem equally applicable.

5. Summary and conclusion

One of the aims of the upcoming Solar Orbiter mission is to directly identify the source regions of solar wind by linking remote and in situ observations. The novelty of Solar Orbiter's instrumentation lies in the capability of measuring solar wind in situ and remotely at the same time and very close to the Sun. The challenge to establish the link is not only to find the spatial displacement between in situ observed solar wind and its source region on the Sun but also to take into account the temporal displacement between these two observations. This means that we need to point the remote-sensing instrument on the right place at the Sun and at the right time. In order to do so the terminal solar wind speed as well as the magnetic configuration inside the corona must be known. Both cannot be known in real time, for example, the terminal solar wind speed cannot be obtained from remote sensing but only by in situ measurements. Thus, a prediction of the solar wind speed which will be measured in situ in the future is needed to point the spectrograph at the right place at present.

In this study we investigated the spatial and temporal displacement between in situ observed solar wind and its source region on the Sun. In addition we tested different methods to predict the optimal pointing of SPICE with respect to source region coverage and temporal displacement. The spatial displacement is found by tracking the solar wind from its source region out to the spacecraft. Above the source surface we applied classic ballistic back mapping, resulting in a ballistic displacement. Inside the corona we applied a PFSS model which yields a magnetic displacement, and a model by Cranmer et al. (2007) from which we derive the coronal escape time.

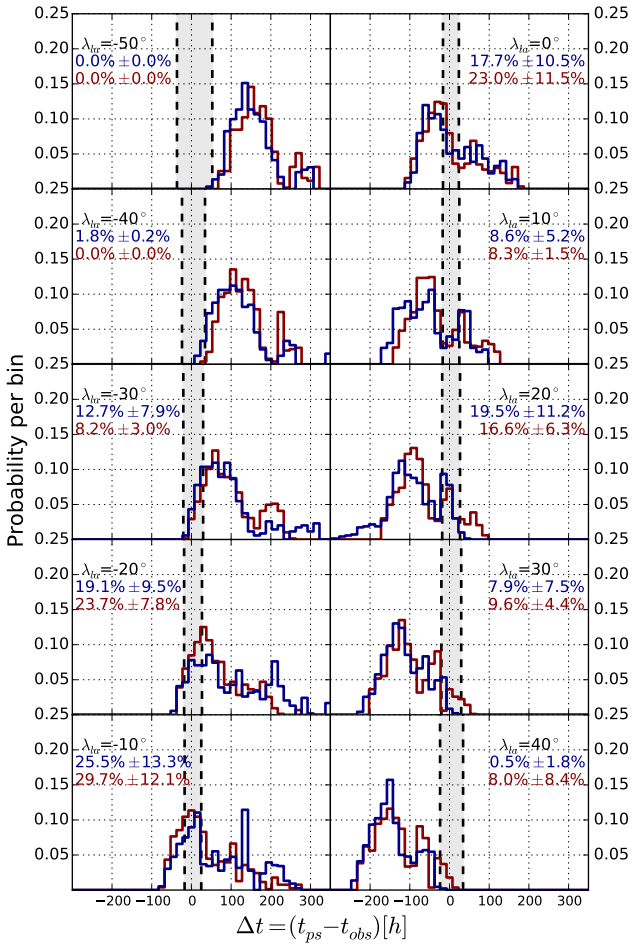

Fig. 13. Comparison of the leading stripe mapping between the PFSS (red histograms) and the CSSS (blue histograms) model. The axes are the same as in Fig. 12. Note that the subset of CRs used for this comparison only includes four rotations. The solar wind speed window covers the range from 0 to 350 km/s. The errors given are the statistical errors originating from the variation between the CRs.

We find that it is important to consider the magnetic mapping in addition to the ballistic mapping for the prediction of the solar wind's source regions. For the prediction of the solar wind's release time, that is, the time when the instrument has to do its observation, the plasma escape time has to be added to the ballistic travel time of the plasma package. For an instrument to track the source regions in real time, a prediction scheme that uses the solar wind speeds and magnetic configuration of the preceding CR yields a probability of 45.56 % ± 15.77 % to observe the source region at the time of the solar wind's release at the photosphere. SPICE will only be able to make one raster per day, that is, SPICE will not be able to track the source regions at all times, but the in-situ instrument (HIS) will measure at all time. To account for this a leading stripe forward mapping was devised, where six snapshots are vertically stacked to form a stripe which covers the whole Sun in latitude. Virtually any source region will be detected eventually, but typically not at the time of the plasma release at the Sun. For each source region covered by the leading stripe the time difference between remote observation and solar wind release can be calculated. To optimize the number of observations done at the right time the leading angle of the stripe can be varied. We tested this for various angles ranging from -50° to 40° and three different solar wind speed regimes. This results in an optimal leading angle ≈-6° for the study of slow solar wind (250 kms^{-1}<v_{sw}<350 kms^{-1}), ≈20° for intermediate (350 kms^{-1}<v_{sw}<600 kms^{-1}) and ≈10° for fast solar wind (600 kms^{-1}<v_{sw}<900 kms^{-1}).
Additionally we repeated the leading stripe method while using CSSS maps for the magnetic mapping in order to compare the results. The comparison did not lead to different results, hence we concluded that the PFSS model is sufficient for the presented analysis. In particular these small leading angles and the corresponding almost optimal line of sights are advantageous for the quality of the SPICE measurements. Although the focus of our study was on the upcoming Solar Orbiter mission and the SPectral Imaging of the Coronal Environment instrument, the methods described are generally applicable.

Acknowledgements. This work uses magnetograms obtained from the MDI instrument in board the SOHO spacecraft, SOHO is a project of international cooperation between ESA and NASA. Additionally this work uses SOLIS data obtained by the NSO Integrated Synoptic Program (NISP), managed by the National Solar Observatory, which is operated by the Association of Universities for Research in Astronomy (AURA), Inc. under a cooperative agreement with the National Science Foundation.
The authors would like to thank Dr Bala Poduval for her valuable support with the CSSS model and the computations contributed to this work.
Rfws acknowledges constructive discussions with the Solar Orbiter SPICE steering committee and the Solar Orbiter Science Working Team and the German Space Agency,DLR for grant 50OT1202. LB was supported by DLR grant 50OC1501.

References

Altschuler, M. D. & Newkirk, G. 1969, Sol. Phys., 9, 131
Bochsler, P. 2000, Reviews of Geophysics, 38, 247
Caldwell, M. 2014, SPICE Instrument User Manual
Cranmer, S. R., van Ballegooijen, A. A., & Edgar, R. J. 2007, ApJS, 171, 520
Fisk, L. A. 2003, Journal of Geophysical Research (Space Physics), 108, 1157
Fludra, A., Griffin, D., Caldwell, M., et al. 2013, in Proc. SPIE, Vol. 8862, Solar Physics and Space Weather Instrumentation V, 88620F
Geiss, J., Gloeckler, G., & von Steiger, R. 1995, Space Sci. Rev., 72, 49
Goel, A. & Choudhuri, A. R. 2009, Research in Astronomy and Astrophysics, 9, 115
Hassler, D. M., Deforest, C., & Spice Team. 2011, AGU Fall Meeting Abstracts
Koskela, J. S., Virtanen, I. I., & Mursula, K. 2015, AGU Fall Meeting Abstracts
Krieger, A. S., Timothy, A. F., & Roelof, E. C. 1973, Sol. Phys., 29, 505
Landi, E., Gruesbeck, J. R., Lepri, S. T., & Zurbuchen, T. H. 2012, ApJ, 750, 159
Liu, Y. & Norton, A. 2001, Mdi measurement errors: the magnetic perspective, SOI technical note, Tech. rep., Technical report, Stanford University
Neugebauer, M., Forsyth, R. J., Galvin, A. B., et al. 1998, J. Geophys. Res., 103, 14587
Nolte, J. T. & Roelof, E. C. 1973, Sol. Phys., 33, 241
Poduval, B. 2016, ApJ, 827, L6
Poduval, B. & Zhao, X. P. 2014, ApJ, 782, L22
Rappazzo, A. F., Matthaeus, W. H., Ruffolo, D., Servidio, S., & Velli, M. 2012, ApJ, 758, L14
Royal Observatory of Belgium, B. 2016, `http://sidc.be/silso/home`
Schatten, K. H., Wilcox, J. M., & Ness, N. F. 1969, Sol. Phys., 6, 442
Scherrer, P. H., Bogart, R. S., Bush, R. I., et al. 1995, Sol. Phys., 162, 129
Schwenn, R., Mohlhauser, K. H., & Rosenbauer, H. 1981, in Solar Wind 4, ed. H. Rosenbauer, 118

-

7 ENERGETIC NEUTRAL ATOMS

In the former chapters the topic was the quiescent solar wind and its source regions. As discussed, the solar wind is generally synonymous with highly charged particles. Despite that being the case, one could say that there is yet another, a hidden charge state in the heliosphere, namely the uncharged or neutral state, as already hinted in section 2.1.1. There is more than one population of neutral atoms in interplanetary space and some of them even have an origin that lies outside the heliosphere. Others stem from various sources inside the heliosphere like the Sun itself and some of the planets. Direct observations of energetic neutral atoms are rare, partly due to the lack of dedicated instruments. But there are numerous indirect observations where neutral atoms are ionized prior to their measurement and are then detected by ion detectors.

7.1 NEUTRAL ATOMS IN THE HELIOSPHERE

A rather prominent example for neutral atoms in the heliosphere are the so called pick-up ions. Although they are ions, these particles are a good indicator for the existence of neutrals in interplanetary space. Neutral atoms inside the heliosphere have a certain chance to become ionized, either by photoionization due to solar ultra violet radiation of by charge exchange with solar wind ions. As soon as an atom becomes ionized it is affected by the magnetic field embedded in the solar wind and is carried outwards while gyrating around the magnetic field lines. Because of this process these particles are called pick-up ions. They are frequently measured by solar wind detectors and are direct evidence for the existence of a neutral atom population in interplanetary space. Pick-up ions are divided into two groups, interstellar and inner-source pick up ions. Both can be distinguished from solar wind ions by their charge state, as they tend to be singly charged. Additionally, interstellar pick-up ions have a velocity distribution different from the solar wind, with the velocities ranging from zero v_p to two times v_p, see Drews et al. (2015), or Kallenbach et al. (2000). These particles originate from the local interstellar medium and enter the heliosphere through the heliopause, as they are not affected by magnetic fields. When they reach the inner heliosphere they potentially end up as pick-up ions, see for example Möbius et al. (1985) for more information.
Inner-source pick up ions differ from interstellar pick-up ions in that they mimic the velocity distribution of the solar wind, see Geiss et al. (1996). Their origin cannot be fully explained by now, but the most likeliest scenario is that these particles are former solar wind which has been neutralized on its way between the Sun and the observer. After that the particles have been ionized again, but without reaching their former high charge state.
While pick-up ions are an excellent example for an indirect observation of neutral atoms, there are also direct measurements. The Interstellar Boundary EXplorer (IBEX), see McComas et al. (2004), is able to measure these neutral atoms directly. IBEX measured the famous "ribbon", a signature of neutral atoms which is believed to be a finger print of the heliopause. The neutral particles measured by

IBEX are believed to be pick-up ions that have been accelerated, deflected and neutralized at the termination shock. As neutral particles they then travel back again into the heliosphere were they are then observed. Interestingly, when the Voyager spacecraft crossed the termination shock the measurements did not match the expectations which were based on the process described above, see Senanayake et al. (2015). The scenario for the origin of these neutral particles might still be valid, but further studies are needed.

Another source for neutral particles in the heliosphere could be the Sun itself. An indication for that are Lyman-α measurements in the corona. At a first glance it is unexpected to find uncharged particles here since the corona is too hot to leave atoms non-ionized. Nevertheless, the first measurements were made by Gabriel (1971), who attributed the observed Lyman-α lines to photo-excitation of residual coronal hydrogen. The lines were observed for heights up to $\sim 1 R_\odot$ above the photosphere. Hence it is in the bounds of possibility that neutral hydrogen can escape into the heliosphere.

An indirect observation of neutral atoms coming from the Sun was made by Mewaldt et al. (2009). Although the measured particles were protons, Mewaldt et al. (2009) concluded that they must have been neutral atoms and have only been ionized shortly prior to the measurement. In this case, energetic neutral atoms were produced in a flare event on the Sun, where charge exchange reactions produced neutral hydrogen from protons accelerated in the flare region. The observation was made by the Low Energy Telescope (LET), see Mewaldt et al. (2007), and the High Energy Telescope (HET), see von Rosenvinge et al. (2007), on the Stereo B spacecraft. The assumption that these particles traveled as neutral atoms through the heliosphere was based on the fact that the heliospheric magnetic field would not have allowed charged particles from the flare to arrive at the spacecraft at all. Another instrument that has measured neutral particles in the heliosphere is for example the Ulysses interstellar neutral GAS experiment (GAS), see Witte et al. (1992).

Following the above, it can be seen that there are several sources for neutral atoms in the heliosphere, but so far direct observation are rare. The energy of these particles ranges from a few tens of eV for interstellar atoms to some MeV in case of the energetic neutral atoms reported by Mewaldt et al. (2009). An example for two planned instruments that will be able to directly measure neutral atoms is the STart from a ROtating Field mass spectrOmeter (STROFIO) and the Emitted Low Energy Neutral Atoms (ELENA) instrument on the BepiColombo spacecraft. Both instruments are part of the Search for Exospheric Refilling and Emitted Natural Abundances (SERENA) instrument suite, see Orsini et al. (2010) for more information. Both instruments together cover the energy range from a fraction of an eV to several keV. The neutral particles these instruments are supposed to measure come from the local environment around planet Mercury. Here interactions with the solar wind are believed to release neutral atoms, making Mercury another source for neutral particles in the heliosphere.

7.2 THE SOLAR WIND CALIBRATION FACILITY

These new instruments, like all particle detectors, need to be calibrated in order to later understand the detector response. There are many accelerators that pro-

duce charged particle beams which can be used to calibrate ion and electron detectors, but there are only few possibilities to calibrate a neutral atom detector. Additionally, many accelerators are not intentionally built for detector calibration, but for example being used in medical treatment. Specialized calibration facilities are scarce. To fill this void the University of Kiel is establishing a dedicated solar wind laboratory in which all constituents of the solar wind can be created, including accelerated neutral atoms, and be used for detector calibration. Figure 30 shows a Computer Assisted Drawing (CAD) of the solar wind laboratory.

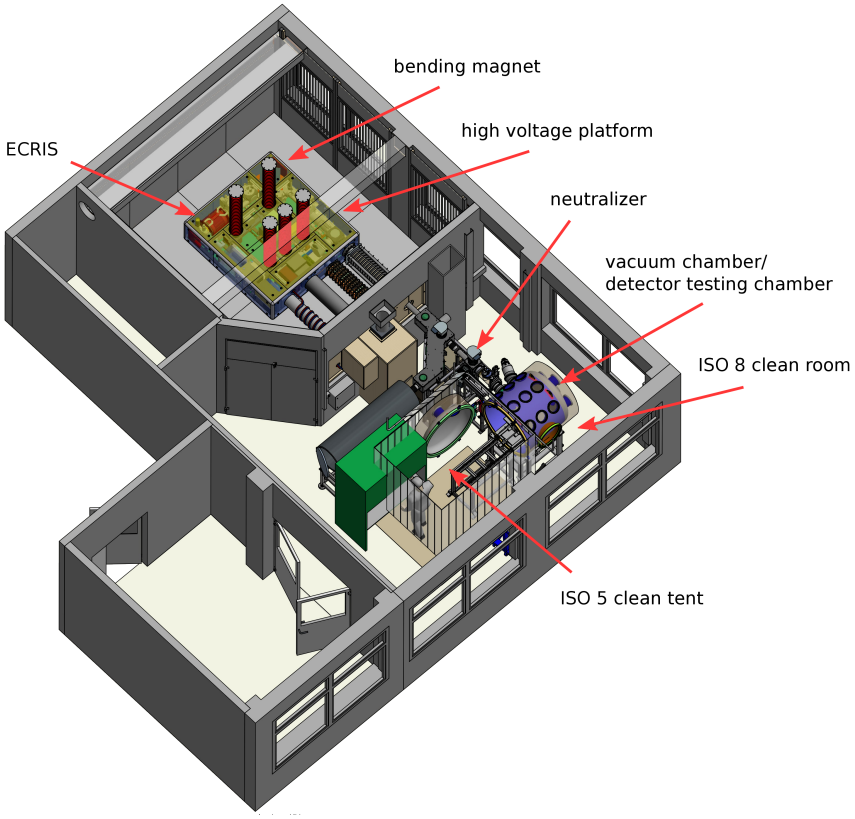

Figure 30: CAD of the solar wind lab. On the left side of the isometric drawing an ion source can be seen on a high voltage platform. On the right side a big vacuum chamber is displayed. Detectors can be placed inside this chamber for calibration purposes. CAD from Kolbe (2017).

Here the key elements of the laboratory are marked. The Electron Cyclotron Resonance Ion Source (ECRIS) is the heart of the facility and can create ions with very high charges states, e.g. Ar^{12+}. Once accelerated, the ion beam is split up by a bending magnet according to the ions mass per charge ratios. After that selected the ions pass through a second acceleration range. Finally, the ions can be neutralized by a gas or foil target in order to create a beam of energetic neutral atoms. Not marked in figure 30 is an electron source which can create a beam of accelerated electrons. Thereby this facility is able to recreate a majority of the particle populations found in the heliosphere. The achievable particle energy ranges from $\sim$5 keV/q up to 470 keV/q, with q being the charge of the original ion in case of a neutral beam.
Such a calibration facility needs detectors of its own to measure the created par-

ticle fluxes. The problem that arises with neutral atoms is that they are more difficult to measure than charged particles. There is a wide range of detector systems available for the measurement of charged particles, such as Multi Channel Plates (MCPs) (Henkel et al., 1978), Solid State Detector (SSD) or Faraday cups (FCs) and these can in principle be used for the detection of neutral atoms as well. Most particle-counting detectors such as MCPs and SSDs have problems with particle fluxes $\geq 10^6\,\mathrm{s}^{-1}$. For such intense fluxes these detectors get saturated and therefore count rates higher than the above mentioned cannot be measured correctly. Even worse, such fluxes can potentially damage the detector. Another problem which applies especially to SSDs, is the necessity of a dead layer in front of the entrance window of the detector. Particles with insufficient kinetic energy, especially heavy atoms, are unable to penetrate this dead layer and therefore cannot be detected. In the solar wind laboratory FCs are used as detectors, which in general provide many advantages: They combine high reliability with low monetary effort. Especially compared to SSDs and MCPs they can withstand higher thermal loads and they do not have a lower limit for the primary particle energy as long as it is able to produce secondary electrons. This is the case because a FC cannot directly detect neutral particles since it measures the impinging current which is zero for a beam of neutral atoms. Nevertheless it can indirectly observe neutrals by measuring the current of secondary electrons which are emitted by the impact of primary particles.

7.3 SECONDARY ELECTRON EMISSION

In order to calibrate the FC for the measurement of uncharged atoms, the Secondary Electron Emission (SEE) must be known. In general, the SEE for a primary particle of a given particle species depends on its kinetic energy and on its ionization potential. It also depends on the absorber material, i.e. the material the FC is made of. Two processes induce the emission of electrons, the so called kinetic emission and the potential emission, see Wang et al. (2007).
Since neutral particles carry no charge, potential emission does not play a role for the SEE induced by neutral atoms and only the kinetic emission should matter. Since all used FCs are made of aluminum we can make the assumption that the SEE only depends on the kinetic energy and supposedly also on the element of the primary neutral atoms. Therefore, the correlation between the primary kinetic energy and the SEE for every element of interest is needed. Once this is obtained by experiment, we can use the FC as a detector for the determination of absolute fluxes of neutral atoms.
In general, the SEE γ, is defined as:

$$\gamma = \frac{F_{se}}{F_n} \tag{38}$$

Here F_{se} is the flux of Secondary Electrons (SEs) leaving the FC and F_n is the flux of primary neutral atoms. The flux of electrons can be easily obtained by

$$F_{se} = \frac{I_{se}}{eA} \tag{39}$$

where I_{se} is the measured current of SEs induced by neutral atoms, e is the unit charge and A is the collecting area.

7.4 EXPERIMENTAL SETUP

The energetic neutral particles are created from accelerated ions. The ions originate from an ECRIS, which can produce various ion species of different charge states. The ECRIS is custom made, for more information about it see Stalder (2008). These ions can be accelerated with up to 20 kV/q. Downstream of the ECRIS the ion beam is separated by a bending magnet (framed black in figure 31) for its mass per charge ratio. Thus, behind the bending magnet one can obtain a monoenergetic beam of ions of one particular charge state with an energy uncertainty of some eV. The overall setup is shown in figure 31. Here the bending magnet and parts of the downstream beamline is displayed. To convert the ions into a beam of neutral

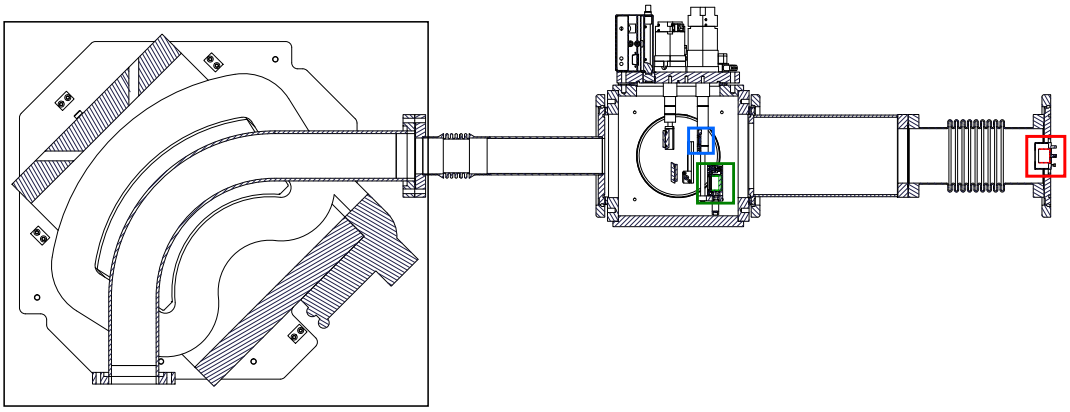

Figure 31: The beamline downstream of the bending magnet. Not shown is the ion source. The bending magnet is framed in black. Framed in blue is the carbon foil, which is utilized to neutralize the ions. The FC to be calibrated is positioned at the end of the beam line, roughly 60 cm behind the foil, framed in red. A second FC, framed in green, can be moved directly behind the foil, closer than 1 cm distance. CAD from Kolbe (2017).

atoms a very thin carbon foil (framed blue in figure 31) can be inserted into the beam line. In figure 32 the mounting of the carbon foil is shown. The ions pass

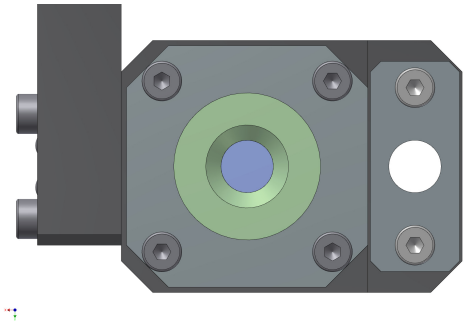

Figure 32: CAD of the carbon foil (blue) with its mounting. The white opening right to the foil serves as a reference-aperture. As the foil is mounted on a fine nickel grid with a transmissivity of 81%, this grid is also present (but not illustrated) in the reference-aperture to ensure identical transmissivity (besides the influence of the foil). Drawing from Kolbe (2017).

through the foil and undergo interactions which modify the charge state. Inside the foil the initial charge state of the ions is lost and set to an equilibrium charge state. Behind the foil the ions are neutralized by electrons tunneling from the foil to the ion, as described in Kallenbach et al. (1993). The carbon foil was purchased from Lebow Company Lebow Company (2013). The foil is mounted on a nickel-grid with a geometrical transmissivity of 81%. Next to the foil there is an aperture with a blank nickel grid of the same geometric transmissivity. This serves as a reference-opening. For more information about the neutralization process and an alternative gas neutralizer see Peleikis (2011).
At the end of the beam line the FC for the measurement of the neutral atoms is installed (framed red in figure 31). A sketch of the FC is shown in figure 33. All

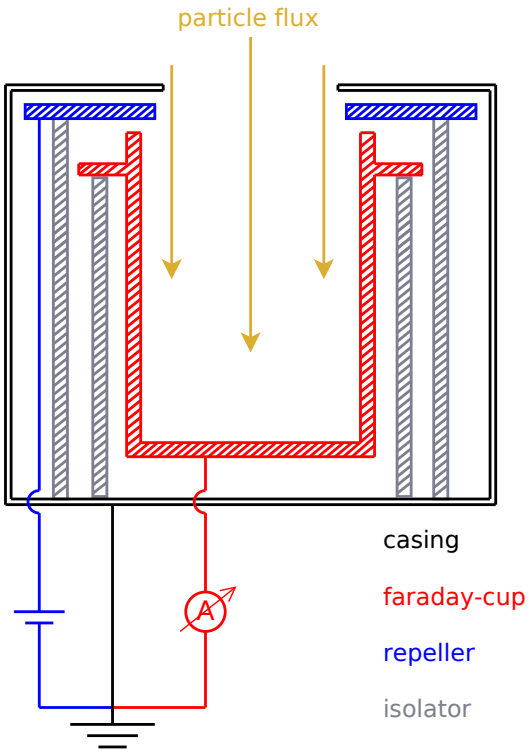

Figure 33: Schematic sketch of the Faraday cup. The current induced by incoming charged particles is measured by an pico-amperemeter. The voltage of the repeller can be adjusted from -150 V to 150 V

current in and out of the FC is measured by a connected pico amperemeter, as shown in figure 33. That means that incoming ions and escaping SEs are measured, depending on the status of an electron repeller in front of the entrance of the FC. It can prevent SEs from escaping from the FC or forces all SEs to leave the FC, depending on the applied voltage, which can be biased from 150 V to -150 V.

7.5 MEASUREMENT PRINCIPLE

As described in section 7.3, the flux of neutral atoms F_n needs to be known for the calibration of the FC. In our investigation we assume that the flux of neutral atoms

behind the foil equals the flux of ions that passes through the reference-aperture in the foil mounting (compare figure 32), assuming a 100% neutralization:

$$F_n = \alpha(E_{kin})F_I \tag{40}$$

F_I is the flux of Ions passing through the reference aperture. $\alpha(E_{kin})$ is a dimensionless parameter, depending on the kinetic energy E_{kin} of the particles, which accounts for scattering caused by the foil. It can be geometrically specified by equations 41 to 43.

$$\alpha = \frac{\text{Flux}_{\text{reduced}}}{\text{Flux}_{\text{all}}} \tag{41}$$

$$\text{Flux}_{\text{all}} = \int_{-\pi}^{\pi}\int_{-\pi}^{\pi} \mathrm{d}\vartheta\,\mathrm{d}\varphi f_E(\vartheta,\varphi), \tag{42}$$

$$\text{Flux}_{\text{reduced}} = \int_{-\varphi_{FC}}^{\varphi_{FC}}\int_{-\vartheta_{FC}}^{\vartheta_{FC}} \mathrm{d}\vartheta\,\mathrm{d}\varphi f_E(\vartheta,\varphi). \tag{43}$$

The directions of the scattered velocity vectors are distributed on a hemisphere given by the coordinates φ and ϑ, where $f_E(\vartheta,\varphi)$ is the distribution function, which depends on the kinetic energy. Other modifications of the beam by the foil are not covered by $\alpha(E_{kin})$. It will be discussed later in this section. The assumption shown in equation 40 is justified by two aspects: The carbon foil does not change the intensity of the particle beam and, below a certain kinetic energy, only neutral atoms emerge from the foil, as discussed by Gonin et al. (1994).
The first aspect is intuitively clear. Above a kinetic energy of some keV all particles can pass through the foil. This can be simulated with TRIM (Ziegler (2007)).
The second aspect was experimentally verified. For that we measured the ion current while relocating the foil into the beam line. In our experiments we observed that for sufficiently low kinetic energies (but still capable of penetrating the foil) only neutral atoms emerge from the foil.
As described by Kallenbach et al. (1993), the reason for the neutralization by the passage through the foil lies in different physical processes. One of theses processes is the tunneling of electrons from the solid to the projectile. While the initial charge state of the ion is lost after the first few atomic layers, the ion is neutralized by a tunnel-current of electrons, which tunnel through the potential barrier between the solid and the projectile. This process becomes more efficient for lower ion velocities, since the interaction time between ion and solid then increases. Therefore, for low kinetic energies, all ions are neutralized.
This was experimentally observed for kinetic energies of the primary particles up to 60 keV. Figure 34 shows two example measurement for a beam of nitrogen ions with the FC. In the first case the nitrogen ions have a kinetic energy of 54 keV and in the second case of 76 keV. The electron repeller is biased to a negative voltage. Hence, only ions contribute to the current measurement as SEs are suppressed. During the current measurement, the foil is driven into the beamline. The measurement with nitrogen ions at 54 keV does not show any measurable current with the foil inside the beam line. In case of 76 keV nitrogen ions a current could be measured while the foil was inside the beamline. It should be noted that the current drops to zero for both cases for a short amount of time because here the mounting of the foil blocks the beam completely. From this measurement it can be inferred

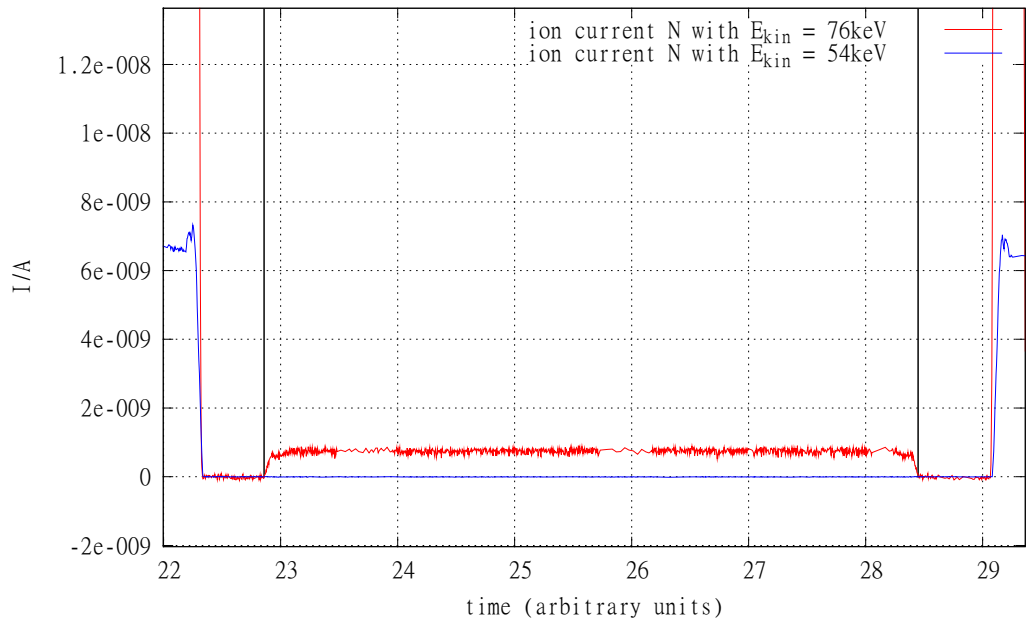

Figure 34: Continuous ion current measurement of nitrogen ions with 54 keV (blue) and 76 keV (red) with the carbon foil driving through the beam. The two black bars mark the time when the foil is inside the beam line. The current of the 54 keV N-ions drops to zero because only neutral nitrogen emerges from the foil. In case of 76 keV N-ions a mixed beam of neutrals and ions emerges from the foil and the FC collects the primary charges.

that for kinetic energies below 60 keV no ions but only neutral atoms can emerge from the carbon foil. At higher energies a fraction of the emerging particles carries a charge. Therefore, we limit our investigations to energies below 60 keV.
In order to determine the scattering-parameter $\alpha(E_{kin})$ from equation 40 we use a second FC (framed green in figure 31), which measures the current directly behind the foil and compare these measurements with the measurements made by a FC further downstream of the foil (framed red in figure 31). In principle, if this FC could be used for the determination of the SEE one would not need to determine $\alpha(E_{kin})$. But as stated above, for the detection of neutral atoms the repeller has to be on a positive potential. Close behind the carbon foil, a positively biased repeller would inevitably channel SE from the foil into the FC, thereby falsifying the measurement of the neutral atoms.
The parameter α gives the ratio of flux which reaches the red framed FC (see figure 31) after the beam has been scattered by the carbon foil. The geometrically motivated equation 41 can not be utilized in the present case, since $f_E(\varphi, \vartheta)$ is unknown. Instead we determine $\alpha(E_{kin})$ from two combined current measurements.

$$\alpha(E_{kin}) = \frac{I_{far}}{I_{close}} \tag{44}$$

Equation 44 shows that $\alpha(E_{kin})$ is just the ratio between the ion current measured far behind the foil (I_{far}) and close behind the foil (I_{close}). Figure 35 shows the measured $\alpha(E_{kin})$ as a function of the kinetic energy for oxygen and nitrogen and compares it with simulated values for $\alpha(E_{kin})$. As one can see the measured values

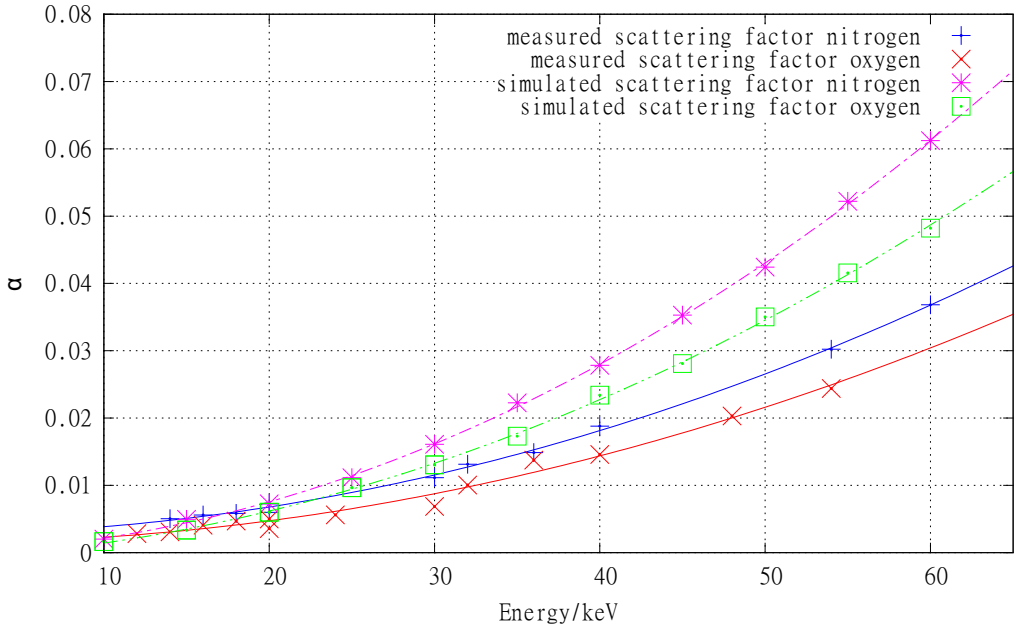

Figure 35: Scattering, $\alpha(E_{kin})$, see equation 44, of the carbon foil for different kinetic energies for primary oxygen and nitrogen, as derived from equation 44. The solid red and blue curves are measured, the dashed curves are simulated with TRIM.

for $\alpha(E_{kin})$ differ from the simulated ones. Unfortunately it is not possible at this point to figure out the reason fo this discrepancy, since the simulation software TRIM is basically a black box. Hence, for our following consideration we will rely upon the measured values. Table 5 shows the fit parameters for the fits for the measured values shown in figure 35. The fit functions are second order polynomials of the form

element	$d/(\text{keV})^{-2}$	$e/(\text{kev})^{-1}$	f
oxygen	$7.989 \cdot 10^{-6}$	$3.021 \cdot 10^{-6}$	$1.48 \cdot 10^{-3}$
nitrogen	$9.14 \cdot 10^{-6}$	$1.904 \cdot 10^{-6}$	$2.75 \cdot 10^{-3}$

Table 5: Parameters for the fit-functions of the measured values shown in figure 35

$$\alpha_{fit}(E_{kin}) = dE_{kin}^2 + eE_{kin} + f. \tag{45}$$

With these foregoing considerations we can deduce the SEE-coefficient γ from two current measurements made with the FC far behind the foil. At first we measure the current of ions I_I through the reference-aperture with a negatively biased electron-repeller. Therefore, only the current of the ions contributes to the measurement. Secondly we measure the current of SEs I_{se} after the beam passed through the foil with a positively biased electron-repeller. That way only the SEs induced by the neutral atoms contribute to the current measurement if the kinetic energy of the primary particles is low enough. Using equation 38-44 one easily sees that

$$\gamma = \frac{F_{se}}{F_n} = \frac{I_{se}}{eF_n} = \frac{I_{se}}{e\alpha(E_{kin})I_I}. \tag{46}$$

7.6 MEASUREMENT

Following the above described principle, the measurements for determining the SEE-coefficient γ were performed for oxygen and nitrogen for initial kinetic energies ranging from 10 keV to 60 keV. Figure 36 shows the results. Here γ is shown as a function of the initial kinetic energy. It should be noted that the initial energy of the particles is decreased when they pass through the foil since the passage through the foil is accompanied by an energy-loss. This energy-loss as well as the error-bars for the energy-axis were derived from TRIM-simulations. Nevertheless γ is plotted as a function of the initial energy, since it is known to the experimenter, on the contrary to the decreased residual energy after the passing through the foil. The blue curve, which is the fit for nitrogen, corresponds to lower values of γ than

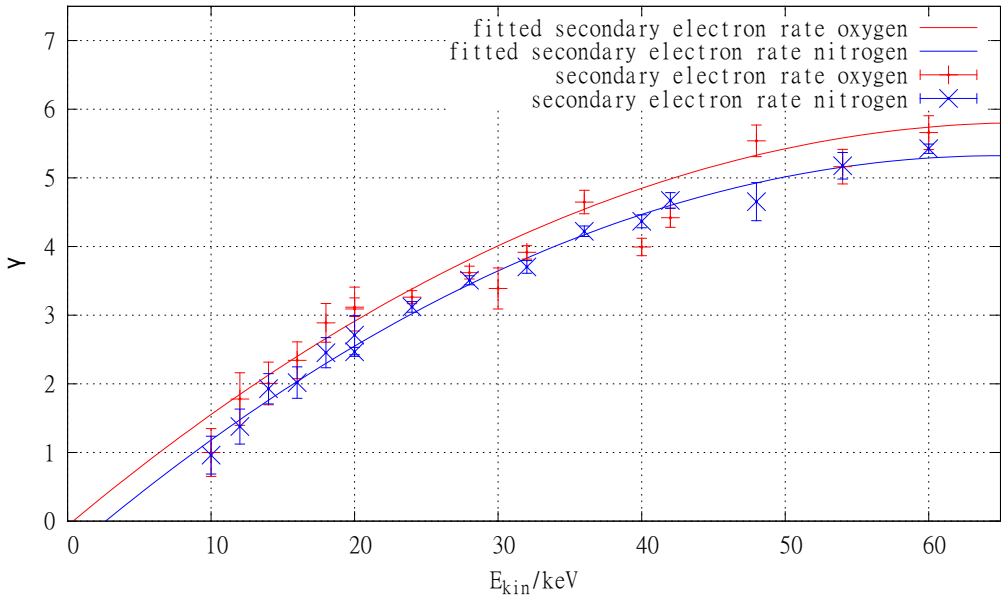

Figure 36: The measured SEE coefficient γ for neutral oxygen and nitrogen, shown as a function of the initial kinetic energy.

the red curve. That is because nitrogen and oxygen differ in mass, which leads to a higher SEE for oxygen. This is for example discussed by Beuhler and Friedman (1977). The SEE-coefficient γ is proportional to $\frac{dE}{dx}$, the energy-loss of the projectile, which is proportional to its atomic number.
The fitted curves are second order polynomials of the form

$$\gamma_{fit}(E_{kin}) = aE_{kin}^2 + bE_{kin} + c \tag{47}$$

There is no physical motivation for choosing these fit-functions, since the goal is to calibrate a FC for the measurement of neutral atoms. The parameters for oxygen and nitrogen are shown in table 6.

7.7 DISCUSSION OF THE CALIBRATION

With this calibration the FC becomes a reliable and robust measurement device for high-intensity neutral atom fluxes. It has virtually no upper limit regarding the

element	$a/(\mathrm{keV})^{-2}$	$b/(\mathrm{kev})^{-1}$	c
oxygen	$-1.305 \cdot 10^{-3}$	0.1751	$-6.685 \cdot 10^{-2}$
nitrogen	$-1.368 \cdot 10^{-3}$	0.1779	-0.4613

Table 6: Parameters for the fit-functions shown in figure 36

particle flux while the lower limit is given by the sensitivity of the connected amperemeter. This makes it superior to SSDs, MCPs or comparable detectors regarding the high particle fluxes. Of course the method presented here only lays the foundation for future calibrations, since only oxygen and nitrogen have been calibrated for now. As soon as the solar wind laboratory has been completed, a wide range of elements can be ionized, accelerated and subsequently neutralized. The described calibration must then be repeated for the elements of interest.

8 CONCLUSION

The Sun and the heliosphere it creates have been subject to spacecraft based observations for around 50 years. Despite considerable advancements in this field of research there are still many particle populations inside interplanetary space with unknown origin or characteristics. Two of them, the so called slow solar wind and energetic neutral atoms are topic of this work. Regarding the slow solar wind it has been observed for a long time and its parameters are well characterized. Based upon these parameters we already have a very good idea where the plasma that makes up the slow solar wind most likely forms in the corona, namely in regions that are filled with magnetic field line loops. The thing that is missing from our understanding is the physical mechanism that releases the plasma from these closed field line structures so that it can contribute to the solar wind. Today, combining in-situ measurements of solar wind parameters with models of the coronal magnetic field can help us on the one hand to understand possible release mechanisms and on the other hand to narrow down the search for where on the Sun these release mechanisms take place. Future mission like Solar Orbiter will further investigate the slow solar wind's origin and hopefully find the missing link between slow solar wind plasma in the heliosphere and magnetic structures in the corona. Regarding the energetic neutral atoms in the heliosphere our current knowledge is far less advanced. While there are some instruments that have directly measured interplanetary neutral atoms the availability of data is poor compared to the slow solar wind. Here we rely on future missions to establish a profound comprehension of these particles.
In this work we started in the heliosphere with the observation of the solar wind and traveled with the observed particles from the spacecraft back to Sun in search of their origin. From there on we devised new measurement strategies for new instruments to better pinpoint the sources of the slow solar wind. And lastly we took another step back and calibrated a neutral particle detector which serves in a facility that emulates the solar wind in order to calibrate new spacecraft based instruments. In a way, this was a backward journey from the calibration of a detector, to the development of a measurement scheme and finally ending with the actual measurement.

8.1 COMBINING IN-SITU DATA AND A CORONAL MAGNETIC FIELD MODEL

For the investigation of the slow solar wind's source regions we combined observational data with a model of the coronal magnetic field, the Potential Field Source Surface (PFSS) model. The PFSS model assumes that at a given distance to the Sun at the so called source surface, usually at $2.5\,R_\odot$, only open radial field lines remain. With that we were able to determine the photospheric source of in-situ measured solar wind. The current leading hypotheses regarding the origin of the slow solar wind predict its source regions either at the border of coronal holes or in a web-like structure of separatrices, called the S-web, which globally connects all open

field lines regions in the corona. The mechanism which is speculated to release the slow solar wind plasma from closed field line regions is magnetic reconnection between open and closed magnetic field lines. Naturally, this can only occur at regions where open and closed field lines are in close proximity. Due to the limitations of the PFSS model we are not able to confirm something like the S-web, but we did find that the solar wind's source location in the corona with respect to the coronal hole border determines the solar wind type. This was expected, as comparable studies led to similar results. Additionally, we were also able to show that the shape of the magnetic field lines, which the plasma has to follow, plays a decisive role. Field lines that bend away from the coronal hole boundary are correlated with fast solar wind, while only open field lines that follow the curvature of adjacent closed field lines can be correlated with slow solar wind. With that our work strongly supports the idea that magnetic reconnection releases the slow solar wind plasma, because only open field lines that follow the shape of the closed loops can reconnect with them over the whole range between photosphere and source surface. Our findings are in agreement with studies made by Pinto et al. (2016), who used magneto-hydrodynamical simulations and likewise reported that the bending of the field lines determines the solar wind type.

8.2 DEVISING A MEASUREMENT SCHEME FOR NEW INSTRUMENTS

From an observational point of view a problem that remains is that most measurements have been made by spacecraft far away from the Sun. Additionally not all spacecraft carry remote sensing instruments together with in-situ detectors. Consequently, a spacecraft which carries both types of instrumentation is needed, that will also approach the Sun as close as possible. This gap in our current observation of the solar wind will be filled by Solar Orbiter, which is currently scheduled to launch in February 2019. On board Solar Orbiter will be a coronal spectrograph, namely the Spectral Imaging of the Coronal Environment (SPICE), and the Solar Wind Analyzer (SWA) suite, which consist of in-situ particle detectors. The search for the origin of the slow solar wind is one of the main scientific goals for Solar Orbiter, however this is not an easy task even with the advantages it brings. The best way to operate SPICE and SWA is to have them both observe the same solar wind package. First remotely with SPICE at the moment of its formation on the Sun and later in-situ with SWA, so that both measurements can be directly linked. The problem here is to know in advance where SPICE has to be pointed at on the Sun, in order to image the solar wind package at the right moment. In order to solve this problem we devised a measurement scheme to optimize the investigation of the coronal sources of the solar wind. This scheme was designed and tested by utilizing a PFSS model and solar wind data from the Advanced Composition Explorer (ACE). With that we simulated the planned orbit of Solar Orbiter and the observation of solar wind. In this simulation, using our measurement scheme, we were able to align SPICE at the Sun in a way that maximizes the portion of source regions that are remotely observed at the optimal point in time so that the desired double observation can be achieved.

8.3 CALIBRATION OF A NEUTRAL PARTICLE DETECTOR

In the last part of this work we focused on a different particle species in the heliosphere. While the solar wind consist in general of highly charged ions, there is yet another, hidden component, namely uncharged particles. This includes the population of energetic neutral atoms in interplanetary space. Although these particles are known to exist in the heliosphere they rarely have been directly observed. This will change in the future, as there are instruments like the STart from a ROtating Field mass spectrOmeter (STROFIO) on the spacecraft BepiColombo in preparation, with the goal to measure neutral atoms. These neutral particle detectors need to be calibrated and for that purpose we are preparing a solar wind laboratory with the capability to produce, amongst others, beams of energetic neutral atoms. Of course, this facility needs a detector of its own. With this in mind we calibrated a Faraday cup (FC) in order to function as a neutral particle detector. Out of the box a FC is not ideal for the measurement of neutral particles. However, it posses other qualities like being very robust in case of high particle fluxes which is why they are used in our calibration facility. Naturally, a FC measures impinging current, which is technically zero for a beam of neutral atoms. Nevertheless, we figured out how to use the emission of secondary electrons in order to detect the primary neutral particles. Because we want to be able to measure total fluxes we needed to determine the energy and element depending secondary electron emission coefficient γ. Subsequently we devised a measurement principle for the determination of γ based on the existing laboratory equipment and exemplarily determined γ for oxygen and nitrogen.

8.4 SUMMARY AND OUTLOOK

With this work we were able to corroborate the current idea that the source regions for the slow solar wind can be found at the borders of coronal holes. Furthermore, our findings strongly support the concept of magnetic reconnection being one of the drivers behind the release of slow solar wind plasma from closed magnetic field lines. But ultimately it also showed that we are at the moment not well enough equipped to unambiguously identify the true origin of the slow solar wind. With the data base now available to us the best course of action would be to enhance models like the PFSS model. With ever increasing computing power it is possible to increase the resolution of said models. Even more important is the resolution of the input magnetograms. With high resolution input it might be possible to conclusively confirm features like the S-web. With better models, studies restricted to spacecraft like ACE can help us to further establish a sophisticated idea of where and how the slow solar wind is released.
Ultimately, neither the origin of the slow solar wind nor the characteristics of energetic neutral particles can be conclusively explored without new instrumentation. Solar Orbiter has the potential to uncover the origin of the slow solar wind with its unique orbit and well rounded instrumentation. With our measurement scheme we contributed an important tool to this future mission. An improved PFSS model and a better understanding of the processes that might release the slow solar wind can greatly help interpreting the measurements Solar Orbiter is going to make. Regarding the energetic neutral atoms our new calibration facility will hopefully be

fully operational in the very near future in order to support all upcoming missions, thereby greatly supporting the building of our understanding of the many particle population found in the heliosphere.

BIBLIOGRAPHY

Altschuler, M. D. and Newkirk, G. (1969). Magnetic Fields and the Structure of the Solar Corona. I: Methods of Calculating Coronal Fields. *Sol. Phys.*, 9:131–149.

Altschuler, M. D., Trotter, D. E., and Orrall, F. Q. (1972). Coronal Holes. *Sol. Phys.*, 26:354–365.

Antiochos, S. K., DeVore, C. R., Karpen, J. T., and Mikić, Z. (2007). Structure and Dynamics of the Sun's Open Magnetic Field. *ApJ*, 671:936–946.

Antiochos, S. K., Mikić, Z., Titov, V. S., Lionello, R., and Linker, J. A. (2011). A Model for the Sources of the Slow Solar Wind. *ApJ*, 731:112.

Aschwanden, M. J. (2004). *Physics of the Solar Corona: An Introduction*. Springer, Berlin.

Balogh, A., Beek, T. J., Forsyth, R. J., Hedgecock, P. C., Marquedant, R. J., Smith, E. J., Southwood, D. J., and Tsurutani, B. T. (1992). The magnetic field investigation on the ULYSSES mission - Instrumentation and preliminary scientific results. *A&AS*, 92:221–236.

Balogh, A. and Erdõs, G. (2013). The Heliospheric Magnetic Field. *Space Sci. Rev.*, 176:177–215.

Bame, S. J., Asbridge, J. R., Feldman, W. C., and Gosling, J. T. (1977). Evidence for a structure-free state at high solar wind speeds. *J. Geophys. Res.*, 82:1487–1492.

Bame, S. J., McComas, D. J., Barraclough, B. L., Phillips, J. L., Sofaly, K. J., Chavez, J. C., Goldstein, B. E., and Sakurai, R. K. (1992). The ULYSSES solar wind plasma experiment. *A&AS*, 92:237–265.

Bentley, J. L. (1975). Multidimensional Binary Search Trees Used for Associative Searching . *ACM*, 18.

Berger, L. (2008). *Velocity Distribution Functions of Heavy Ions in the Solar Wind at 1 AU*. PhD thesis, Christian Albrechts Universitaet zu Kiel.

Berger, L., Wimmer-Schweingruber, R. F., and Gloeckler, G. (2010). 3D velocity distribution functions of heavy ions and kinetic properties of O^{6+} at 1 AU. *Twelfth International Solar Wind Conference*, 1216:253–256.

Beuhler, R. J. and Friedman, L. (1977). A model of secondary electron yields from atomic and polyatomic ion impacts on copper and tungsten surfaces based upon stopping-power calculations. *Journal of Applied Physics*, 48:3928–3936.

Bochsler, P. (2000). Abundances and charge states of particles in the solar wind. *Reviews of Geophysics*, 38:247–266.

Bogart, R. S. and Scherrer, P. H. (1986). Solar rotation measured at the Wilcox Solar Observatory. In *Bulletin of the American Astronomical Society*, volume 18 of *BAAS*, page 848.

Borovsky, J. E. (2008). Flux tube texture of the solar wind: Strands of the magnetic carpet at 1 AU? *Journal of Geophysical Research (Space Physics)*, 113:A08110.

Carrington, R. C. (1855). On a Method of Observing the Spots of the Sun. *MNRAS*, 15:174.

De Moortel, I., Browning, P., Bradshaw, S. J., Pintér, B., and Kontar, E. P. (2008). The way forward for coronal heating. *Astronomy and Geophysics*, 49(3):3.21–3.26.

Domingo, V., Fleck, B., and Poland, A. I. (1995). SOHO: The Solar and Heliospheric Observatory. *Space Sci. Rev.*, 72:81–84.

Drews, C., Berger, L., Taut, A., Peleikis, T., and Wimmer-Schweingruber, R. F. (2015). 2D He^+ pickup ion velocity distribution functions: STEREO PLASTIC observations. *A&A*, 575:A97.

Elliott, H. A., McComas, D. J., Schwadron, N. A., Gosling, J. T., Skoug, R. M., Gloeckler, G., and Zurbuchen, T. H. (2005). An improved expected temperature formula for identifying interplanetary coronal mass ejections. *Journal of Geophysical Research: Space Physics*, 110(A4):n/a–n/a. A04103.

European Space Agency (2008). Esa website. http://sci.esa.int/ulysses/41770-ulysses-orbit-plot-up-to-march-2009/.

Fisk, L. A., Gloeckler, G., Zurbuchen, T. H., Geiss, J., and Schwadron, N. A. (2003). Acceleration of the Solar Wind as a Result of the Reconnection of Open Magnetic Flux with Coronal Loops. In Velli, M., Bruno, R., Malara, F., and Bucci, B., editors, *Solar Wind Ten*, volume 679 of *American Institute of Physics Conference Series*, pages 287–292.

Fludra, A., Griffin, D., Caldwell, M., Eccleston, P., Cornaby, J., Drummond, D., Grainger, W., Greenway, P., Grundy, T., Howe, C., McQuirk, C., Middleton, K., Poyntz-Wright, O., Richards, A., Rogers, K., Sawyer, C., Shaughnessy, B., Sidher, S., Tosh, I., Beardsley, S., Burton, G., Marshall, A., Waltham, N., Woodward, S., Appourchaux, T., Philippon, A., Auchere, F., Buchlin, E., Gabriel, A., Vial, J.-C., Schühle, U., Curdt, W., Innes, D., Meining, S., Peter, H., Solanki, S., Teriaca, L., Gyo, M., Büchel, V., Haberreiter, M., Pfiffner, D., Schmutz, W., Carlsson, M., Haugan, S. V., Davila, J., Jordan, P., Thompson, W., Hassler, D., Walls, B., Deforest, C., Hanley, J., Johnson, J., Phelan, P., Blecha, L., Cottard, H., Paciotti, G., Autissier, N., Allemand, Y., Relecom, K., Munro, G., Butler, A., Klein, R., and Gottwald, A. (2013). SPICE EUV spectrometer for the Solar Orbiter mission. In *Solar Physics and Space Weather Instrumentation V*, volume 8862 of *Proc. SPIE*, page 88620F.

Forsyth, R. J. (1995). The High Latitude Heliospheric Magnetic Field. *Space Sci. Rev.*, 72:153–163.

Gabriel, A. H. (1971). Measurements on the Lyman Alpha Corona (Papers presented at the Proceedings of the International Symposium on the 1970 Solar Eclipse, held in Seattle, U. S. A. , 18-21 June, 1971.). *Sol. Phys.*, 21:392–400.

Galvin, A. B., Gloeckler, G., Ipavich, F. M., Shafer, C. M., Geiss, J., and Ogilvie, K. (1993). Solar wind composition measurements by the ULYSSES SWICS experiment during transient solar wind flows. *Advances in Space Research*, 13:75–78.

Gary, S. P. (1993). *Theory of Space Plasma Microinstabilities*.

Geiss, J., Gloeckler, G., and von Steiger, R. (1995). Origin of the Solar Wind From Composition Data. *Space Sci. Rev.*, 72:49–60.

Geiss, J., Gloeckler, G., and von Steiger, R. (1996). Origin of C^+ ions in the heliosphere. *Space Sci. Rev.*, 78:43–52.

Giordano, S., Antonucci, E., Noci, G., Romoli, M., and Kohl, J. L. (2000). Identification of the Coronal Sources of the Fast Solar Wind. *ApJ*, 531:L79–L82.

Gloeckler, G., Cain, J., Ipavich, F. M., Tums, E. O., Bedini, P., Fisk, L. A., Zurbuchen, T. H., Bochsler, P., Fischer, J., Wimmer-Schweingruber, R. F., Geiss, J., and Kallenbach, R. (1998). Investigation of the composition of solar and interstellar matter using solar wind and pickup ion measurements with SWICS and SWIMS on the ACE spacecraft. *Space Sci. Rev.*, 86:497–539.

Gloeckler, G., Geiss, J., Balsiger, H., Bedini, P., Cain, J. C., Fischer, J., Fisk, L. A., Galvin, A. B., Gliem, F., Hamilton, D. C., Hollweg, J. V., Ipavich, F. M., Joos, R., Livi, S., Lundgren, R. A., Mall, U., McKenzie, J. F., Ogilvie, K. W., Ottens, F., Rieck, W., Tums, E. O., von Steiger, R., Weiss, W., and Wilken, B. (1992). The Solar Wind Ion Composition Spectrometer. *A&AS*, 92:267–289.

Gonin, M., Kallenbach, R., and Bochsler, P. (1994). Charge exchange of atoms with high first ionization potentials in carbon foils at E $\leq$35 keV/u. *Nuclear Instruments and Methods in Physics Research B*, 94:15–21.

Gosling, J. T., Bame, S. J., Feldman, W. C., McComas, D. J., Phillips, J. L., Goldstein, B., Neugebauer, M., Burkepile, J., Hundhausen, A. J., and Acton, L. (1995). The band of solar wind variability at low heliographic latitudes near solar activity minimum: Plasma results from the Ulysses rapid latitude scan. *Geophys. Res. Lett.*, 22:3329–3332.

Grevesse, N. and Sauval, A. (2000). *Solar Abundances*.

Gringauz, K. I., Bezrokikh, V. V., Ozerov, V. D., and Rybchinskii, R. E. (1960). A Study of the Interplanetary Ionized Gas, High-Energy Electrons and Corpuscular Radiation from the Sun by Means of the Three-Electrode Trap for Charged Particles on the Second Soviet Cosmic Rocket. *Soviet Physics Doklady*, 5:361.

Heidrich-Meisner, V., Peleikis, T., Kruse, M., Berger, L., and Wimmer-Schweingruber, R. (2016). Observations of high and low Fe charge states in individual solar wind streams with coronal-hole origin. *A&A*, 593:A70.

Heidrich-Meisner, V., Peleikis, T., Kruse, M., Berger, L., and Wimmer-Schweingruber, R. (2017). Evolution of an equatorial coronal hole structure and the released coronal hole wind stream: CR 2039-2050. *A&A*.

Henkel, P., Roy, R., and Wiza, J. (1978). High Gain Microchannel Plates. *IEEE Transactions on Nuclear Science*, 25:548–549.

Hoeksema, J. T., Scherrer, P. H., Title, A. M., and Tarbell, T. D. (1988). The Michelson Doppler imager for the solar oscillations imager program on SOHO. In Rolfe, E. J., editor, *Seismology of the Sun and Sun-Like Stars*, volume 286 of *ESA Special Publication*.

Hollweg, J. V. (1990). Heating of the solar corona. *Computer Physics Reports*, 12:205–232.

Hundhausen, A. J. (1972). Coronal Expansion and Solar Wind. *Physics and Chemistry in Space*, 5.

Hundhausen, A. J. (1973). Solar wind stream interactions and interplanetary heat conduction. *J. Geophys. Res.*, 78:7996.

Hundhausen, A. J., Bame, S. J., Asbridge, J. R., and Sydoriak, S. J. (1970). Solar wind proton properties: Vela 3 observations from July 1965 to June 1967. *J. Geophys. Res.*, 75:4643.

Kallenbach, R., Geiss, J., Gloeckler, G., and von Steiger, R. (2000). Pick-up Ion Measurements in the Heliosphere - A Review. *Ap&SS*, 274:97–114.

Kallenbach, R., Gonin, M., Bürgi, A., and Bochsler, P. (1993). Charge exchange of hydrogen ions in carbon foils. *Nuclear Instruments and Methods in Physics Research B*, 83:68–72.

Kasper, J. C., Lazarus, A. J., and Gary, S. P. (2008). Hot Solar-Wind Helium: Direct Evidence for Local Heating by Alfvén-Cyclotron Dissipation. *Physical Review Letters*, 101(26):261103.

Koeten, M. (2009). *An Improved Efficiency Model for ACE/SWICS- Determination fo the Carbon Isotopic Ratio $^{13}C/^{14}C$ in the Solar Wind from ACE/SWICS Measurements*. PhD thesis, Christian Albrechts Universitaet zu Kiel.

Kolbe, S. (2007-2017). Solar wind lab cad drawings. Technical report, Universität zu Kiel.

Krieger, A. S., Timothy, A. F., and Roelof, E. C. (1973). A Coronal Hole and Its Identification as the Source of a High Velocity Solar Wind Stream. *Sol. Phys.*, 29:505–525.

Kruse, M. (2018). *Numerical PFSS Modeling*. PhD thesis, Christian Albrechst Universitaet zu Kiel. *In preperation*.

Landi, E., Alexander, R. L., Gruesbeck, J. R., Gilbert, J. A., Lepri, S. T., Manchester, W. B., and Zurbuchen, T. H. (2012). Carbon Ionization Stages as a Diagnostic of the Solar Wind. *ApJ*, 744:100.

Lebow Company (2013). http://www.lebowcompany.com/.

Leinert, C., Link, H., and Pitz, E. (1974). Die Sonnensonde Helios und ihre Experimente. *Sterne und Weltraum*, 13:86–91.

Livi, S., Galvin, A., Kistler, L., Collier, . M., Allegrini, F., Lepri, S., and Zurbuchen, T. (2012). Solar wind measurements on Solar Orbiter: discovering the links between the solar wind and the atmosphere of our Sun. In *39th COSPAR Scientific Assembly*, volume 39 of *COSPAR Meeting*, page 1101.

Livingston, W., Harvey, J., Pierce, K., Schrage, D., and Slaughter, C. (1974). Report on the Kitt Peak Vacuum Telescope. In *Bulletin of the American Astronomical Society*, volume 6 of *BAAS*, page 291.

Marsch, E. (2003). Wave-particle Interactions and Ion Kinetics in the Solar Corona and Solar Wind. *Astronomische Nachrichten Supplement*, 324:12.

Marsch, E., Schwenn, R., Rosenbauer, H., Muehlhaeuser, K.-H., Pilipp, W., and Neubauer, F. M. (1982). Solar wind protons - Three-dimensional velocity distributions and derived plasma parameters measured between 0.3 and 1 AU. *J. Geophys. Res.*, 87:52–72.

Marsden, R. G. and Smith, E. J. (1996). The Ulysses mission: an introduction. *Nuovo Cimento C Geophysics Space Physics C*, 19:909–914.

Marsden, R. G., Smith, E. J., Cooper, J. F., and Tranquille, C. (1996). ULYSSES at high heliographic latitudes: an introduction. *A&A*, 316:279–286.

Maruca, B. A., Bale, S. D., Sorriso-Valvo, L., Kasper, J. C., and Stevens, M. L. (2013). Collisional Thermalization of Hydrogen and Helium in Solar-Wind Plasma. *Physical Review Letters*, 111(24):241101.

McComas, D., Allegrini, F., Bochsler, P., Bzowski, M., Collier, M., Fahr, H., Fichtner, H., Frisch, P., Funsten, H., Fuselier, S., Gloeckler, G., Gruntman, M., Izmodenov, V., Knappenberger, P., Lee, M., Livi, S., Mitchell, D., Möbius, E., Moore, T., Reisenfeld, D., Roelof, E., Schwadron, N., Wieser, M., Witte, M., Wurz, P., and Zank, G. (2004). The Interstellar Boundary Explorer (IBEX). In Florinski, V., Pogorelov, N. V., and Zank, G. P., editors, *Physics of the Outer Heliosphere*, volume 719 of *American Institute of Physics Conference Series*, pages 162–181.

McComas, D. J., Bame, S. J., Barker, P., Feldman, W. C., Phillips, J. L., Riley, P., and Griffee, J. W. (1998a). Solar Wind Electron Proton Alpha Monitor (SWEPAM) for the Advanced Composition Explorer. *Space Sci. Rev.*, 86:563–612.

McComas, D. J., Barraclough, B. L., Funsten, H. O., Gosling, J. T., Santiago-Muñoz, E., Skoug, R. M., Goldstein, B. E., Neugebauer, M., Riley, P., and Balogh, A. (2000). Solar wind observations over Ulysses' first full polar orbit. *J. Geophys. Res.*, 105:10419–10434.

McComas, D. J., Riley, P., Gosling, J. T., Balogh, A., and Forsyth, R. (1998b). Ulysses' rapid crossing of the polar coronal hole boundary. *J. Geophys. Res.*, 103:1955.

Mewaldt, R. A., Cohen, C. S., Mason, G. M., Cummings, A. C., Davis, A. J., Labrador, A. W., Leske, R. A., Miyasaka, H., Stone, E. C., von Rosenvinge, T. T., and Wiedenbeck, M. E. (2007). Solar Energetic Particle Observations From the STEREO Low Energy Telescope (LET). *AGU Spring Meeting Abstracts*.

Mewaldt, R. A., Leske, R. A., Stone, E. C., Barghouty, A. F., Labrador, A. W., Cohen, C. M. S., Cummings, A. C., Davis, A. J., von Rosenvinge, T. T., and Wiedenbeck, M. E. (2009). STEREO Observations of Energetic Neutral Hydrogen Atoms During the 2006 December 5 Solar Flare. *ApJ*, 693:L11–L15.

Möbius, E., Hovestadt, D., Klecker, B., Scholer, M., Gloeckler, G., and Ipavich, F. M. (1985). Observation of He^+ pick-up ions in the solar wind. *Johns Hopkins APL Technical Digest*, 6:264.

Müller, D., Marsden, R. G., St. Cyr, O. C., and Gilbert, H. R. (2013). Solar Orbiter . Exploring the Sun-Heliosphere Connection. *Sol. Phys.*, 285:25–70.

Neugebauer, M., Forsyth, R. J., Galvin, A. B., Harvey, K. L., Hoeksema, J. T., Lazarus, A. J., Lepping, R. P., Linker, J. A., Mikic, Z., Steinberg, J. T., von Steiger, R., Wang, Y.-M., and Wimmer-Schweingruber, R. F. (1998). Spatial structure of the solar wind and comparisons with solar data and models. *J. Geophys. Res.*, 103:14587–14600.

Nittler, L., Starr, R. D., Schlemm, III, C., McNutt, R. L., and Solomon, S. C. (2010). Constraints on Solar Coronal Abundances from MESSENGER X-ray Solar Monitor Data. *AGU Fall Meeting Abstracts*.

Nolte, J. T., Davis, J. M., Gerassimenko, M., Krieger, A. S., Solodyna, C. V., and Golub, L. (1978). The relationship between solar activity and coronal hole evolution. *Sol. Phys.*, 60:143–153.

Nolte, J. T., Krieger, A. S., Timothy, A. F., Gold, R. E., Roelof, E. C., Vaiana, G., Lazarus, A. J., Sullivan, J. D., and McIntosh, P. S. (1976). Coronal holes as sources of solar wind. *Sol. Phys.*, 46:303–322.

Orsini, S., Livi, S., Torkar, K., Barabash, S., Milillo, A., Wurz, P., di Lellis, A. M., Kallio, E., and The Serena Team (2010). SERENA: A suite of four instruments (ELENA, STROFIO, PICAM and MIPA) on board BepiColombo-MPO for particle detection in the Hermean environment. *Planet. Space Sci.*, 58:166–181.

Owens, M. J. and Forsyth, R. J. (2013). The Heliospheric Magnetic Field. *Living Reviews in Solar Physics*, 10(1):5.

Panitzsch, L., Peleikis, T., Böttcher, S., Stalder, M., and Wimmer-Schweingruber, R. F. (2013). Current density distributions and sputter marks in electron cyclotron resonance ion sources. *Review of Scientific Instruments*, 84(1):013303–013303.

Panitzsch, L., Peleikis, T., Stalder, M., and Wimmer-Schweingruber, R. F. (2011). Spatially resolved charge-state and current-density distributions at the extraction of an electron cyclotron resonance ion source. *Review of Scientific Instruments*, 82(9):093302–093302.

Parker, E. N. (1958). Dynamics of the Interplanetary Gas and Magnetic Fields. *ApJ*, 128:664.

Parker, E. N. (1965). Dynamical Theory of the Solar Wind. *Space Sci. Rev.*, 4:666–708.

Peleikis, T. (2011). Neutralisierung eines ionenstrahls.

Peleikis, T., Kruse, M., Berger, L., Drews, C., and Wimmer-Schweingruber, R. (2016). Investigation of solar wind source regions using ulysses composition data and a pfss model. *AIP Conference Proceedings*, 1720(1):020003.

Peleikis, T., Kruse, M., Berger, L., and Wimmer-Schweingruber, R. (2017). Origin of the solar wind: A novel approach to link in situ and remote observations a study for spice and swa on the upcoming solar orbiter mission. *A&AS*.

Pesnell, W. D., Thompson, B. J., and Chamberlin, P. C. (2012). The Solar Dynamics Observatory (SDO). *Sol. Phys.*, 275:3–15.

Pinto, R. F., Brun, A. S., and Rouillard, A. P. (2016). Flux-tube geometry and solar wind speed during an activity cycle. *A&A*, 592:A65.

Potgieter, M. (2012). Hundred years of cosmic rays in the heliosphere. In *39th COSPAR Scientific Assembly*, volume 39 of *COSPAR Meeting*, page 1532.

Schatten, K. H., Wilcox, J. M., and Ness, N. F. (1969). A model of interplanetary and coronal magnetic fields. *Sol. Phys.*, 6:442–455.

Schwadron, N. A., McComas, D. J., Elliott, H. A., Gloeckler, G., Geiss, J., and von Steiger, R. (2005). Solar wind from the coronal hole boundaries. *Journal of Geophysical Research (Space Physics)*, 110:A04104.

Senanayake, U. K., Florinski, V., Cummings, A. C., and Stone, E. C. (2015). Spectral Evolution of Anomalous Cosmic Rays at Voyager 1 beyond the Termination Shock. *ApJ*, 804:12.

Smith, C. W., L'Heureux, J., Ness, N. F., Acuña, M. H., Burlaga, L. F., and Scheifele, J. (1998). The ACE Magnetic Fields Experiment. *Space Sci. Rev.*, 86:613–632.

Smith, J. E. (1989). Interplanetary magnetic field over two solar cycles and out to 20 AU. *Advances in Space Research*, 9:159–169.

Snyder, C. W. and Neugebauer, M. (1963). Direct Observations of the Solar Wind by the Mariner II spacecraft. *International Cosmic Ray Conference*, 1:210.

Stalder, M. (2008). *Entwicklung einer neuen EZR-Ionenquelle für das Kieler Sonnenwindlabor*. PhD thesis, Christian Albrechts Universitaet zu Kiel.

Stix, T. H. (1992). *Waves in plasmas*.

Stone, E. C., Burlaga, L. F., Cummings, A. C., Feldman, W. C., Frain, W. E., Geiss, J., Gloeckler, G., Gold, R. E., Hovestadt, D., Krimigis, S. M., Mason, G. M., McComas, D., Mewaldt, R. A., Simpson, J. A., von Rosenvinge, T. T., and Wiedenbeck, M. E. (1990). The advanced composition explorer. In Jones, W. V., Kerr, F. J., and Ormes, J. F., editors, *Particle Astrophysics - The NASA Cosmic Ray Program for the 1990s and Beyond*, volume 203 of *American Institute of Physics Conference Series*, pages 48–57.

The Ace Science Center (2008). The ace science center. http://www.srl.caltech.edu/ACE/ASC/.

Tu, C.-Y., Zhou, C., Marsch, E., Xia, L.-D., Zhao, L., Wang, J.-X., and Wilhelm, K. (2005). Solar Wind Origin in Coronal Funnels. *Science*, 308:519–523.

Ulysses Final Archive (2008). Ulysses final archive. http://ufa.esac.esa.int/ufa/data.

von Rosenvinge, T., Cummings, A., Cohen, C., Leske, R., Mewaldt, R., Stone, E., and Wiedenbeck, M. (2007). The High Energy Telescopes for the STEREO Mission. *AGU Spring Meeting Abstracts*.

von Steiger, R., Schwadron, N. A., Fisk, L. A., Geiss, J., Gloeckler, G., Hefti, S., Wilken, B., Wimmer-Schweingruber, R. F., and Zurbuchen, T. H. (2000). Composition of quasi-stationary solar wind flows from Ulysses/Solar Wind Ion Composition Spectrometer. *J. Geophys. Res.*, 105:27217–27238.

von Steiger, R., Zurbuchen, T. H., and McComas, D. J. (2010). Oxygen flux in the solar wind: Ulysses observations. *Geophys. Res. Lett.*, 37:L22101.

Wang, Y., Zhao, Y., Qayyum, A., and Xiao, G. (2007). Separation of potential and kinetic electron emission from Si and W induced by multiply charged neon and argon ions. *Nuclear Instruments and Methods in Physics Research B*, 265:474–478.

Wang, Y.-M. (2012). Semiempirical Models of the Slow and Fast Solar Wind. *Space Sci. Rev.*, 172:123–143.

Wenzel, K. P., Marsden, R. G., Page, D. E., and Smith, E. J. (1992). The ULYSSES Mission. *A&AS*, 92:207.

Whang, Y. C. and Burlaga, L. F. (1989). Recurrent solar wind structures in the outer heliosphere. *Advances in Space Research*, 9:111–116.

Wimmer-Schweingruber, R. F., von Steiger, R., and Paerli, R. (1997). Solar wind stream interfaces in corotating interaction regions: SWICS/Ulysses results. *J. Geophys. Res.*, 102:17407–17418.

Witte, M., Rosenbauer, H., Keppler, E., Fahr, H., Hemmerich, P., Lauche, H., Loidl, A., and Zwick, R. (1992). The interstellar neutral-gas experiment on ULYSSES. *A&AS*, 92:333–348.

Xu, F. and Borovsky, J. E. (2015). A new four-plasma categorization scheme for the solar wind. *Journal of Geophysical Research (Space Physics)*, 120:70–100.

Zhao, L., Zurbuchen, T. H., and Fisk, L. A. (2009). Global distribution of the solar wind during solar cycle 23: ACE observations. *Geophys. Res. Lett.*, 36:L14104.

Ziegler, J. (2007). Stopping and Range of Ions in Matter. http://www.srim.org/.

Zurbuchen, T. and von Steiger, R. (2000). Ulysses/swics data archive.

Zurbuchen, T. H., von Steiger, R., Gruesbeck, J., Landi, E., Lepri, S. T., Zhao, L., and Hansteen, V. (2012). Sources of Solar Wind at Solar Minimum: Constraints from Composition Data. *Space Sci. Rev.*, 172:41–55.

Part I

APPENDIX

9 UNEXPECTED VARIABILITY IN THE FAST SOLAR WIND

In this chapter a supplementary publication for this work is presented, which is related to the study covered in chapter 5. Here the focus lies upon the fast solar wind instead of the slow solar wind. The reason why this study is presented here is because the same combination of ballistic back mapping and magnetic mapping is used as in the publication presented in chapter 5.

9.1 BRIEF SUMMARY OF THE PUBLICATION

This study discusses variations in fast solar wind. In contrast to the high variability of the slow solar wind, coronal hole wind has been thought to be extremely stable in all its parameters. This concerns plasma parameters like proton density and velocity, but also the charge state ratios found in the fast solar wind are supposed to be unchanging in individual streams. Because of that the fast solar wind has been considered to be well understood when compared to the slow solar wind. The following study shows that this is by far not the case and that even the fast solar wind is still an unexhausted subject of research.
This study reveals that the charge state ratios of iron ions show an entirely unexpected behavior, in that the average iron charge state in individual fast solar wind streams can frequently reach values which are comparable to those found in slow solar wind streams. Meanwhile, the oxygen and carbon charge states remain as low as expected for coronal hole plasma. This cast a new light on the origination processes of the fast solar wind, which therefore might not be as well understood as it is believed right now.

Own Contribution to Publication: 20%

The following article is reproduced from Heidrich-Meisner et al. (2016), with permission ©ESO.
Despite scientific discussions the second author Thies Peleikis contributed figure 6 and figure 8 and the related handling of the PFSS data and the magnetic mapping of the solar wind data through the corona.

A&A 593, A70 (2016)
DOI: 10.1051/0004-6361/201527998

Astronomy & Astrophysics

Observations of high and low Fe charge states in individual solar wind streams with coronal-hole origin

Verena Heidrich-Meisner, Thies Peleikis, Martin Kruse, Lars Berger, and Robert Wimmer-Schweingruber

Christian Albrechts University at Kiel, 24118 Kiel, Germany
e-mail: heidrich@physik.uni-kiel.de

Received 18 December 2015 / Accepted 18 July 2016

ABSTRACT

Context. The solar wind originating from coronal holes is comparatively well-understood and is characterized by lower densities and average charge states compared to the so-called slow solar wind. Except for wave perturbations, the average properties of the coronal-hole solar wind are passably constant.
Aims. In this case study, we focus on observations of the Solar Wind Ion Composition Spectrometer (SWICS) on the Advanced Composition Explorer (ACE) of individual streams of coronal-hole solar wind that illustrate that although the O and C charge states are low in coronal-hole wind, the Fe charge distribution is more variable. In particular, we illustrate that the Fe charge states in coronal-hole solar wind are frequently as high as in slow solar wind.
Methods. We selected individual coronal-hole solar wind streams based on their collisional age as well as their respective O and C charge states and analyzed their Fe charge-state distributions. Additionally, with a combination of simple ballistic back-mapping and the potential field source surface model, transitions between streams with high and low Fe charge states were mapped back to the photosphere. The relative frequency of high and low Fe charge-state streams is compared for the years 2004 and 2006.
Results. We found several otherwise typical coronal-hole streams that include Fe charge states either as high as or lower than in slow solar wind. Eight such transitions in 2006 were mapped back to equatorial coronal holes that were either isolated or connected to the northern coronal-hole. Attempts to identify coronal structures associated with the transitions were so far inconclusive.

Key words. solar wind – Sun: heliosphere – Sun: magnetic fields

1. Introduction

The steady solar wind is typically divided into two dominant types, fast and slow solar wind. However, the differences in their properties are better ordered by elemental and charge-state abundances rather than by solar wind speed. Here, we focus on fast solar wind. It has been uniquely identified as originating from coronal holes and the release mechanism is well understood (i.e. Tu et al. 2005). Therefore, in the following, we use the term coronal-hole wind instead of fast solar wind. Aside from fluctuations caused by waves (mainly Alfvénic waves), its plasma and compositional properties are constant (e.g. von Steiger et al. 2000). Both the elemental and charge-state compositions of the solar wind reflect the conditions in the respective solar source regions. In particular, the charge-state distribution for each solar wind ion species is (almost completely) determined in the corona. For each ion pair the recombination and ionization rates are temperature dependent and the hot corona allows high ionization states to occur. For a pair of adjacent ionization states $i \leftrightarrow i+1$, this can be expressed by a temperature dependent charge modification time scale $\tau_{\mathrm{mod},i}(T) = \frac{1}{n_{\mathrm{e}}(C_i+R_{i+1})}$, where T denotes the electron temperature in K, n_{e} the electron density, C_i the ionization rate of the ith ionization state, and R_{i+1} the recombination rate of the $(i+1)$th to the ith ionization state. But the ionization state is not only temperature dependent. A sufficiently high electron density is required to allow recombination. Thus, a simple model to explain the observed solar wind speeds and charge states assumes that the charge state can change along the solar-wind flux tube until the expansion time scale (which depends on the electron density profile in the corona) is of the same order as the charge modification time scale of an ion pair. Beyond this point the charge-state distribution remains "frozen-in" as the solar wind propagates further outwards.

The coronal-hole wind is known for comparatively low O and C charge states and corresponding freeze-in temperatures. They are particularly low compared to those of the slow solar wind. The O charge-state distribution can be considered as a tracer for the solar wind type. The ratio $n_{O^{7+}}/n_{O^{6+}}$ of the densities of O^{7+} to O^{6+} (denoted with $n_{O^{7+}}$ and $n_{O^{6+}}$, respectively) has been frequently used in solar wind categorization schemes (e.g. Zurbuchen et al. 2002; Zhao et al. 2009) to differentiate between fast (coronal hole) and slow solar wind. In accordance with the cool O and C signatures in coronal-hole wind, the charge-state distributions of other ions, for example Fe, could also be expected to be cooler in the coronal-hole wind than in the slow solar wind. However, that is clearly not necessarily the case.While the Ulysses observations in von Steiger et al. (2000), Richardson (2014) and Zhao & Landi (2014, as well as the ACE observations in Zhao & Landi 2014) show on average higher Fe charge states in the fast solar wind than in the slow solar wind (see for example Plate 5 in von Steiger et al. 2000), the STEREO results (Galvin et al. 2009) indicate lower Fe charge states in coronal-hole wind. For example, for the solar-wind speed bin 650−700 km s^{-1} the average Fe charge state in coronal-hole wind observed with PLASTIC on STEREO A from 2007−2009 is given as 9.25, which is lower than for all slow

solar wind bins considered in that article. For all other high speed bins, the average Fe charge state is even lower. Zhao & Landi (2014) compared long-term properties of coronal-hole wind at different solar minima and identified two subcategories, coronal-hole wind originating from polar coronal holes and coronal-hole wind originating from the equatorial region. Lower Fe charge states were observed in equatorial coronal-hole wind than in polar coronal holes and additionally lower charge states were found in the second solar minimum. A gradual charge-state decrease for O, C, and Fe from solar maximum to the following solar minimum in solar cycle 23 has been discussed in Lepri et al. (2013) and Zhao & Fisk (2010) underlines differences in the composition of the slow solar wind between the two consecutive solar minima in solar cycles 22 and 23.

Instead of focusing on the statistics of charge-state parameters gathered over long time periods, we discuss several case studies of individual streams within the ACE/SWICS data that show regions of high and low Fe charge states with a clear transition between these regions. We then map these streams back to their coronal sources and assess whether there are any coronal structures that may be associated with these transitions.

2. Data analysis and event selection

The SWICS instrument on ACE (Gloeckler et al. 1998) combines a time-of-flight mass spectrometer and energy-per-charge analyzer with an energy measurement. A detailed and extensive description of the data analysis procedure applied to the pulse height amplitude (PHA) data is given in the PhD thesis Berger (2008) and has been applied in, e.g. Berger et al. (2011).

The proton density n_p (from the Solar Wind Electron, Proton and Alpha Monitor (SWEPAM) on ACE, McComas et al. 1998), and the densities of O^{6+}, O^{7+}, C^{5+}, and C^{6+} are used for the characterization of solar-wind plasma as coronal-hole wind. We selected coronal-hole-wind streams based on four-hour resolution data from SWICS and SWEPAM and the following three criteria: (1) Low O and C charge-state ratios ($n_{O^{7+}}/n_{O^{6+}}$ and $n_{C^{6+}}/n_{C^{5+}}$, respectively) are considered as the decisive property for identifying coronal-hole wind. Zhao et al. (2009) proposed an upper limit of $n_{O^{7+}}/n_{O^{6+}} < 0.145$ for coronal-hole wind. To avoid potential contamination with inter-stream solar wind, we apply $n_{O^{7+}}/n_{O^{6+}} < 0.1$ which was also used in Zurbuchen et al. (2002). For C, we adopted an upper threshold of $n_{C^{6+}}/n_{C^{5+}} < 1$. (2) Based on the observations in Kasper et al. (2008), we additionally require a low collisional age $a_{col} = \frac{r}{v_p \tau_{col}} < 0.1$, with r as the distance from the Sun to ACE, v_p the solar-wind proton speed, and τ_{col} the time scale for α to proton energy exchange due to small-angle Coulomb scattering, where $\tau_{col} \sim n_p T_p^{-3/2}$. The collisional age is defined by the ratio of expansion and collisional time scales. Although the proton-proton collisional age is not representative for the collisional properties of the entire solar-wind plasma, we consider the proton-proton collisional age as a representative marker for the solar-wind stream type. (3) Only streams that remained within the respective same categorization regimes of the average O and C charge states and collisional age for at least half a day were considered. Fluctuations in a_{col}, $n_{O^{7+}}/n_{O^{6+}}$, $n_{C^{6+}}/n_{C^{5+}}$, or the average Fe charge-state on smaller time scales than the four hours were permitted as long as the average value (averaged over four hours) remained in the respective range.

As a comparison baseline we also require pure slow solar wind. In this context, pure slow solar wind is characterized by high O charge states $n_{O^{7+}}/n_{O^{6+}} > 0.1$, high C charge states $n_{C^{6+}}/n_{C^{5+}} > 1$, and high collisional age $a_{col} > 0.4$. This characterization of slow solar wind is not directly complementary to the criteria for identifying coronal-hole wind as described above in order to reduce the contamination of each wind type by transition regions that exhibit a mixture of properties of slow and coronal-hole wind.

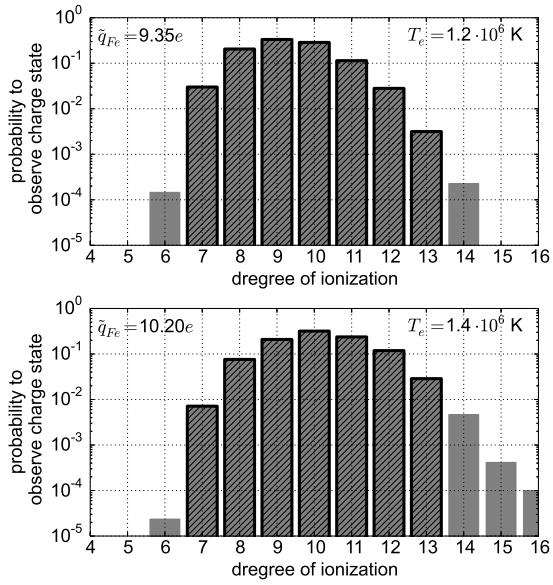

Fig. 1. *Top panel*: Fe charge-state distribution at $T = 1.2 \times 10^6$ K taken from the CHIANTI database. *Bottom panel*: Fe charge-state distribution at $T = 1.4 \times 10^6$ K from the CHIANTI. The black borders indicate the Fe charge states considered in this work. In both panels, the mean Fe charge-state $\tilde{q}_{Fe}$ is given as inset on the *left*.

In this study, we are interested in the Fe charge-state distribution in coronal-hole wind. The densities of the Fe charge states are provided by ACE/SWICS. In particular, since the most abundant Fe charge states are well isolated from all other ions in the SWICS m-m/q diagram, we focus on these, namely Fe^{7+}, Fe^{8+}, Fe^{9+}, Fe^{10+}, Fe^{11+}, Fe^{12+}, and Fe^{13+}. In the following the average Fe charge-state $\tilde{q}_{Fe}$ is defined as $\tilde{q}_{Fe} = \sum_{c=7}^{13} c n_{Fe^{c+}} / \sum_{c=7}^{13} n_{Fe^{c+}}$.

Figure 1 shows the Fe charge-state distribution for two electron temperatures $T = 1.2 \times 10^6$ K (top) and $T = 1.4 \times 10^6$ K (bottom) as provided by the atomic database CHIANTI (Dere et al. 1997; Landi et al. 2013). The temperatures are chosen from the typical range of observed electron temperatures in the corona (see e.g. Ko et al. 1997; Wilhelm 2012). The charge states considered here (Fe^{7+}, Fe^{8+}, Fe^{9+}, Fe^{10+}, Fe^{11+}, Fe^{12+}, and Fe^{13+}) are highlighted by hatched bars and black borders around the respective bars and are at the relevant temperatures the most prominent charge states.

Based on the CHIANTI data displayed in Fig. 1 and under the assumptions that the freeze-in temperature $T_{f,Fe}$ for all Fe ions is the same and that $T_{f,Fe} \sim 1.2 \times 10^6$ K, Fig. 1 also illustrates that $q_{Fe} = 9$ would be the most likely charge state, with a mean charge state of 9.35. For $T = 1.4 \times 10^6$ K a mean charge state of 10.2 would be expected. However, since the assumption that all Fe ions freeze-in at the same temperature is not accurate, this provides only a rough guideline. Furthermore CHIANTI makes the assumption of a Maxwellian distribution for the electron velocity distribution function which is known not to be the appropriate choice for the solar corona and the solar wind (see for example, Marsch 2006). Instead our notion of high or low average Fe charge state is based on a comparison

of Fe charge states in coronal-hole wind to those observed in selected samples of slow solar wind.

For 2004 the median of the average Fe charge-state of pure slow solar wind was $\tilde{q}_{\mathrm{Fe,slow}} = 9.87$. The 1σ-level is bounded below by $\tilde{q}_{\mathrm{Fe,slow}} - \sigma = 9.54$. These values are used to define our notion of high and low Fe charge states. We consider the average Fe charge state $\tilde{q}_{\mathrm{Fe,CH}}$ of a coronal-hole-wind stream as low and the stream as Fe-cool if $\tilde{q}_{\mathrm{Fe,CH}} < \tilde{q}_{\mathrm{Fe,slow}} - \sigma$. Analogously, we consider a coronal-hole-wind stream to be Fe-hot if its average Fe charge-state is within one σ of the average Fe charge state of pure slow solar wind for that year or higher: $\tilde{q}_{\mathrm{Fe,CH}} > \tilde{q}_{\mathrm{Fe,slow}} - \sigma$. Thus for 2004, the threshold value is $\tilde{q}_{\mathrm{Fe,slow}} - \sigma = 9.54$ and for 2006 $\tilde{q}_{\mathrm{Fe,slow}} - \sigma = 9.71$.

To ensure that the selected coronal-hole-wind streams are not contaminated with interplanetary coronal mass ejections (ICMEs), we cross-referenced the Jian et al. (2006, 2011) and Richardson & Cane (2010) ICME lists and the Large Angle and Spectrometric Coronagraph (LASCO) CME list and excluded all time periods with ICMEs from our times of interest. For four days after each halo CME in the LASCO list (Yashiro et al. 2004; Gopalswamy et al. 2009) that does not have a counterpart in the ICME lists, we verified that no ICME signatures were contained in the coronal-hole-wind stream candidates. Also, to reduce the effect of inter-stream regions, time periods with enhanced proton density and magnetic field strength which indicate stream interaction-regions (Jian et al. 2006, 2011) were excluded as well. With this method, 4660 12-min observations were selected as coronal-hole wind in 2004, accumulating to 38.8 days of combined coronal-hole wind, and 8346 observations corresponding to 69.5 days of combined coronal-hole wind in 2006. For the sake of an unbiased representation, we randomly chose three transitions from two different years between Fe-cool and Fe-hot coronal-hole wind from the available data set to be discussed in detail in the following section: day of year (DoY) 2−14 in 2004 and DoY 158−162 and DoY 212−215 in 2006. Six additional transitions in 2006 are mentioned briefly.

3. Fe charge states of individual coronal-hole-wind streams

We now focus on the Fe charge-state distribution of individual coronal-hole-wind streams and relate the average Fe charge state of these to the average Fe charge-state of all slow solar wind streams of the same year.

Figure 2 summarizes the solar wind properties for 12 days in 2004. From top to bottom, the panels in Fig. 2 show the collisional age a_{col}, the ratios $n_{\mathrm{O^{7+}}}/n_{\mathrm{O^{6+}}}$ and $n_{\mathrm{C^{6+}}}/n_{\mathrm{C^{5+}}}$, the corresponding freeze-in temperatures $T_{f,\mathrm{O^{7+}/O^{6+}}}$ and $T_{f,\mathrm{C^{6+}/C^{5+}}}$, the magnetic field strength B and angles B_ϕ, B_θ, and in the bottom panel the proton speed v_{p} (left y-axis) and proton density n_{p} (right y-axis). A coronal-hole stream (DoY 3.5−6.5) is followed by an interface region with a higher-speed stream and an ICME beginning on DoY 9. The ICME period is marked with gray hatching. From DoY 3.5 to DoY 6.5, $n_{\mathrm{O^{7+}}}/n_{\mathrm{O^{6+}}}$ and $n_{\mathrm{C^{6+}}}/n_{\mathrm{C^{5+}}}$ are low and, in particular, are below their respective thresholds for coronal-hole wind. The collisional age a_{col} is below its threshold value of 0.1 for coronal-hole wind as well. Thus, according to the criteria described in Sect. 2, this suffices to categorize this stream as fast, that is, as coronal-hole wind. This is supported by the additional data products shown in Fig. 2. Although there is some variability in the solar-wind proton speed v_{p}, the minimal value is still unlikely to be produced by slow solar wind. The freeze-in temperatures are derived under the assumption of an equilibrium state that allows us to relate the observed abundance ratio of two adjacent ions to the respective ionization and recombination rates: $n_i/n_{i+1} = R_{i+1}(T_f)/C_i(T_f)$. Since they depend on the density ratios $n_{\mathrm{O^{7+}}}/n_{\mathrm{O^{6+}}}$ and $n_{\mathrm{C^{6+}}}/n_{\mathrm{C^{5+}}}$ it is not surprising that the freeze-in temperatures are low during the coronal-hole-wind stream as well.

Although still below the threshold for coronal-hole wind defined above, the $n_{\mathrm{O^{7+}}}/n_{\mathrm{O^{6+}}}$ ratio and the collisional age are higher from DoY 3.5 to DoY 4.25 than in the following period. To prevent any interference by other processes, we focus on the part of the coronal-hole-wind stream from DoY 4.5−6.5 where both density ratios are safely below their respective categorization thresholds. Based on these considerations, the time period from DoY 4.5−6.5 (which is indicated with the gray shaded area in Fig. 2) contains only typical, quiet coronal-hole wind.

The ICME period exhibits a much larger variability in all data products; in particular, the $n_{\mathrm{O^{7+}}}/n_{\mathrm{O^{6+}}}$ and the collisional age are much higher. The magnetic-field angles show a smooth rotation indicating a magnetic cloud as part of the ICME. Thus, this ICME can easily be distinguished from the coronal-hole-wind stream.

Figure 3 focuses on the highlighted part of the coronal-hole-wind stream (DoY 4.5−6.5) from Fig. 2. For this time period of interest, Fig. 3 examines how the individual Fe charge states behave during DoY 4.5−5.6 and DoY 5.6−6.5. The motivation for this partition is detailed in Fig. 4. The upper five panels of Fig. 3 show the density ratios of C, O, and Fe ion pairs within these two parts of the coronal-hole-wind stream of interest, and the bottom panel provides examples of the charge-state distributions of C, O, and Fe for two selected observations. The vertical lines in the upper panels indicate the corresponding times used in the bottom panel. The horizontal lines in each panel give the mean density ratio in the left and right interval, respectively. All Fe ion density ratios shown here are higher in the first part of the stream than in the second part. Comparing the two charge-state distribution examples at the bottom, in the example on the left, not only is the maximum of the Fe charge-state distribution shifted from $\mathrm{Fe^{9+}}$ to $\mathrm{Fe^{10+}}$ as compared to the second example, but the complete distribution is shifted to higher charge states. Thus, a change in the mean charge-state cannot be explained by a single enhanced or depleted charge-state. Instead all considered charge states are affected.

As a continuous representation of the charge-state distributions in the bottom panel of Fig. 3, Fig. 4 shows a time series of the Fe charge-state distribution (considering only $\mathrm{Fe^{7+}}$ to $\mathrm{Fe^{13+}}$) in the first panel. The three bottom panels provide the solar-wind proton speed v_{p}, proton density n_{p}, and the ratio $n_{\mathrm{O^{7+}}}/n_{\mathrm{O^{6+}}}$ as reference. During DoY 4.5–5.6 the charge-state distribution of Fe is shifted to higher charge states more similar to those observed in slow solar wind. A transition between Fe-hot and Fe-cool coronal-hole wind (marked with a vertical black line) occurs at DoY 5.6. After the transition, at 5.6−6.5, lower Fe charge states are observed. Both the characterization as Fe-cool or Fe-hot wind and the resulting transition point are defined on four-hour resolution data. The same transition divides the left and right parts of the five top panels in Fig. 3. It is interesting to note that the Fe-hot part of the stream coincides with an average solar wind speed below 600 km s^{-1}, whereas the Fe-cool interval shows an average solar wind speed higher than 600 km s^{-1}. This hints at a potential stream boundary between two high-speed streams that coincides with the transition between Fe-hot and Fe-cool coronal-hole wind as a possible explanation for the observed transition.

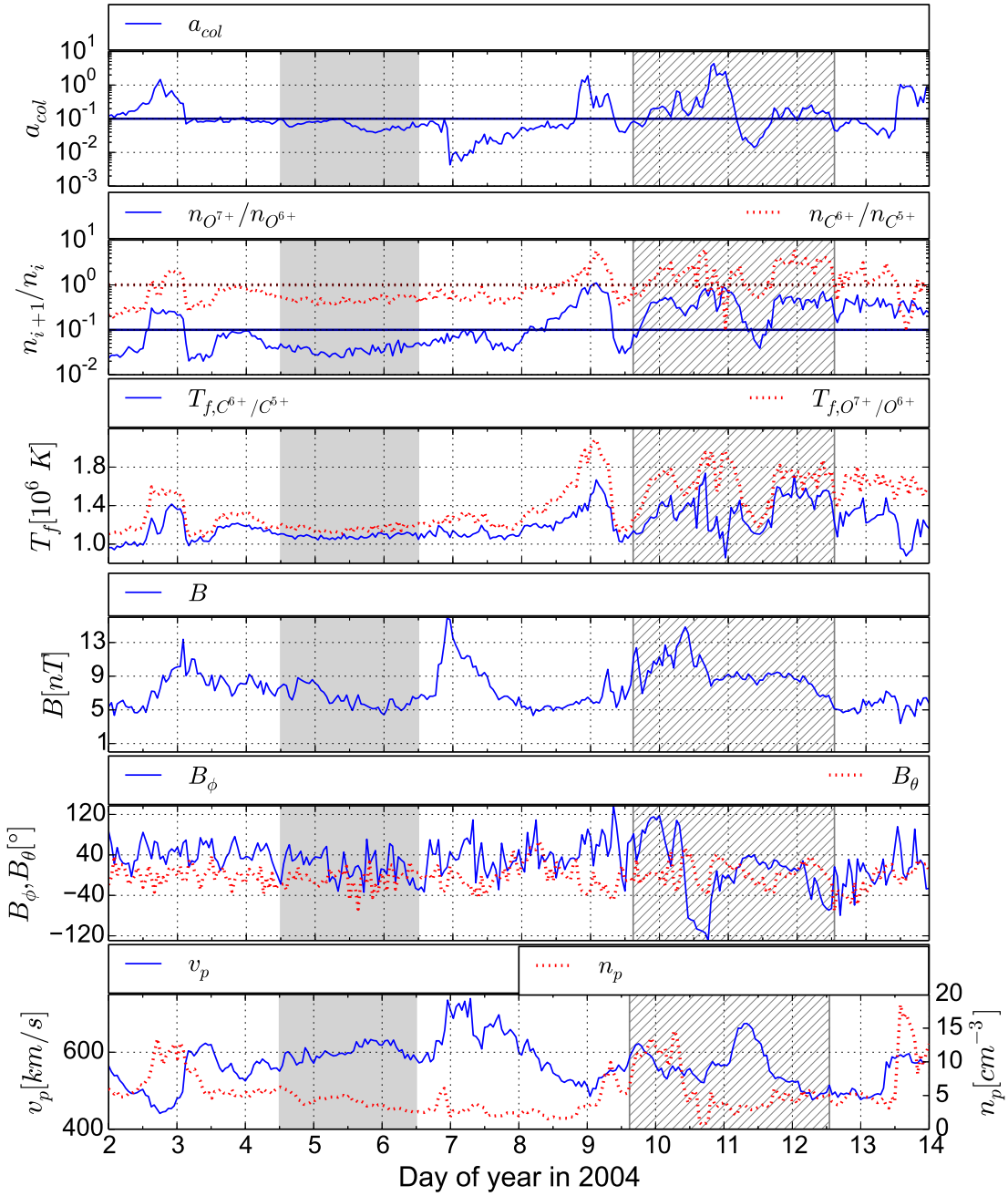

Fig. 2. Solar wind properties for 12 days in 2004. The collisional age $a_{\rm col}$ is displayed in the *first panel*. The *second panel* shows the density ratios $n_{\rm O^{7+}}/n_{\rm O^{6+}}$ and $n_{\rm C^{6+}}/n_{\rm C^{5+}}$. The horizontal lines in the *first two panels* indicate the respective selection thresholds for $a_{\rm col} = 0.1$, $n_{\rm C^{6+}}/n_{\rm C^{5+}} = 1$, and $n_{\rm O^{7+}}/n_{\rm O^{6+}} = 0.1$. The *third panel* contains the freeze-in temperatures T_f corresponding to the ion density ratios $n_{\rm O^{7+}}/n_{\rm O^{6+}}$ and $n_{\rm C^{6+}}/n_{\rm C^{5+}}$. The *fourth panel* gives the magnitude of the magnetic field B and the azimuthal (B_ϕ) and polar (B_θ) angles of the magnetic field are shown in the *fifth panel*. The *sixth panel* shows the solar-wind proton speed (*left* y-axis) and proton density (*right* y-axis) as measured by SWEPAM. All data products are displayed with 1h time resolution. The gray shaded area marks a pure coronal-hole-wind stream, while the hatched area highlights an ICME.

Figure 5 shows observations for a solar wind stream in 2006 which exhibits a transition from Fe-cool CH wind to Fe-hot CH wind. In the top panel of Fig. 5, a time series of the charge-state distribution is shown (in the same way as in Fig. 4). An increase of the average Fe charge state is visible at DoY 160.4 thus indicating a transition from Fe-cool coronal-hole wind to Fe-hot coronal-hole wind. The panels below show the solar-wind proton speed, proton density, and the $n_{\rm O^{7+}}/n_{\rm O^{6+}}$ ratio measured at ACE. To allow a direct comparison with the model polarity in Fig. 6, the bottom panel gives additionally the magnetic-field polarity observed with ACE/MAG (Smith et al. 1998) for the same time period. In order to determine the in-situ magnetic-field polarity, we first derive the nominal magnetic-field direction $B_\phi^{\rm nom}$, that is, the angle between the field line and the radial direction: $B_\phi^{\rm nom} = \arccos\left(\sqrt{\frac{1}{1+(\omega r \sin(\theta)/v_{\rm p})^2}}\right)$. Here, ω is the solar angular velocity, r is the Sun-spacecraft distance, θ is the heliographic latitude and $v_{\rm p}$ is the in-situ solar-wind proton speed. Next, we subtract the nominal magnetic field angle $B_\phi^{\rm nom}$ from the in-situ measured angle B_ϕ. If the absolute difference is greater than 90 deg, the magnetic-field polarity is inwardly (⊗, red) directed; otherwise it is outwardly (⊙, green) directed. A switch from outwardly

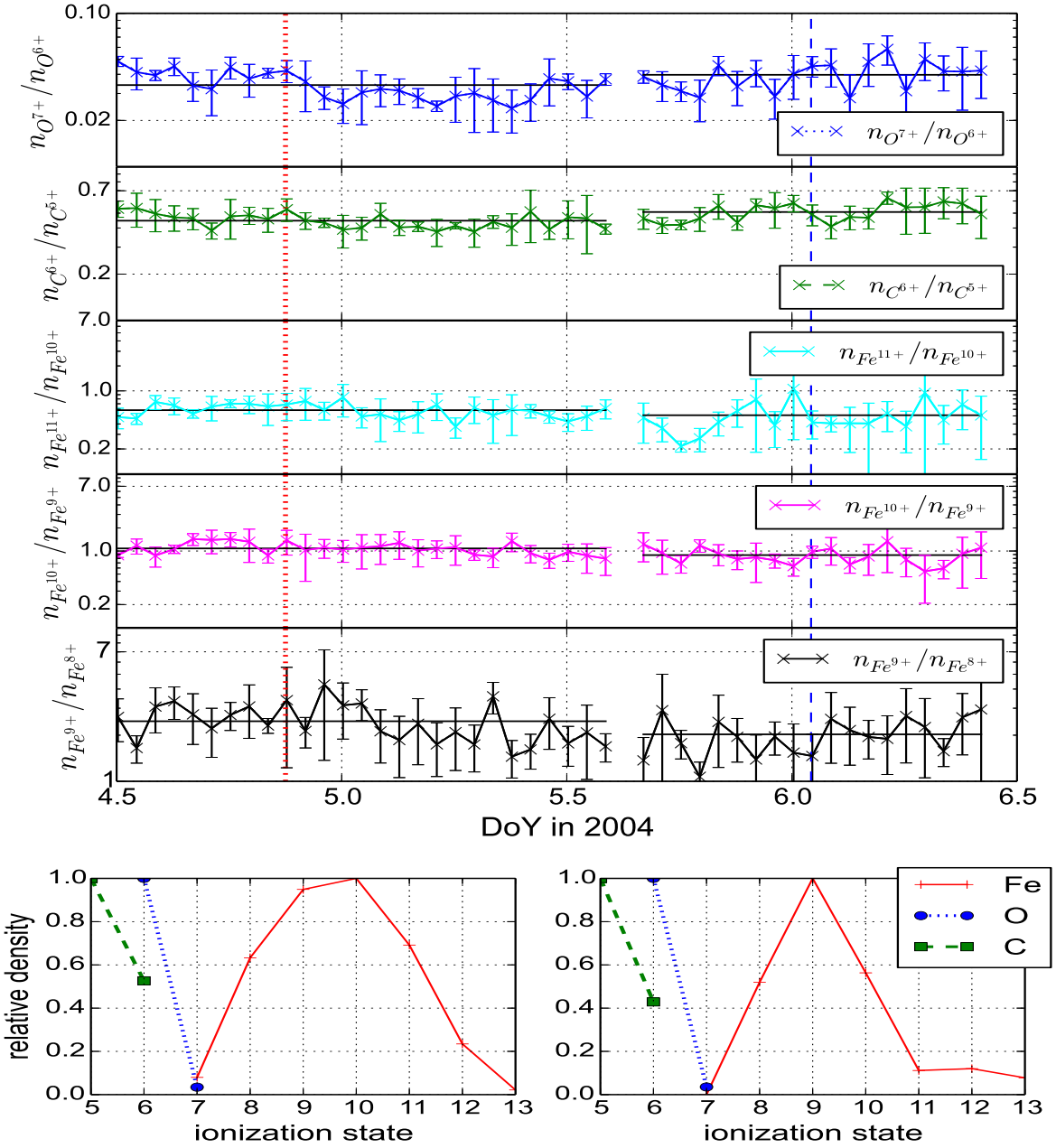

Fig. 3. Ion density ratios for the highlighted part of the coronal-hole-wind stream from Fig. 2. The *five top panels* show the density ratios of ion pairs, namely $n_{O^{7+}}/n_{O^{6+}}$, $n_{C^{6+}}/n_{C^{5+}}$, $n_{Fe^{11+}}/n_{Fe^{10+}}$, $n_{Fe^{10+}}/n_{Fe^{9+}}$, $n_{Fe^{9+}}/n_{Fe^{8+}}$. Each curve is divided into two parts. This partition is based on the mean Fe charge-state as illustrated in Fig. 4. The horizontal lines in each panel give the mean density ratio in the *left and right* interval, respectively. The vertical lines in the *five top panels* indicate the points in times for which examples of charge-state distributions normalized to the maximum density for C, O, and Fe are shown in the *bottom panel*. The dotted line corresponds to the *left bottom panel* and the dashed line to the *right panel*. (Although C^{4+} is more abundant than C^{6+} it is omitted here because it tends to be contaminated with adjacent O ions in ACE/SWICS.) Each data point represents a one-hour average and the error bars reflect the error from the counting statistics.

pointing (i.e. ⊙, green) polarity to inwardly pointing polarity (i.e. ⊗, red) occurs at DoY 157.3. From DoY 157.3 onwards, the polarity remains inwardly pointing (⊗, red) with some exceptions. We verified that the exceptions are caused by kinks in the magnetic field which can be seen by a reversal of the ion-proton differential streaming (Berger et al. 2011). In particular, the polarity does not change on DoY 160 which includes the transition from Fe-cool coronal-hole wind to Fe-hot coronal-hole wind.

With a combination of ballistic back-mapping and a potential field source surface (PFSS, Schatten et al. 1969; Altschuler & Newkirk 1969) model, the photospheric source region of the ACE observations from DoY 158−163 can be estimated. Based on the in-situ solar wind speed, the solar rotation, and the heliographic coordinates of ACE, the position of ACE in heliographic coordinates is mapped back to the source surface. Here, a simple PFSS model takes over and allows us to track the field lines down to the photosphere. A uniform grid with 1° resolution is assumed at the source surface. Peleikis et al. (2015) gives a more detailed description of the method applied here. The accuracy of this approach is limited by the varying age of different parts of the underlying magnetograms that are composites of images from 27 days. In the following, this back-mapping is used to test whether the observed coronal-hole wind can be

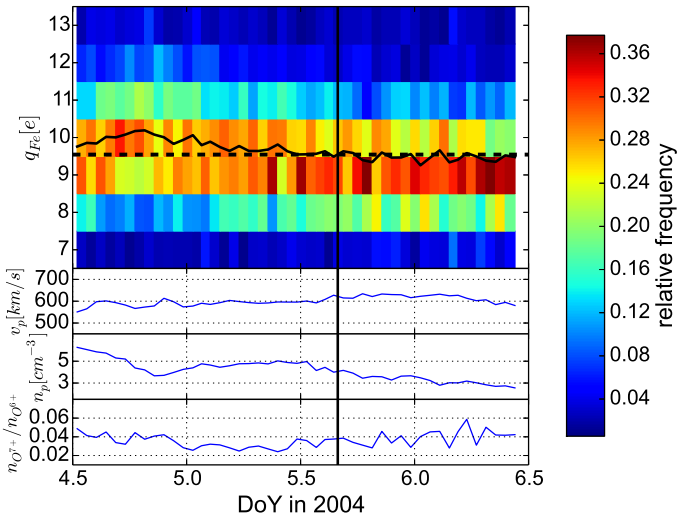

Fig. 4. Time series of Fe charge-state distributions (*first panel*) for the highlighted time period from Fig. 2, that is, DoY 4.5−6.5 in 2004, in one-hour time resolution. In black, the average charge-state (that is, $\tilde{q}_{\mathrm{Fe}} = \sum_{c=7}^{13} c n_{\mathrm{Fe}^{c+}} / \sum_{c=7}^{13} n_{\mathrm{Fe}^{c+}}$) is shown in units of the elementary electric charge e. Each charge-state distribution is normalized to the sum. Below, the solar wind proton speed (*second panel*) and proton density (*third panel*) are given as reference. In the *bottom panel* the ratio $n_{O^{7+}}/n_{O^{6+}}$ is shown as well. The threshold value between Fe-cool and Fe-hot wind is shown as a horizontal dashed line and the transition between Fe-hot and Fe-cool coronal-hole wind is marked with a vertical black line in all panels.

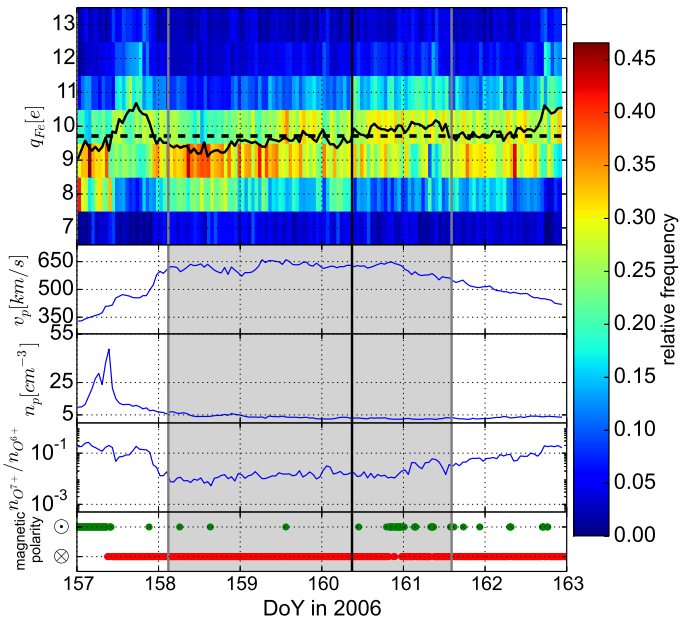

Fig. 5. Time series of the charge-state distributions of Fe for six days in 2006 with a one-hour time resolution and in the same format as in Fig. 4, with an additional panel for the magnetic-field polarity. Here, red indicates inwards pointing polarity (⊗) and green indicates outwards-pointing polarity (⊙).

associated with an open field line region in the photosphere and to investigate what kind of coronal structures are related to the transitions between Fe-cool and Fe-hot coronal-hole wind. Although only parts of the resulting heliographic maps are shown here, we examined the complete Carrington map in each case.

In Fig. 6, each cross in the lower panel represents a footpoint of a magnetic field line mapped back from the source

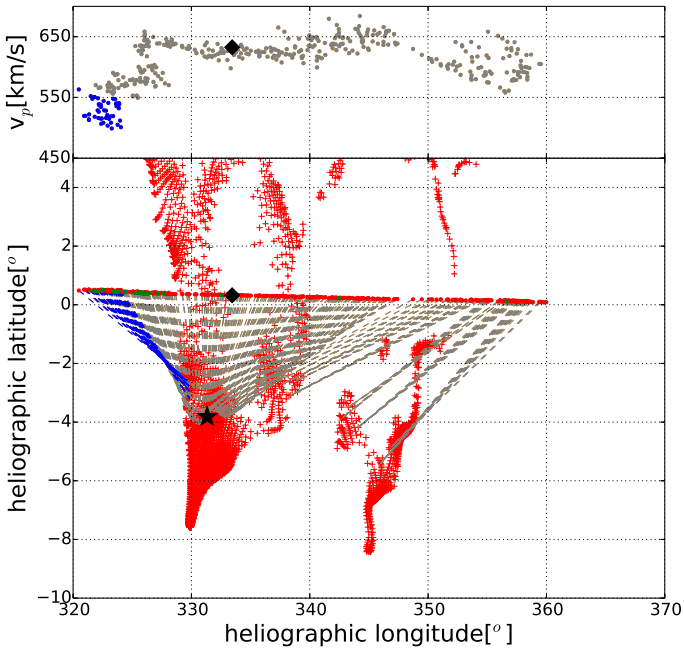

Fig. 6. Section of a heliographic map based on MDI magnetograms for Carrington rotation 2044. The first part of the highlighted part of the stream in Fig. 5 is omitted because it is part of the previous Carrington rotation. The *top panel* shows the solar-wind proton speed (v_{p}) plotted against the mapped back heliographic longitude on the source surface. Below, the dotted line shows the corresponding footpoints of ACE for DoY 158.4−162 on the source surface in heliographic coordinates. The color of each footpoint on the source surface corresponds to the magnetic-field polarity observed at ACE. The polarity is plotted in 12-min time resolution. These footpoints are then traced down to the photosphere with a PFSS model. The dashed lines connect the positions of the ACE footpoints on the source surface to the corresponding footpoints on the photosphere. Footpoints of open field lines in the photosphere are indicated with + symbols (red). The transition between the Fe-hot coronal-hole wind and the Fe-cool coronal-hole wind is marked with a black diamond on the source surface (and in the *first panel*) and with a black star on the photosphere.

surface down to the photosphere. Additionally for the corresponding Carrington rotation 2044, the footpoints of ACE are shown over this Carrington map derived from a PFSS model based on magnetograms from the Michelson Doppler Imager (MDI, Scherrer et al. 1991) on the Solar and Heliospheric Observatory (SOHO). Figure 6 shows only the area to which the observations in the stream of interest in Fig. 5 are mapped back by the PFSS model. This area is an extension of the northern polar coronal hole to equatorial regions with – according to the PFSS model – red, inwardly pointing polarity. The dashed lines connecting the footpoints on the source surface and the photosphere corresponding to the coronal-hole-wind stream from DoY 158.12−161.59 are colored gray and the start of the subsequent declining phase of the stream (DoY 161.59−162) is colored blue. The border between the Fe-cool coronal-hole wind and the Fe-hot coronal-hole wind is indicated with a black diamond on the source surface and with a black star on the photosphere. The beginning of the period of interest belongs to the preceding Carrington rotation. Thus, for mapping the corresponding footpoints a different Carrington map would need to be considered. Since the transition itself occurs later in the stream and for the sake of clarity this first part of the stream is therefore omitted in Fig. 6. The remaining part of the coronal-hole-wind stream of interest, including the transition between the Fe-cool and the

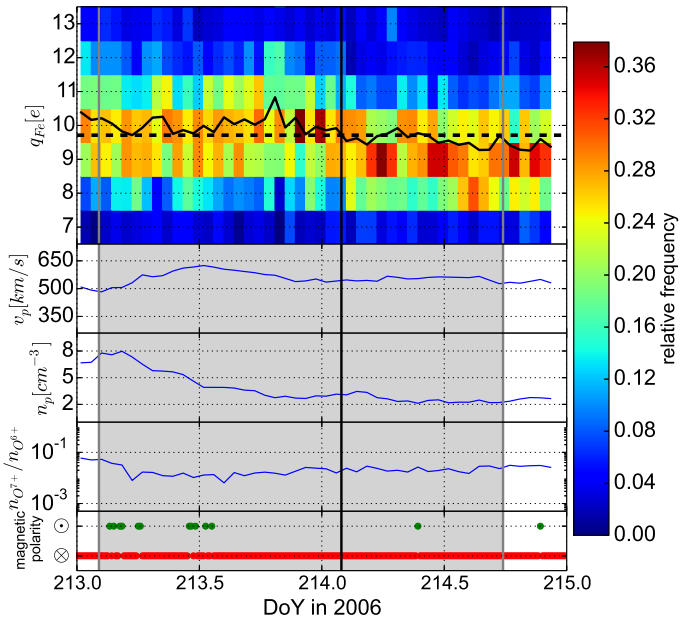

Fig. 7. Time series of the charge-state distributions of Fe for two days in 2006, with a one-hour time resolution (*first panel*) in the same format as in Fig. 5.

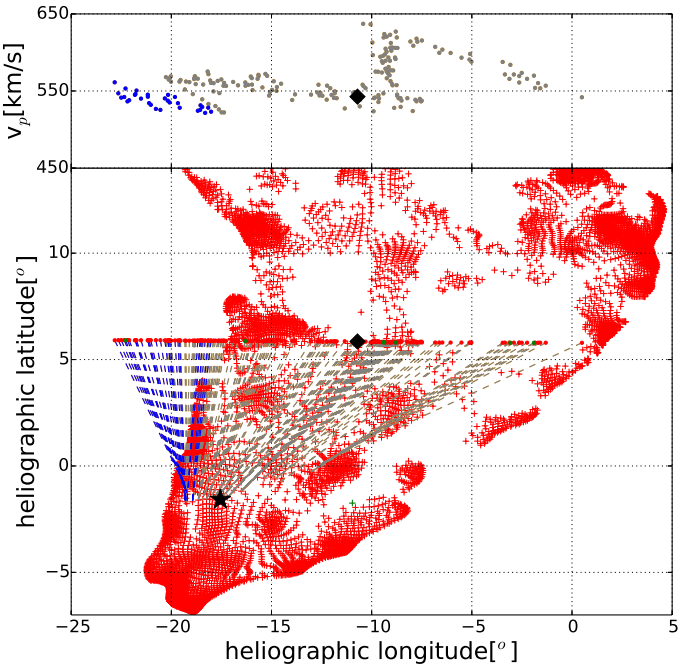

Fig. 8. A section of a heliographic map based on an MDI magnetogram for Carrington rotation 2046. The format is the same as in Fig. 6.

Fe-hot stream, and the following stream are mapped to a small scale region with open field lines in the equatorial region which is, as we verified on the complete Carrington map, connected to the northern polar coronal hole. For the whole time period and in particular, around the transition between the Fe-cool and Fe-hot stream, the in-situ observed polarities match (inwards pointing with the exception of the aforementioned kinks) the polarities predicted by the PFSS model. However, due to the limitations on the accuracy of the back-mapping caused by the requirement to derive the magnetic field lines from a complete Carrington rotation, the possibility that the transition occurs at an edge of this open field line region cannot be ruled out.

A second transition, DoY 213−215 in 2006, in this case from an Fe-hot to an Fe-cool stream, is shown as a charge-state distribution time series in Fig. 7. The Fe-hot part of this stream includes the beginning of the trailing edge of the high-speed stream as defined in Borovsky & Denton (2016). The transition from Fe-cool to Fe-hot wind, however, occurs 12 h earlier and is thus unlikely to be affected by the trailing edge. It is interesting to note that the Fe-hot part of the stream of interest includes faster solar wind than the Fe-cool part of the stream. However, the change in solar wind speed occurs >5 h earlier than the transition from Fe-hot to Fe-cool wind. Since the transition boundary is defined on four-hour averages, shifting the temporal bins cannot make the two changes coincide exactly but they might be closer, as it appears here. As shown in Fig. 8, which provides a part of the photospheric map for the relevant Carrington rotation 2046, the transition between the Fe-hot and Fe-cool coronal-hole-wind streams is situated within a larger region (compared to the case in Fig. 6) of open field lines. Inspection of the heliographic map for the complete Carrington rotation (not shown here) indicates that this region was not connected to a polar coronal-hole. In the following, we refer to such a region of open field lines which is not connected to a polar coronal-hole as isolated. Within the accuracy of the back-mapping approach, the transition lies within a region of open field lines. However, within this region, the field line density is not uniform; for example west of the transition (to the right of the star in Fig. 8) the field line density is decreasing at the photosphere. This fine-structure could be related to the transition. The in-situ magnetic polarity again matches the polarity predicted by the PFSS model with a few exceptions that can be explained as kinks in the magnetic field as well. For both transition examples in Figs. 6 and 8, both streams, in particular also the Fe-hot stream, originate in the equatorial region.

Table 1 summarizes the properties of eight transitions in 2006. The first column gives the start and end times of the part of the coronal-hole-wind stream containing the transition in DoY and the corresponding Carrington rotation is noted in the second column. An $*$ in the first column indicates the transitions shown in Figs. 5−8. The transition time is listed in the third column. To indicate the latitudinal and longitudinal position of the back-mapped foot points of each coronal-hole-wind stream, the highest and lowest back-mapped foot point is given in heliographic latitude in the fourth column, and the respective heliographic longitude in the fifth column. The last column indicates whether the stream is mapped to an isolated open field line region or whether the corresponding open field line region is connected to the northern polar coronal-hole (NPCH). All these coronal-hole-wind streams have inwardly pointing magnetic polarity as indicated by the symbol ⊗ in the last column. All eight transitions are mapped back to low latitudes and the longitudinal spread is at most 18°. As listed in Table 1, four out of eight transitions between Fe-cool and Fe-hot coronal-hole wind in 2006 were mapped back to isolated coronal holes in the equatorial region. The remaining three transitions were observed in the equatorial region as well, but the respective coronal holes were connected to the northern polar coronal-hole. With respect to the long-term behavior, Zhao & Landi (2014) observed that wind from polar coronal holes is predominantly Fe-hot, while equatorial coronal-hole wind is predominantly Fe-cool. The case study shown here illustrates that, independently of their connection to a polar coronal-hole, Fe-hot coronal-hole-wind streams are hidden within the mainly Fe-cool equatorial coronal-hole wind.

A possible explanation for the change in the Fe charge states at transitions between Fe-cool and Fe-hot coronal-hole wind is

Table 1. Eight transitions between Fe-cool and Fe-hot coronal-hole-wind streams in 2006.

Stream of interest [DoY in 2006]	CR	Transition time [DoY in 2006]	Latitude [°]			Longitude [°]			Isolated or connected
51.6–53.2	2040	51.4	−10.8	to	−5.7	320.2	to	331.6	⊗ isolated
104.9–107.0	2042	105.7	−5.0	to	−4.0	317.5	to	320.9	⊗ connected to NPCH
131.5–134.4	2043	133.4	−7.7	to	−2.9	326.7	to	343.9	⊗ connected to NPCH
∗ 158.1 – 161.6	2044	160.4	−5.4	to	−2.4	329.8	to	348.5	⊗ connected to NPCH
186.2–188.1	2045	187.4	−4.9	to	−1.4	331.1	to	343.5	⊗ connected to NPCH
∗ 213.1–214.5	2046	214.1	−1.7	to	−2.9	341.0	to	351.7	⊗ isolated
240.1–241.7	2047	241.0	−0.1	to	3.6	354.4	to	3.3	⊗ isolated
294.0–296.0	2049	295.0	5.2	to	5.7	4.9	to	5.7	⊗ isolated

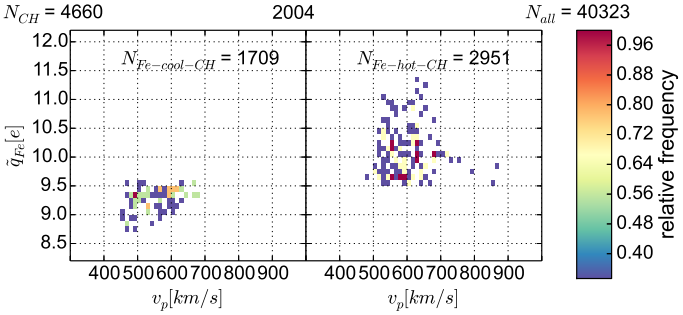

Fig. 9. Average charge-state ($\tilde{q}_{\rm Fe}$) versus solar wind proton speed for Fe-cool and Fe-hot coronal-hole type wind for 2004. The color gradient indicates the frequency of observing each charge-state-solar wind speed pair in 2004 and is normalized to the maximum in each panel. Each data point represents a four-hour average. The inset in each panel gives the number of data points in 12-min resolution that contributed to the averages in in this figure. The number ($N_{\rm all}$) of all 12-min resolution data points in 2004 is given on the top right and the number ($N_{\rm CH}$) of all data points categorized as pure coronal-hole wind, in the *top left*.

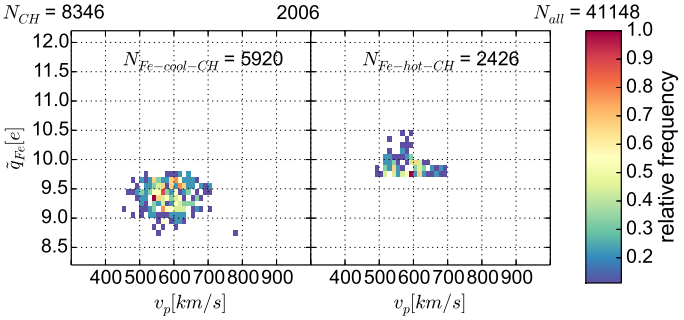

Fig. 10. Average charge-state ($\tilde{q}_{\rm Fe}$) versus solar wind proton speed for Fe-cool and Fe-hot coronal-hole wind for 2006 in the same format as in Fig. 9.

that they coincide with stream interfaces between two distinct coronal-hole-wind streams. This is supported by the coinciding increase in solar wind speed and the decrease in proton density $n_{\rm p}$ in the 2004 example in Fig. 4. However, in Figs. 5 and 7, no clear change in the proton density $n_{\rm p}$ is visible at the transition. Furthermore, although the average solar wind speeds in the DoY 213–215 example in 2006 differ before and after the transition, the change in the solar wind speed does not coincide with the transition but occurs more than five hours earlier. Within the accuracy of the back-mapping approach, the back-mapped positions of the transitions in Figs. 6 and 8 might be consistent with stream interfaces at the transition times but this is not conclusive. Therefore, this explanation can neither be proved nor ruled out by the observations here.

To put the case studies presented above into some perspective, Figs. 9 and 10 illustrate how frequently Fe-cool and Fe-hot coronal-hole-wind streams were observed in 2004 and 2006, respectively. Figure 9 shows the frequency of the average charge-state versus the solar wind proton speed for all Fe-cool coronal-hole wind in 2004 (left panel) and all Fe-hot coronal-hole wind in 2004 (right panel). The inset in each panel indicates the number of data points in 12-min resolution of Fe-cool ($N_{\rm Fe\text{-}cool-CH}$) and Fe-hot coronal-hole wind ($N_{\rm Fe\text{-}hot-CH}$) included in each panel. For reference, the number $N_{\rm all}$ of all 12-min resolution data points in 2004 is given on the top right and the number $N_{\rm CH}$ of all data points categorized as pure coronal-hole wind in the top left. In the same way, Fig. 10 shows Fe-cool and Fe-hot coronal-hole wind for the year 2006. With respect to the solar wind speed, the distributions of both the Fe-cool and Fe-hot components of the coronal-hole wind overlap to a large extent in both years. In particular in 2004, the Fe-cool component contains slower solar wind than the Fe-hot component and the overlap is smaller than in 2006. The question under which conditions each type of coronal-hole wind is prevalent in other years is left for a later study. However, comparing the years 2004 (Fig. 9) and 2006 (Fig. 10) allows some observations. Firstly, while in 2004, 1709 individual observations can be identified as Fe-cool coronal-hole wind and 2951 as Fe-hot coronal-hole wind, the 2006 data contains 5920 Fe-cool coronal-hole wind observations and 2426 Fe-hot coronal-hole wind observations. This illustrates that in 2004 the Fe-hot wind is more frequent than the Fe-cool coronal-hole wind. In 2006, however, the opposite is the case: Fe-cool coronal-hole wind is more frequent than Fe-hot coronal-hole wind. Secondly, not only does the frequency of each wind type change but the Fe-hot coronal-hole wind is less variable in its average Fe charge state and the overall average Fe charge states are lower in 2006 than in 2004. (Although not shown here, this effect is not only visible for Fe but also for O.) Both observations hint at a solar-cycle dependence as observed for O and C in Kasper et al. (2012), Schwadron et al. (2011). Additionally, an overall drop of O and C charge states as observed in 2006, at the transition to the long solar minimum at the end of solar cycle 23 (e.g. Lepri et al. 2013; Richardson 2014), is probably superimposed on the Fe charge-state distribution as well. This aspect requires further investigation.

The 2004 data in Fig. 9 exhibits an interesting feature with respect to a possible solar-wind proton speed dependence of the average Fe charge state. The average Fe charge state of the Fe-cool component (left panel) of the coronal-hole wind shows a possible dependence on the solar-wind speed. However, this is

not visible in the Fe-hot component in the right panel which instead manifests a larger variability in the average Fe charge state for each solar-wind speed. For the 2006 example, this feature is not visible.

4. Conclusions

Complementing the observations of the long-term behavior of the Fe charge states in von Steiger et al. (2000), Galvin et al. (2009), Richardson (2014), Lepri et al. (2013), Kasper et al. (2012), Schwadron et al. (2011), Zhao & Landi (2014), we present a case-study of individual solar-wind streams that can be clearly identified as coronal-hole wind, with either high or low Fe charge states compared to the charge states in slow solar wind. Streams with either property occur in the same year and we also observe direct transitions between them. This indicates that the steady coronal-hole wind is less uniform in terms of Fe charge states than with respect to O and C charge states. In particular, solar-wind streams with high Fe charge states are Fe-hot and C/O-cool at the same time. Under the assumption that the charge-state distribution is frozen-in in the corona, a higher Fe charge state implies a higher freeze-in temperature for the same cool O freeze-in temperature and thus, a qualitatively different temperature profile in the corona.

The back-mapping of transitions between Fe-cool and Fe-hot coronal-hole-wind streams finds the origin of both streams in equatorial regions and close to each other. Thus, streams with consistently high or low Fe charge states can originate in the same region. A more systematic investigation of the origin of all individual Fe-hot and Fe-cool coronal-hole-wind streams is beyond the scope of this case-study. In addition, we have seen that in 2004 Fe-hot coronal-hole wind is more frequent, while in 2006 Fe-cool coronal-hole wind is predominantly observed. A possible solar-cycle dependence of the frequency of Fe-hot and Fe-cool coronal-hole wind – as it has been observed for O and C in Schwadron et al. (2011) and for Fe as well over solar cycle 23 in Lepri et al. (2013) – is one possibility to explain the changes in the frequency of Fe-hot and Fe-cool coronal-hole wind between 2004 and 2006. The details of a solar-cycle dependence, the evolution of the respective coronal structures over consecutive Carrington rotations, and the implications of these observations for the temperature profile in coronal holes require further investigation.

Acknowledgements. Part of this work was supported by the Deutsche Forschungsgemeinschaft (DFG) project number Wi-2139/10-1. We very gratefully acknowledge the diligent work of the anonymous referee who provided very detailed and helpful suggestions and comments.

References

Altschuler, M. D., & Newkirk, G. 1969, Sol. Phys., 9, 131
Berger, L. 2008, Ph.D. Thesis, Kiel, Christian-Albrechts-Universität
Berger, L., Wimmer-Schweingruber, R., & Gloeckler, G. 2011, Phys. Rev. Lett., 106, 151103
Borovsky, J. E., & Denton, M. H. 2016, J. Geophys. Res.: Space Phys., 121, 5055
Dere, K., Landi, E., Mason, H., Fossi, B. M., & Young, P. 1997, A&AS, 125, 149
Galvin, A., Popecki, M., Simunac, K., et al. 2009, Ann. Geophys, 27, 3909
Gloeckler, G., Cain, J., Ipavich, F., et al. 1998, in The Advanced Composition Explorer Mission (Springer), 497
Gopalswamy, N., Yashiro, S., Michalek, G., et al. 2009, Earth, Moon, and Planets, 104, 295
Jian, L., Russell, C., Luhmann, J., & Skoug, R. 2006, Sol. Phys., 239, 393
Jian, L., Russell, C., & Luhmann, J. 2011, Sol. Phys., 274, 321
Kasper, J., Lazarus, A., & Gary, S. 2008, Phys. Rev. Lett., 101, 261103
Kasper, J., Stevens, M., Korreck, K., et al. 2012, ApJ, 745, 162
Ko, Y.-K., Fisk, L. A., Geiss, J., Gloeckler, G., & Guhathakurta, M. 1997, Sol. Phys., 171, 345
Landi, E., Young, P., Dere, K., Del Zanna, G., & Mason, H. 2013, ApJ, 763, 86
Lepri, S., Landi, E., & Zurbuchen, T. 2013, ApJ, 768, 94
Marsch, E. 2006, Liv. Rev. Sol. Phys., 3, 1
McComas, D., Bame, S., Barker, P., et al. 1998, in The Advanced Composition Explorer Mission (Springer), 563
Peleikis, T., Kruse, M., Berger, L., Drews, C., & Wimmer-Schweingruber, R. F. 2015, in Solar Wind 14: Proc. of the fourteenth international Solar wind Conf., AIP Conf. Proc., 1720, 020003
Richardson, I. 2014, Sol. Phys., 289, 3843
Richardson, I., & Cane, H. 2010, Sol. Phys., 264, 189
Schatten, K., Wilcox, J., & Ness, N. 1969, Sol. Phys., 6, 442
Scherrer, P., Hoeksema, J., & Bush, R. 1991, Adv. Space Res., 11, 113
Schwadron, N., Smith, C., Spence, H. E., et al. 2011, ApJ, 739, 9
Smith, C. W., L'Heureux, J., Ness, N. F., et al. 1998, in The Advanced Composition Explorer Mission (Springer), 86, 613
Tu, C., Zhou, C., Marsch, E., et al. 2005, Science, 308, 519
von Steiger, R. V., Schwadron, N., Fisk, L., et al. 2000, J. Geophys. Res.: Space Phys., 105, 27217
Wilhelm, K. 2012, Space Sci. Rev., 172, 57
Yashiro, S., Gopalswamy, N., Michalek, G., et al. 2004, J. Geophys. Res.: Space Phys., 109
Zhao, L., & Fisk, L. 2010, in SOHO-23: Understanding a Peculiar Solar Minimum, ASP Conf. Ser., 428, 229
Zhao, L., & Landi, E. 2014, ApJ, 781, 110
Zhao, L., Zurbuchen, T. H., & Fisk, L. A. 2009, Geophys. Res. Lett., 36, L14104
Zurbuchen, T., Fisk, L., Gloeckler, G., & von Steiger, R. 2002, Geophys. Res. Lett., 29, 66

10

OTHER RELATED PUBLICATIONS

Evolution of an Equatorial Coronal Hole Structure and the Released Coronal Hole Wind Stream: CR 2039-2050

Authors: Heidrich Meisner, V., Peleikis, T., Kruse, M., Berger, L. and Wimmer-Schweingruber, R.F.
Year: 2017
Journal: Astronomy & Astrophysics
See: Heidrich-Meisner et al. (2017)

2D He^{+} Pickup Ion Velocity Distribution Functions: STEREO PLASTIC Observations

Authors: Drews, C., Berger, L, Taut, A., Peleikis, T. and Wimmer-Schweingruber, R.F.
Year: 2015
Journal: Astronomy & Astrophysics
See: Drews et al. (2015)

Spatially Resolved Charge-State and Current-Density Distributions at the Extraction of an Electron Cyclotron Resonance Ion Source

Authors: Panitzsch, L., Peleikis, T., Stalder, M. and Wimmer-Schweingruber, R.F.
Year: 2011
Journal:Review of Scientific Instruments
See: Panitzsch et al. (2011)

Current Sensity Distributions and Sputter Marks in Electron Cyclotron Resonance Ion Sources

Authors: Panitzsch, L., Peleikis, T., Stalder, M. and Wimmer-Schweingruber, R.F.
Year: 2013
Journal:Review of Scientific Instruments
See: Panitzsch et al. (2013)

11 ULYSSES/SWICS ION POSITIONS

In this chapter the positions of O^{6+}, O^{7+}, C^{5+} and C^{6+} in the Ulysses/SWICS et-matrices are listed. As discussed in section 4.3, the ion positions have been translated from ACE/SWICS to Ulysses/SWICS. The first column of the following tables gives the E/q step, the second the E/q value, the third t_{ToF}, the fourth E_{res}, the fifth σ of the Gaussian distribution of t_{ToF} and the sixth σ of the Gaussian distribution of E_{res}. Except for the second columns all units are channel numbers.
The conversion has been made for all ions in the SWICS et-matrices are group internally available at data/etph/peleikis/Ulysses/tables or on request at peleikis@phyisk.uni-kiel.de or wimmer@phyisk.uni-kiel.de.

E/q step	E/q[keV]	t_{ToF}	E_{res}	σ_{ToF}	σ_E
0	60.5078	214.2624	153.6153	7.7017	3.7279
1	56.3162	219.6552	145.0610	7.7000	3.7400
2	52.4150	225.0839	137.1423	7.6886	3.7532
3	48.7840	230.5411	129.8154	7.6800	3.7600
4	45.4046	236.0160	123.0310	7.6813	3.7583
5	42.2592	241.5006	116.7122	7.6800	3.7600
6	39.3318	246.9841	110.8056	7.6690	3.7711
7	36.6071	252.4578	105.3172	7.6600	3.7800
8	34.0712	257.9105	100.2461	7.6601	3.7796
9	31.7110	263.3332	95.5573	7.6600	3.7800
10	29.5142	268.7148	91.2152	7.6524	3.7885
11	27.4697	274.0463	87.1935	7.6400	3.8000
12	25.5667	279.3172	83.4695	7.6273	3.8101
13	23.7956	284.5186	80.0217	7.6200	3.8200
14	22.1472	289.6405	76.8292	7.6200	3.8308
15	20.6130	294.6748	73.8690	7.6200	3.8400
16	19.1851	299.6126	71.1235	7.6141	3.8475
17	17.8561	304.4468	68.5877	7.6000	3.8600
18	16.6191	309.1700	66.2336	7.5800	3.8800
19	15.4678	313.7759	63.9929	7.5600	3.9000
20	14.3963	318.2583	61.9092	7.5400	3.9200
21	13.3990	322.6126	59.9789	7.5400	3.9400
22	12.4708	326.8342	58.1901	7.5000	3.9800
23	11.6069	330.9202	56.5323	7.4800	4.0000
24	10.8029	334.8674	54.9955	7.4600	4.0400
25	10.0545	338.6741	53.5708	7.4400	4.0600
26	9.3580	342.3391	52.2496	7.4200	4.1000
27	8.7097	345.8607	51.0247	7.3800	4.1400
28	8.1064	349.2395	49.8888	7.3600	4.1800
29	7.5448	352.4772	48.8347	7.3200	4.2200
30	7.0222	355.5742	47.8567	7.3000	4.2600
31	6.5357	358.5333	46.9490	7.2600	4.3200
32	6.0830	361.3556	46.1067	7.2200	4.3800
33	5.6616	364.0443	45.3248	7.1800	4.4200
34	5.2694	366.6019	44.5988	7.1400	4.5000
35	4.9044	369.0315	43.9251	7.1000	4.5600
36	4.5646	371.3379	43.2992	7.0400	4.6400
37	4.2484	373.5244	42.7180	7.0000	4.7200
38	3.9541	375.5946	42.1782	6.9400	4.8000
39	3.6802	377.5531	41.6768	6.9000	4.8800
40	3.4252	379.4037	41.2111	6.8400	4.9800
41	3.1880	381.1517	40.7781	6.7800	5.0800
42	2.9671	382.8002	40.3732	6.7200	5.2000
43	2.7616	384.3546	39.9906	6.6600	5.3200
44	2.5703	385.8184	39.6350	6.5800	5.4600
45	2.3922	387.1958	39.3046	6.5200	5.6000
46	2.2265	388.4916	38.9974	6.4400	5.7600
47	2.0723	389.7099	38.7119	6.3600	5.9200
48	1.9287	390.8533	38.4466	6.2800	6.1000
49	1.7951	391.9272	38.1998	6.2000	6.3000
50	1.6708	392.9352	37.9703	6.1200	6.5001
51	1.5550	393.8795	37.7572	6.0400	6.7200
52	1.4473	394.7653	37.5588	5.9400	6.9600
53	1.3470	395.5947	37.3745	5.7601	7.4798
54	1.2537	396.3719	37.2028	5.5800	8.0999
55	1.1669	397.0997	37.0431	5.3799	8.8203
56	1.0860	397.7797	36.8949	5.1801	9.6596
57	1.0108	398.4166	36.7568	4.9600	10.6400
58	0.9408	399.0122	36.6286	4.7599	11.7804
59	0.8756	399.5683	36.5092	4.5600	13.0798
60	0.8150	400.0880	36.3981	4.3402	14.5986
61	0.7585	400.5742	36.2948	4.1400	16.3801
62	0.7060	401.0284	36.1985	3.9198	18.4621
63	0.6570	401.4514	36.1093	3.7401	20.8773

Table 7: Ion: O^{6+}

E/q step	E/q[keV]	t_{ToF}	E_{res}	σ_{ToF}	σ_E
0	60.5078	199.0116	183.0367	7.1232	4.5196
1	56.3162	203.9741	172.8476	7.1200	4.5200
2	52.4150	208.9698	163.4406	7.1082	4.5276
3	48.7840	213.9918	154.7457	7.1000	4.5400
4	45.4046	219.0300	146.6910	7.1014	4.5530
5	42.2592	224.0771	139.2339	7.1000	4.5600
6	39.3318	229.1228	132.3335	7.0887	4.5592
7	36.6071	234.1590	125.9349	7.0800	4.5600
8	34.0712	239.1751	119.9875	7.0812	4.5685
9	31.7110	244.1630	114.4470	7.0800	4.5800
10	29.5142	249.1129	109.2820	7.0691	4.5903
11	27.4697	254.0162	104.4868	7.0600	4.6000
12	25.5667	258.8632	100.0507	7.0600	4.6099
13	23.7956	263.6458	95.9445	7.0600	4.6200
14	22.1472	268.3549	92.1397	7.0529	4.6302
15	20.6130	272.9831	88.6141	7.0400	4.6400
16	19.1851	277.5222	85.3474	7.0257	4.6494
17	17.8561	281.9662	82.3197	7.0200	4.6600
18	16.6191	286.3082	79.5130	7.0200	4.6800
19	15.4678	290.5417	76.9115	7.0000	4.7200
20	14.3963	294.6619	74.4995	6.9800	4.7400
21	13.3990	298.6645	72.2625	6.9600	4.7600
22	12.4708	302.5451	70.1879	6.9400	4.8000
23	11.6069	306.3003	68.2637	6.9200	4.8400
24	10.8029	309.9284	66.4786	6.9000	4.8600
25	10.0545	313.4273	64.7873	6.8800	4.9000
26	9.3580	316.7960	63.2032	6.8600	4.9600
27	8.7097	320.0332	61.7343	6.8200	5.0000
28	8.1064	323.1393	60.3714	6.8000	5.0400
29	7.5448	326.1158	59.1067	6.7800	5.1000
30	7.0222	328.9624	57.9334	6.7400	5.1600
31	6.5357	331.6823	56.8440	6.7200	5.2200
32	6.0830	334.2762	55.8332	6.6800	5.2800
33	5.6616	336.7479	54.8944	6.6400	5.3400
34	5.2694	339.0991	54.0228	6.6000	5.4200
35	4.9044	341.3329	53.2135	6.5600	5.5000
36	4.5646	343.4537	52.4618	6.5200	5.5800
37	4.2484	345.4636	51.7638	6.4800	5.6800
38	3.9541	347.3666	51.1154	6.4200	5.7800
39	3.6802	349.1671	50.5130	6.3800	5.9000
40	3.4252	350.8681	49.9535	6.3200	6.0200
41	3.1880	352.4752	49.4331	6.2800	6.1400
42	2.9671	353.9906	48.9500	6.2200	6.2800
43	2.7616	355.4195	48.5008	6.1600	6.4200
44	2.5703	356.7654	48.0831	6.1000	6.5800
45	2.3922	358.0316	47.6950	6.0200	6.7400
46	2.2265	359.2230	47.3342	5.9600	6.9200
47	2.0723	360.3430	46.9985	5.9000	7.1200
48	1.9287	361.3945	46.6866	5.8200	7.3200
49	1.7951	362.3820	46.3966	5.7400	7.5400
50	1.6708	363.3088	46.1269	5.6600	7.8001
51	1.5550	364.1771	45.8762	5.6000	8.0600
52	1.4473	364.9915	45.6430	5.5200	8.3400
53	1.3470	365.7540	45.4261	5.3401	8.9598
54	1.2537	366.4683	45.2244	5.1600	9.6999
55	1.1669	367.1373	45.0365	4.9799	10.5404
56	1.0860	367.7623	44.8623	4.8001	11.5395
57	1.0108	368.3480	44.6998	4.6000	12.7000
58	0.9408	368.8954	44.5488	4.4199	14.0204
59	0.8756	369.4065	44.4084	4.2200	15.5798
60	0.8150	369.8842	44.2777	4.0402	17.3783
61	0.7585	370.3312	44.1562	3.8400	19.5001
62	0.7060	370.7488	44.0429	3.6598	21.9024
63	0.6570	371.1376	43.9379	3.4602	24.6769

Table 8: Ion: O^{7+}

E/q step	E/q[keV]	t_{ToF}	E_{res}	σ_{ToF}	σ_E
0	60.5078	203.8506	133.8039	7.3378	3.3917
1	56.3162	209.0219	126.5221	7.3400	3.4000
2	52.4150	214.2257	119.7794	7.3431	3.3986
3	48.7840	219.4553	113.5283	7.3400	3.4000
4	45.4046	224.7006	107.7312	7.3286	3.4114
5	42.2592	229.9539	102.3743	7.3200	3.4200
6	39.3318	235.2044	97.4248	7.3202	3.4187
7	36.6071	240.4442	92.7862	7.3200	3.4200
8	34.0712	245.6625	88.3978	7.3124	3.4311
9	31.7110	250.8508	84.2987	7.3000	3.4400
10	29.5142	255.9987	80.5158	7.2872	3.4395
11	27.4697	261.0978	77.0197	7.2800	3.4400
12	25.5667	266.1380	73.7783	7.2804	3.4488
13	23.7956	271.1108	70.7736	7.2800	3.4600
14	22.1472	276.0068	67.9901	7.2728	3.4690
15	20.6130	280.8186	65.4108	7.2600	3.4800
16	19.1851	285.5380	63.0199	7.2457	3.4939
17	17.8561	290.1580	60.8035	7.2400	3.5000
18	16.6191	294.6712	58.7488	7.2400	3.5000
19	15.4678	299.0719	56.8437	7.2200	3.5200
20	14.3963	303.3549	55.0766	7.2000	3.5400
21	13.3990	307.5153	53.4379	7.1800	3.5600
22	12.4708	311.5489	51.9155	7.1600	3.6000
23	11.6069	315.4526	50.4695	7.1400	3.6200
24	10.8029	319.2236	49.1283	7.1200	3.6400
25	10.0545	322.8601	47.8846	7.1000	3.6800
26	9.3580	326.3612	46.7308	7.0800	3.7000
27	8.7097	329.7260	45.6603	7.0400	3.7400
28	8.1064	332.9545	44.6671	7.0200	3.7600
29	7.5448	336.0480	43.7453	6.9800	3.8000
30	7.0222	339.0068	42.8897	6.9600	3.8400
31	6.5357	341.8337	42.0952	6.9200	3.9000
32	6.0830	344.5298	41.3579	6.8800	3.9400
33	5.6616	347.0985	40.6732	6.8400	3.9800
34	5.2694	349.5417	40.0374	6.8000	4.0400
35	4.9044	351.8629	39.4471	6.7600	4.1000
36	4.5646	354.0665	38.8986	6.7200	4.1600
37	4.2484	356.1554	38.3890	6.6800	4.2400
38	3.9541	358.1336	37.9158	6.6200	4.3000
39	3.6802	360.0049	37.4760	6.5800	4.3800
40	3.4252	361.7727	37.0673	6.5200	4.4800
41	3.1880	363.4428	36.6875	6.4600	4.5600
42	2.9671	365.0176	36.3346	6.4000	4.6600
43	2.7616	366.5026	36.0066	6.3400	4.7800
44	2.5703	367.9012	35.7016	6.2800	4.8800
45	2.3922	369.2172	35.4180	6.2000	5.0200
46	2.2265	370.4554	35.1544	6.1400	5.1400
47	2.0723	371.6193	34.9093	6.0600	5.3000
48	1.9287	372.7117	34.6816	6.0000	5.4400
49	1.7951	373.7378	34.4696	5.9200	5.6000
50	1.6708	374.7006	34.2725	5.8400	5.7801
51	1.5550	375.6029	34.0894	5.7600	5.9800
52	1.4473	376.4489	33.9190	5.6800	6.1800
53	1.3470	377.2412	33.7606	5.5001	6.6398
54	1.2537	377.9835	33.6132	5.3200	7.1799
55	1.1669	378.6785	33.4761	5.1199	7.8003
56	1.0860	379.3281	33.3487	4.9401	8.5197
57	1.0108	379.9364	33.2300	4.7400	9.3800
58	0.9408	380.5052	33.1196	4.5399	10.3403
59	0.8756	381.0365	33.0170	4.3400	11.4599
60	0.8150	381.5332	32.9215	4.1402	12.7588
61	0.7585	381.9976	32.8326	3.9400	14.2601
62	0.7060	382.4316	32.7497	3.7398	16.0218
63	0.6570	382.8356	32.6729	3.5402	18.0578

Table 9: Ion: C^{5+}

E/q step	E/q[keV]	t_{ToF}	E_{res}	σ_{ToF}	σ_E
0	60.5078	186.6666	163.7120	6.6894	4.2113
1	56.3162	191.3583	154.9157	6.6800	4.2200
2	52.4150	196.0800	146.6940	6.6775	4.2198
3	48.7840	200.8252	139.0488	6.6800	4.2200
4	45.4046	205.5845	131.9753	6.6833	4.2276
5	42.2592	210.3507	125.4281	6.6800	4.2400
6	39.3318	215.1139	119.3599	6.6683	4.2530
7	36.6071	219.8668	113.7312	6.6600	4.2600
8	34.0712	224.5998	108.5105	6.6613	4.2592
9	31.7110	229.3051	103.6813	6.6600	4.2600
10	29.5142	233.9730	99.2150	6.6491	4.2686
11	27.4697	238.5958	95.0422	6.6400	4.2800
12	25.5667	243.1644	91.1143	6.6400	4.2901
13	23.7956	247.6712	87.4389	6.6400	4.3000
14	22.1472	252.1079	84.0227	6.6329	4.3107
15	20.6130	256.4675	80.8544	6.6200	4.3200
16	19.1851	260.7425	77.9184	6.6057	4.3277
17	17.8561	264.9270	75.1969	6.6000	4.3400
18	16.6191	269.0147	72.6732	6.6000	4.3600
19	15.4678	273.0001	70.3327	6.5800	4.3800
20	14.3963	276.8784	68.1620	6.5600	4.4000
21	13.3990	280.6449	66.1487	6.5400	4.4400
22	12.4708	284.2969	64.2805	6.5200	4.4600
23	11.6069	287.8311	62.5469	6.5000	4.5000
24	10.8029	291.2451	60.9384	6.4800	4.5200
25	10.0545	294.5369	59.4454	6.4600	4.5600
26	9.3580	297.7060	58.0598	6.4400	4.6000
27	8.7097	300.7516	56.7735	6.4200	4.6400
28	8.1064	303.6740	55.5790	6.4000	4.6800
29	7.5448	306.4742	54.4699	6.3600	4.7200
30	7.0222	309.1524	53.4399	6.3400	4.7800
31	6.5357	311.7111	52.4832	6.3000	4.8400
32	6.0830	314.1512	51.5843	6.2800	4.9000
33	5.6616	316.4763	50.7378	6.2400	4.9600
34	5.2694	318.6879	49.9518	6.2000	5.0200
35	4.9044	320.7889	49.2217	6.1600	5.1000
36	4.5646	322.7834	48.5432	6.1200	5.1800
37	4.2484	324.6740	47.9132	6.0800	5.2600
38	3.9541	326.4644	47.3276	6.0400	5.3400
39	3.6802	328.1583	46.7834	6.0000	5.4400
40	3.4252	329.7587	46.2779	5.9400	5.5400
41	3.1880	331.2706	45.8077	5.9000	5.6600
42	2.9671	332.6963	45.3710	5.8400	5.7800
43	2.7616	334.0407	44.9648	5.7800	5.9000
44	2.5703	335.3068	44.5873	5.7200	6.0400
45	2.3922	336.4979	44.2364	5.6600	6.2000
46	2.2265	337.6186	43.9102	5.6000	6.3600
47	2.0723	338.6720	43.6065	5.5400	6.5200
48	1.9287	339.6609	43.3246	5.4600	6.7200
49	1.7951	340.5896	43.0622	5.4000	6.9200
50	1.6708	341.4613	42.8181	5.3200	7.1401
51	1.5550	342.2781	42.5914	5.2600	7.3600
52	1.4473	343.0441	42.3802	5.1800	7.6200
53	1.3470	343.7614	42.1841	5.0201	8.1798
54	1.2537	344.4335	42.0014	4.8600	8.8399
55	1.1669	345.0626	41.8315	4.6799	9.6003
56	1.0860	345.6509	41.6735	4.5001	10.4596
57	1.0108	346.2016	41.5266	4.3200	11.4800
58	0.9408	346.7168	41.3898	4.1399	12.6404
59	0.8756	347.1975	41.2626	3.9600	13.9998
60	0.8150	347.6470	41.1443	3.7802	15.5985
61	0.7585	348.0676	41.0342	3.6000	17.4201
62	0.7060	348.4604	40.9317	3.4198	19.5421
63	0.6570	348.8260	40.8365	3.2601	21.9973

Table 10: Ion: C^{6+}

ACKNOWLEDGMENTS

An erster Stelle möchte ich mich bei Prof. Dr. R.F. Wimmer-Schweingruber für die sehr gute Betreuung und die Möglichkeit, diese Arbeit überhaupt anzufertigen bedanken.
Dipl.-Physiker Martin Kruse danke ich für die fruchtbare wissenschaftliche Zusammenarbeit und insbesondere für das PFSS Modell, ohne das diese Arbeit in dieser Form nicht möglich gewesen wäre. Ganz besonders möchte ich mich bei Dr. Lars Berger für die wissenschafliche Betreuung und die vielen Diskussionen über viele Aspekte dieser Arbeit bedanken. Dr. Verena Heidrich-Meisner danke ich ebenfalls für die Diskussionen und das sehr kritische Korrekturlesen. Außerdem danke ich natürlich der Sonnenwindgruppe für die vielen Anregungen und Denkanstöße. Desweiteren bedanke ich mich bei Dr. Lauri Panitzsch und Christiane Helmke für die Zusammenarbeit im Sonnenwindlabor. Stefan Kolbe danke ich für die vielen technischen Zeichnungen und das technische Know How.
In diesem Sinne möchte ich mich bei allen Mitarbeitern der Arbeitsgruppe Wimmer dafür bedanken, dass sie so ein großartiges Team sind. Im speziellen möchte ich Dr. Christian Drews und Dipl.-Physiker Christoph Terasa danken für viele anregende Gespräche über Wissenschaft und Freizeit. Dr. Nina Dresing danke ich für die wunderbare Atmosphäre im Büro und viele Diskussionen. Meinen anderen Korrekturlesern danke ich für das kritische und konstruktive Lesen meiner Arbeit. Und ganz besonders danke ich für den vielen Schabernack, der abseits der Arbeit getrieben wurde und gezeigt hat, dass wir mehr als Kollegen sind. Dazu gehört: Wine&Cheese Tasting, Brettspiele, Eve Online, Pantomime, Magic, Hots, die Kochgruppe, Pen&Paper, StarCraft, Lans, PyBomber, Kompost und der ganze Rest.
Aber es gibt auch ein Leben neben der Arbeit. Ich danke ganz herzlich meinen Eltern Marie und Peter Peleikis. Außerdem meinen Freunden von damals, die bis auf einen keine Physiker sind. Und zuletzt und am wichtigsten danke ich der wunderbaren Mirl Trösch.

EIDESTATTLICHE ERKLÄRUNG

Hiermit versichere ich an Eides Statt, dass die vorliegende Arbeit abgesehen vom Rat meiner akademischen Lehrer ohne fremde Hilfe und lediglich unter Verwendung der angegebenen Literatur sowie den bekannten Nachschlagewerken der Naturwissenschaften angefertigt habe und sie nach Inhalt und Form meine eigene ist. Diese Arbeit ist unter Einhaltung guter wissenschaftlicher Praxis entstanden. Ich versichere, dass diese Arbeit weder ganz noch teilweise an anderer Stelle zur Prüfung vorlag. Frühere Promotionsversuche wurden von mir nicht vorgenommen.
Desweiteren erkläre ich hiermit, dass die in Kapitel 5 vorgestellten Ergebnisse bereits im Journal Amercican Institut of Physics in der hier vorgestellten Form (Peleikis et al., 2016) veröffentlicht wurden. Die in Kapitel 6 vorgestellten Ergebnisse sind bereits online vom Journal Astronomy and Astrophysics veröffentlicht und werden bald auch schriftlich verfügbar sein (Peleikis et al., 2017). Die im Appendix 9 vorgestellte Publikation wurde ebenfalls von Astronomy and Astrophysics veröffentlicht (Heidrich-Meisner et al., 2016).

Kiel, Mai 2017

Thies Peleikis